Threshold Velocity and Incubation Period in Water Droplet Erosion

Mohamed Elhadi Mohamed Ibrahim

A Thesis

In

The Department of

Mechanical, Industrial and Aerospace Engineering

Presented in Partial Fulfilment of the Requirements for the Degree of Doctorate in Philosophy (PhD) (Mechanical Engineering) at

Concordia University

Montreal, Quebec, Canada

July 2022

CONCORDIA UNIVERSITY

School of Graduate Studies

This is to certify that the thesis prepared

By: **Mohamed Elhadi Mohamed Ibrahim**

Entitled: **Threshold Velocity and Incubation Period in Water Droplet Erosion**

and submitted in partial fulfilment of the requirements for the degree of

Doctor of Philosophy (Mechanical Engineering)

Complies with the regulations of the University and meets the accepted standards with respect to originality and quality.

Signed by the final Examining Committee:

_____Dr. Bruno Lee_____*Chair*

_____Dr. Richard Chromik_____ *External Examiner*

_____Dr. Ahmed Soliman _____ *External to Program*

_____Dr. Susan Liscouet-Hanke_____*Examiner*

_____Dr. Ayhan Ince_____ *Examiner*

_____Dr. Mamoun Medraj _____Thesis *Supervisor*

Approved by: _____ Dr. Ivan Contreras _____ *Graduate Program Director*

_____September 16th, 2022_____ __ Dr. Mourad Debbabi _____

Date

Dean, Gina Cody School of Engineering and Computer Science

Abstract

Threshold Velocity and Incubation Period in Water Droplet Erosion

Mohamed Elhadi Ibrahim, PhD

Concordia University, 2022

Erosion wear due to high-speed water droplets impact is a major reliability concern in several power generation and aerospace industries. The problem is synonymously referred to as water droplet erosion (WDE), liquid impingement erosion (LIE), rain erosion (RE), or leading-edge erosion (LEE). The present work addresses two important erosion responses; material endurance against erosion (known as the threshold condition) and the number of droplet impacts needed to initiate erosion damage (known as the incubation period). The objectives of the work are to develop a prediction model for the threshold condition, and to contribute to the understanding of the damage mechanisms in the incubation period.

The present work combines the theory of threshold crack propagation with dynamic wear and fracture properties of materials to arrive at a mathematical equation (model) for the threshold conditions. The developed model predicts the threshold impact velocity of metallic materials directly from their mechanical properties and impact conditions. The model is experimentally validated for five metallic alloys namely; Ti-6Al-4V alloy, 17-4 PH stainless steel, stainless steel (X22CrMoV12-1), 7075-T6 aluminum alloy, and 2024-T4 aluminum alloy. The developed model is also compared to the analytical model developed in the literature and found to predict threshold velocities with higher accuracy. The threshold velocity - simply calculated from the developed model - can directly evaluate the risk of developing erosion damage for specific material, and hence can be used as an effective material design and selection tool.

As for the incubation period, the influence of change in surface roughness (i.e., roughening) and the rate of change in hardness (i.e., hardening) on the damage accumulation process have experimentally and numerically been investigated in this work. Water droplet erosion tests were carried out on Ti-6Al-4V alloy and 17-4 PH stainless steel. Scanning electron microscopy (SEM), Confocal Laser Scanning Microscope (CLSM), Vickers Hardness measurement, Tensile Tests, and Finite Element Analysis (FEA) of Impact stresses were carried out. The results show that the dynamic surface roughening process results in higher and continuously-increasing impact stresses for the same impact pressure due to geometrical stress concentration. It is also found that the strain hardening exponent (n) influences the incubation period by controlling the rate at which the fracture of surface fragments is achieved as well as the rate with which mechanical properties change with the increase in number of droplet impingements. It is concluded that strain hardening exponent (n) and surface roughening are crucial parameters in the damage accumulation process during the incubation period.

Acknowledgements

I would like to express my deepest appreciation to my supervisor Professor Mamoun Medraj. He provided me with opportunity to purse this PhD and ensured that I received the adequate personal and financial support. The completion of this work would not have been possible without his technical inputs. Moreover, I learned and received from him endless amount of advices and mentorship that go well beyond the present thesis. I am extremely grateful to have worked with Professor Mamoun Medraj.

I also would like to extend my acknowledgement to Water Droplet Erosion Team at Concordia University including Dr. Abdullahi Gujba, Rizwan Ahmed, Ming Jing, and Mostafa Elyoussef for their inputs, continuous support and encouragement during the course of this research. Deep thanks also go to our lab associates and research group members including Dr. Dymtro Kevorkov and Mr. Mazen Samara, Eslam Fayed, and Fatile Babajide Oluwagbenga.

Special thanks to Dr. Mason Marzbali form American University in Dubai for his collaboration in the numerical analysis performed in this work.

I would like to recognize the assistance and the help of my friends. They made Montreal feels like home for me during these years.

Finally, I would like to express my deepest gratitude for my parents Elhadi and Magbola for providing me with all kinds of supports, motivation and inspiration throughout my journey.

Table of Contents

List of Figures

List of Tables

1 INTRODUCTION

This chapter lays out the necessary background to the present work. The initial sections provide a definition of the Water Droplet Erosion (WDE) phenomenon, industrial applications where WDE is frequently encountered, and a brief description of the physics and mechanics of WDE. Later sections of the chapter introduce the different aspects of WDE prediction and the objectives of the present thesis.

1.1 Water Droplet Erosion

Water Droplet Erosion (WDE), synonymously known as liquid impingement erosion (LIE), rain erosion (RE) or leading edge erosion (LEE), is a form of materials wear caused by the repetitive impact of water/liquid droplets with sufficiently high speed on solid surfaces [1]. Discrete water droplets distinguish WDE phenomenon from other liquid damage phenomena such as liquid jet erosion and cavitation. This is because the range of impact pressures, and hence stresses caused by discrete water droplet impact is considerably higher than that in other forms of liquid impact.

1.2 Industrial Occurrence of WDE

Water droplet erosion (WDE) of solid surfaces has long been a concern for most of high-speed moving components in hydrometer environments (i.e. environments containing liquid droplets). As such, blades of machineries are particularly prone to experiencing WDE damage. These include:

Steam turbine blades: WDE damage is often observed on the blades of the low pressure (LP) cycle of steam turbine [2,3]. Due to their length, the tip of these blades can assume a linear speed

of up to 900 m/s. The interaction of the wet steam droplets with these blades, as demonstrated in Figure 1-1 (a), results in their erosion [4,5].

Compressors of gas turbine: The inlet air to the compressor is usually cooled by spraying liquid droplets to maximize air density and intake air mass (the process is known as fog cooling) [6,7]. This will in turn increase the power output of the turbine, and therefore, improve the efficiency of the unit [6]. Although this method was proven to be effective in addressing the high ambient temperature issue, droplets are observed to cause severe damage to the leading edge of the compressor blades, as illustrated in Figure 1-1 (b). Severe erosion damages cause blade vibrations, which in turn results in serious fatigue damages and loss in efficiency [6].

Wind turbine blades: The continuous increase in the diameter of wind turbine blades has resulted in high linear speed of the blade's tip. The interaction of the tip with rain droplet causes severe erosion damages to its leading edge [8,9]. The problem is even more in the offshore wind farms [8].

Other rotating blades: WDE due to rain erosion is seen also in helicopters, where leading edges of rotor blades are observed to experience significant erosion even at subsonic speeds [10]. More recently, aero-engine fan blades [11] and compressor of turbocharges in automobiles [12] have also been reported to encounter WDE.

Linearly moving objects: Although primarily encountered in rotating blades, WDE damages have also been observed in linearly moving objects such as rockets and airplanes. For instance, erosion caused by rain drops impact on the surface of aircrafts has been a serious issue in aviation [10,13]. Components made of brittle materials such as glass or thermosetting plastic domes and fiber reinforced plastic radomes are the most susceptible to WDE damages [14]. Figure 1-1 (c)

shows the areas in aircraft that are likely to experience WDE damage. Erosion damage appears in the form of pitting of the airfoils and paint stripping [14].

Moving droplets: WDE is also observed in carbon steel pipelines used in nuclear/fossil power plants, resulting in what is known as "wall-thinning" [15]. This usually happens when accelerated flow of steam passes through orifices, impinging bent parts of the pipe (Figure 1-1 (d)). This eventually leads to the pipe failure, which then leads to the leak of the steam flow to the surrounding environment. Similar incident was reported in Onagawa power plant in 2007 [15].

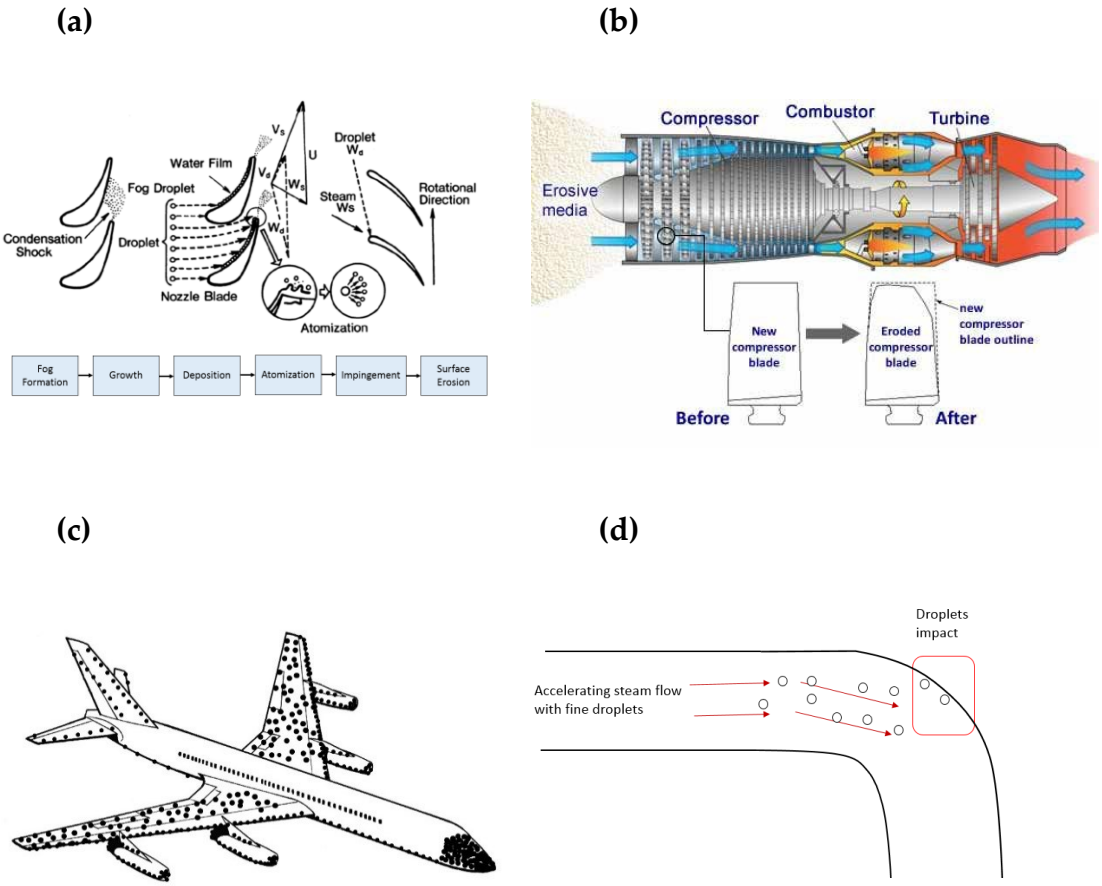

Figure 1-1 Examples of WDE occurrence; (a) blades of low pressure stage in steam turbine [16], (b) compressor of gas turbine (courtesy of MDS Coatings Technologies), (c) parts of airplane, redrawn from [10], and (d) pipes of nuclear power plants [15].

Table 1-1 provides a summary the parts that are likely to be affected by the liquid impingements in various applications as well as the typical materials of these parts. It also lists the erosion impact conditions, namely; the impact speed and droplet size, encountered in these applications. It should be noted that droplet sizes are difficult to quantify for these applications and only approximate ranges could be provided. Values provided in Table 1-1 are inferred from the traces of erosion damage, expect in the case of rain erosion (i.e., wind turbine, aircrafts, etc.) where the characteristics of raindrops can be studied from meteorological observations.

Table 1-1 Summary of the erosion conditions in some applications.

Application	**Parts Affected**	**Typical Materials**	**Impact speed**	**Droplet Diameter**	**Ref(s)**
Steam Turbine	Blades of the low-pressure stage	12% Cr Stainless Steel Ti-6Al-4V Nickel-based Superalloys	400–900 m/s	50–400 μm	[5,17]
Gas Turbines	Compressor blades	Ti-6Al-4V 12% Cr Stainless Steel	100–800 m/s	200–600 μm	[18]
Wind Turbine	Wind turbine blades	Polymer Composites Elastomeric Coatings	70–150 m/s	0.5–5 mm	[9,19,20]
Nuclear Power Plants	Cooling pipes	Carbon Steel	~200 m/s	60–80 μm	[21]
Aero engine	Fan blade	Ti-6Al-4V	200–400 m/s	1–5 mm	[22]
Aircrafts	Rain erosion of different parts.	Aluminum Alloys Polymer Composites	Civil airplanes ~ 250 m/s Fighter Jets ~ up to 5 Mach	1–5 mm	[10,23]

The question of how repetitive impact of liquid droplets causes erosion damage on solid surfaces has usually been studied under two main aspects of investigation: (i) the physics of the interaction of a single droplet with a solid surface at high strain rate and (ii) the mechanics of damage accumulation in multiple/repetitive droplet impingements. The following sections provide a brief description of these two aspects of water droplet erosion.

1.3 Physics of Single Droplet Impact

The high-speed impact of a single droplet onto a solid surface consists of two phases [24]; (i) pressure build-up phase characterized by impact pressure and stress wave and (ii) a pressure release phase featured by lateral jetting.

1.3.1 Pressure Build-up Phase

The sudden impact of a droplet on solid surface results in a high pressure at the contact area. This pressure, initially postulated by Cook [25], has traditionally been referred to as "water hammer pressure". Cook [25] proposed the following equation to calculate the water hammer pressure:

$$P = \rho_0 C_0 V \qquad (1\text{-}1)$$

where $\rho_0,\ C_0,\ and\ V$ are the liquid density, the speed of sound, and the impact speed of the droplet respectively. Following Cook's water hammer equation, the impact pressure has gained considerable attention in WDE investigations because it represents the primary "loading" parameter. The equation proposed by Cook [25] represents a uniform one-dimensional pressure and ignores the influence of the shock wave velocity variable for rigid and elastic surfaces. As such, several modifications to the Cook's water hammer equation were made [26–28]. Through these efforts, it has been established that the impact pressure has spatial and temporal distribution

in the impact zone, as well as a maximum peak value that occurs at a critical contact radius (r_c) [29–31]. The maximum peak value is the most important as it dictates the magnitude of the peak stress in the solid. Heymann [29] approximated the maximum peak pressure to be three-times the water hammer pressure. The full temporal and spatial distribution of the impact pressure was provided by many numerical works [32–34], some of which confirmed Heymann's approximation of the maximum peak pressure. Once the impact pressure is obtained, it is usually used as a boundary loading condition acting on the solid target.

1.3.2 Stress Waves

During the build-up phase, the mechanical equilibrium (i.e. state of stress) in the target material is disturbed by the impact process and the associated impact pressure acting on the impact zone. Three stress waves emerge from the impact zone to propagate this disturbance to the rest of the solid, and therefore, shape its stress and strain field [24]. These (illustrated in Figure 1-2) are a compressional wave moving in a longitudinal direction, a shear wave moving in a transverse direction, and a Rayleigh wave moving along the surface [24,35]. Fracture can occur if the propagating stress waves have amplitudes - of sufficient duration - higher than the dynamic fracture strength of the solid. Stress waves of lower amplitude can also interact with microstructural discontinuities to produce high tensile stress due to stress concentration [36]. Hence, stress wave propagation has traditionally been considered among the mechanisms with which high-speed droplet impact can cause failure.

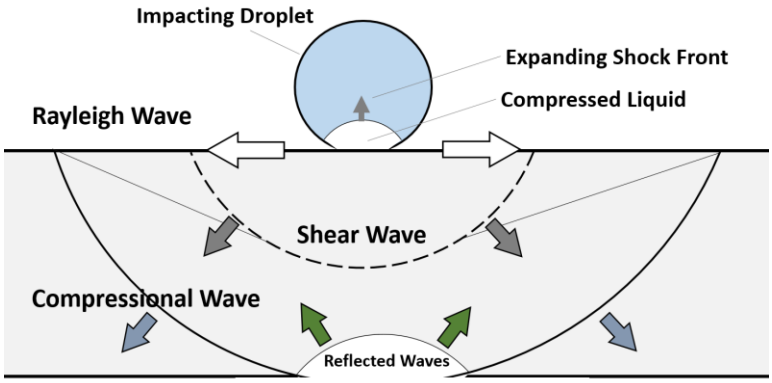

Figure 1-2 Schematic of shock wave behavior during the liquid droplet-solid surface interaction. Redrawn from [10].

1.3.3 Pressure Release Phase and Lateral Jetting

The impact moment (consisting of impact pressure and stress waves) terminates when the pressurized droplet starts releasing. This is accompanied by what is called lateral outflow (or lateral jetting), which is the spreading of the droplet from the periphery of the contact zone. The velocity of the lateral jets depends on the impact velocity [35,37]. For instance, Figure 1-3 shows the variation of lateral jetting velocity for a 2 mm water droplet over a range of impact velocity of 100 to 1140 m/s based on Jenkins and Booker [37] experiments. It can be noticed that lateral jetting velocity can reach up to six times the impact velocity. From a tribological point of view, such high-speed jets may cause high shear stresses and potentially tear surface irregularities. This is why the surface quality and roughness play a very important role in the initiation of erosion damage.

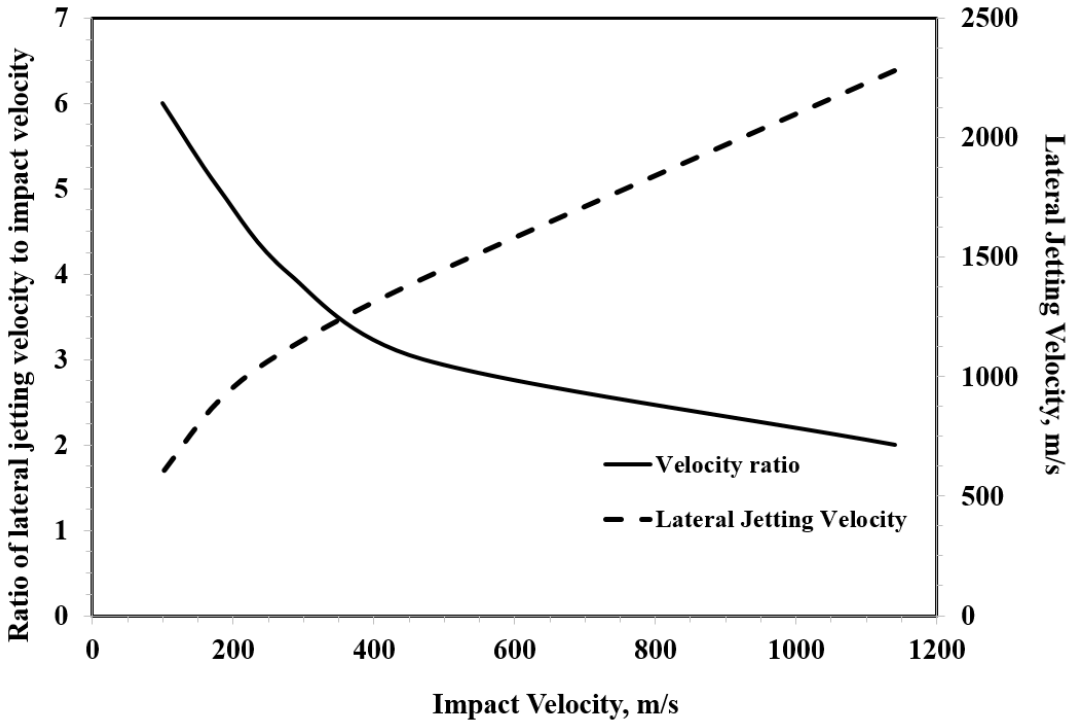

Figure 1-3 Lateral jetting velocity as a function of impact velocity. Redrawn from [76].

1.4 Mechanics of Water Droplet Erosion

In most of the cases, stresses due to a single droplet impact event are not enough to cause erosion damages. Multiple and repetitive droplet impacts on a certain area (impact area) are needed to result in erosion damage in a way akin to fatigue failure. There is a gap in the theoretical understanding of WDE phenomenon related to how the stresses from the individual droplet impacts sum up in the repetitive WDE to eventually result in erosion damage [9]. Nevertheless, experimental testing over the past several decades have established few empirical facts about the mechanics of water droplet erosion. These are discussed in the following sections.

1.4.1 Regimes in Water Droplet Erosion

The outcome of droplet impact process depends markedly on the impact velocity. That is, experimental observations [38,39] suggest that different ranges of impact velocity seem to result

in different water droplet erosion "regimes". Many important aspects distinguish an erosion regime from another such as the predominant damage mechanisms and the way with which erosion damage progresses with time. So far, there seem to be three confirmed droplet impact regimes (illustrated in Figure 1-4); Lower threshold, gradual erosion damage, and the upper threshold. These are detailed in the ensuing discussion.

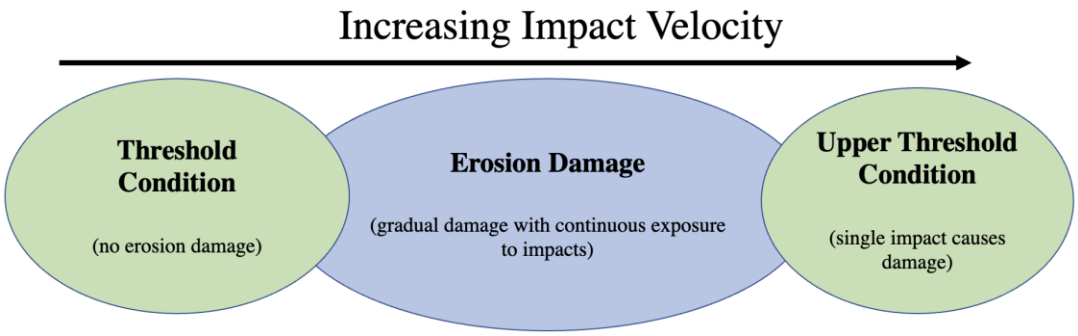

Figure 1-4 Different regimes in water droplet erosion.

1.4.2 Threshold and Upper Threshold Condition

The threshold condition, sometimes referred to as lower or absolute threshold [40], indicates the condition where the intensity of the erosion attack -represented by the impact velocity at a given droplet size- is so low that the material will never experience erosion damages for any practical exposure time. As such, in the threshold condition, erosion is completely avoided. It is likely that the threshold regime is controlled by the elastic and mechanical properties of the target materials [41]. Threshold velocity is often used to refer to the threshold condition.

On the other hand, the upper threshold represents the condition where a single droplet impact event can cause a detectable/measurable erosion damage [42]. This regime is seen when the intensity of the erosion attack is considerably high compared to the erosion resistance of the

material. The damage mechanism in single-impact erosion is likely to be governed by the dynamic fracture strength of the target material and the shearing effects of the lateral jetting [10,43]. Also, it is not known how erosion damage progresses with time (or number of impacts) in this regime [9].

1.4.3 Erosion Damage Regime

Erosion damage regime is usually observed in a wide range of erosion intensities with normal exposure durations. In this regime, multiple droplets are needed to initiate erosion damage. Once the damage started, exposure to subsequent droplet impacts further propagates the erosion damage.

For bulk materials and coatings, erosion damage in this regime shows a strong time-dependency, i.e. it exhibits different erosion rates at different time intervals, resulting in a nonlinear progression of damage [39]. This is usually presented in the so-called erosion curves. Figure 1-5 shows a schematic of the typical (often called S-shaped) erosion curve observed during water droplet erosion (WDE) of almost all bulk materials. The erosion curve is traditionally divided into five distinct regions or stages, as shown in Figure 1-5. These are; the incubation period (stage A) where there is only increase in the roughness of the surface due to the repetitive impact of the water droplets without measurable material loss; Acceleration stage (stage B); Steady-state maximum erosion rate (stage C) where the erosion rate is maximum and remains constant for relatively long period; Attenuation or deceleration stage (stage D) where the erosion rate starts to decrease; and the terminal stage (stage E) where the erosion rate is constant once again.

The incubation period (stage A) and the steady-state maximum erosion (stage C) are considered the most important stages in this regime [39]. This is because the length of the incubation period indicates the resistance of the material to water droplet impacts. Whereas the linear relationship between the erosion rate and exposure duration over steady-state maximum

erosion rate stages allows for the anticipation of amount of erosion damage over a certain period of time.

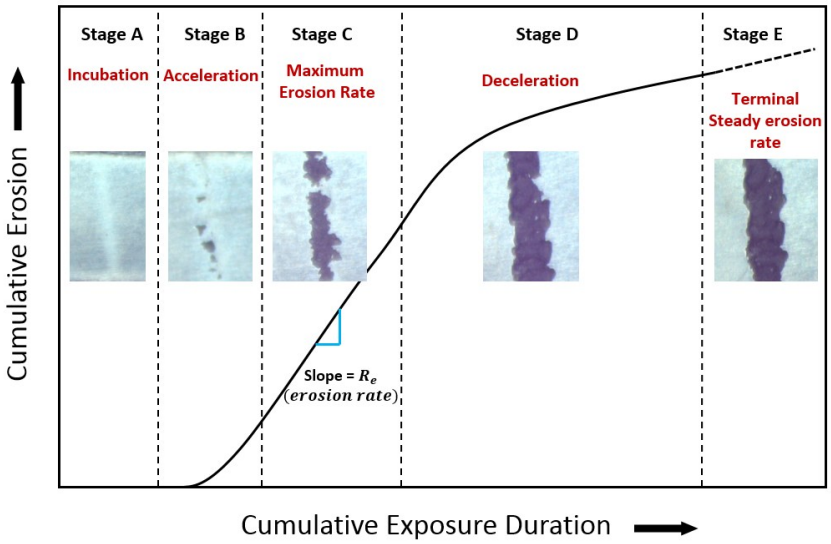

Figure 1-5 Typical erosion curve and stages of damage.

Most of theoretical and empirical investigations of Water Droplet Erosion (WDE) focus on erosion damage regime, particularly the incubation period and the steady-state erosion rate. This is because erosion damages in most of industrial applications proceed according to this regime. The investigations can be summarized into three categories aiming to; (i) understand damage mechanisms in a specific stage of erosion, (ii) understand and quantify the role of impact parameters and mechanical properties on the erosion rate, and (iii) develop models to predict the incubation period and erosion rate at different stages. Since prediction of water droplet erosion is the main focus of the present work, it is further detailed in the following section.

1.5 Prediction of Water Droplet Erosion

Prediction of water droplet erosion is the development of mathematical models that evaluate different erosion responses as a function of impact parameters (such as droplet size and impact velocity), liquid properties (such as density, viscosity, and speed of sound), and solid properties [44]. The most important erosion responses to be predicted are:

1- The length of the incubation period, which describes the time (or number of droplet impacts) needed to initiate erosion damage.

2- The steady-state maximum erosion rate, which describe the way in which erosion damage progresses with exposure duration.

3- The threshold velocity, which describes the WDE endurance condition.

Different approaches are followed in developing prediction models including; analytical, numerical, empirical, and statistical methods [30,45,46]. However, there are many challenges associated with developing erosion prediction models. The two main challenges are [9,38,39]:

Lack of representative failure mechanisms. The development of prediction models requires the adoption of adequate failure mechanisms to represent the cumulative erosion damage due to multiple impacts. However, due to the complexity of water droplet erosion phenomenon, the so-far proposed erosion failure mechanisms fail to comprehensively represent the erosion process. Therefore, further insights into the nature of damage accumulation are needed for the development of accurate prediction models.

Relevant target properties. In water droplet erosion, the impact process occurs at very high strain rate and in a repetitive manner. As such, it has always been difficult to identify the target mechanical properties responsible for its erosion resistance. Moreover, it is not known whether a set of properties applicable to a certain erosion intensity or erosion stage would still

be valid at different intensities and stages where microscopic failure modes may change, or geometrical configurations may significantly alter the solid response to droplet impact.

Despite the challenges, erosion prediction models are extremely important in material design and selection for applications facing the threat of water droplets impact. The present thesis focuses on the prediction of erosion and its challenges. The objectives of the present thesis are presented in the next section.

1.6 Thesis Objectives and Scope of the Work

1.6.1 Thesis Objectives

The present work targets the prediction of water droplet erosion phenomenon. This is because the successful prediction of WDE enables researchers as well as industry to design and select material in such a way that WDE can be prevented. The present thesis aims:

1- To develop a prediction model and experimental procedure to evaluate the threshold condition of metallic materials. The development of such a model will help in evaluating the endurance conditions in water droplet erosion.

2- To investigate the role of hardening and roughening on the incubation period. This will contribute to the understanding of the mechanisms of damage accumulation during the incubation period, which may facilitate developing a comprehensive incubation prediction model in the future.

To achieve the above-mentioned objectives, the present work aims to accomplish the following tasks:

1- To derive a mathematical expression of the threshold velocity from the properties of the material and impact parameters.

2- To establish an experimental procedure to evaluate the threshold velocity of metallic materials.

3- To investigate the role of cyclic change in surface roughness on impact stresses.

4- To investigate the role of strain hardening exponent (n) on the damage accumulation and erosion resistance of solid materials.

Figure 1-6 represents a summary of the objectives of the present work.

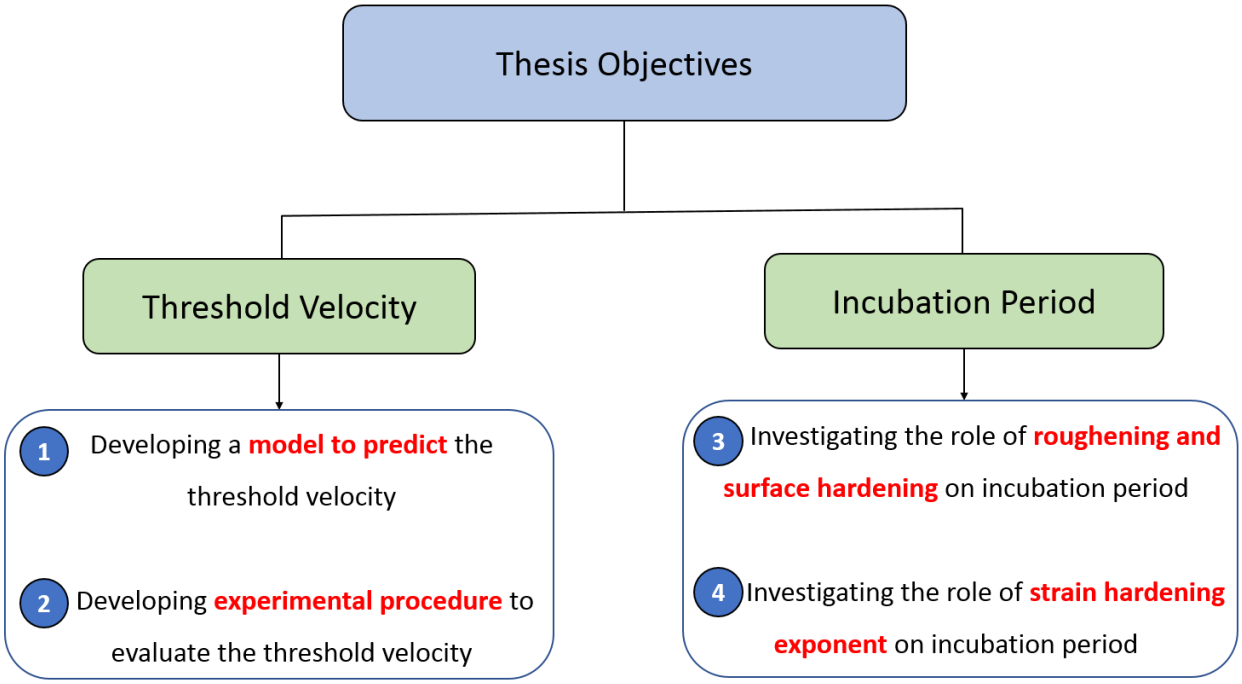

Figure 1-6 Summary of thesis objectives.

1.6.2 Scope of the Work

The scope of the present work in terms of the modeling approach used, materials considered, and experimental measurements and characterization is discussed in this section. The modeling approach adopted for the prediction of the threshold condition is that of a semi-analytical nature. This is because first principles analysis of water droplet erosion requires the consideration and mathematical treatement of multiple complex phenemona such as stress waves, Rayleigh wave, direct stresses, lateral jetting and shear stress, etc. This has been shown to be an extremely difficult endeavor [47]. Instead, the semi-analytical approach adopted in this work assumes a microscopic damage mechanisms (e.g., crack propagation), and attempts to put the assumed mechanism into mathematical formula to build the prediction model. In this way, microscopic treatement of water droplet erosion is achieved, while dealing with the complexity of its first principle physics is avoided.

In terms of materials, the present work deals only with metals. This is because different classes of materials react differently to droplet impacts. As such, developing prediction models for all classes of material is unrealistic as many aspects must be included such as viscoelastic behavior of polymers, brittle fracture of ceramics, etc. Nevertheless, the utility of the present work, since it addresses metals, covers most of the applications where water droplet erosion is encountered, namely; aerospace (e.g., aluminum alloys), steam turbines (e.g., stainless steels), and gas turbines (e.g., titanium alloys).

Finally, since the main objectives are to achieve qualitative understanding of the different mechanisms that lead to the initiation of damage at the end of the incubation period and to validate the threshold prediction model, only relevant measurement and characterization techniques are presented in this work. These include optical imaging, mass loss measurement ($\pm$

0.1 mg accuracy), scanning electron microscopy (SEM), roughness measurement using confocal laser scanning microsope (CLSM), and Vickers mircohardness. These techniques were utilized because they can result in non-destructive examination of the test samples at several intervals during erosion tests.

1.6.3 Structure and Layout of the Thesis

The structure of the present thesis is outlined in Figure 1-7. This can act as a map that allows better reading.

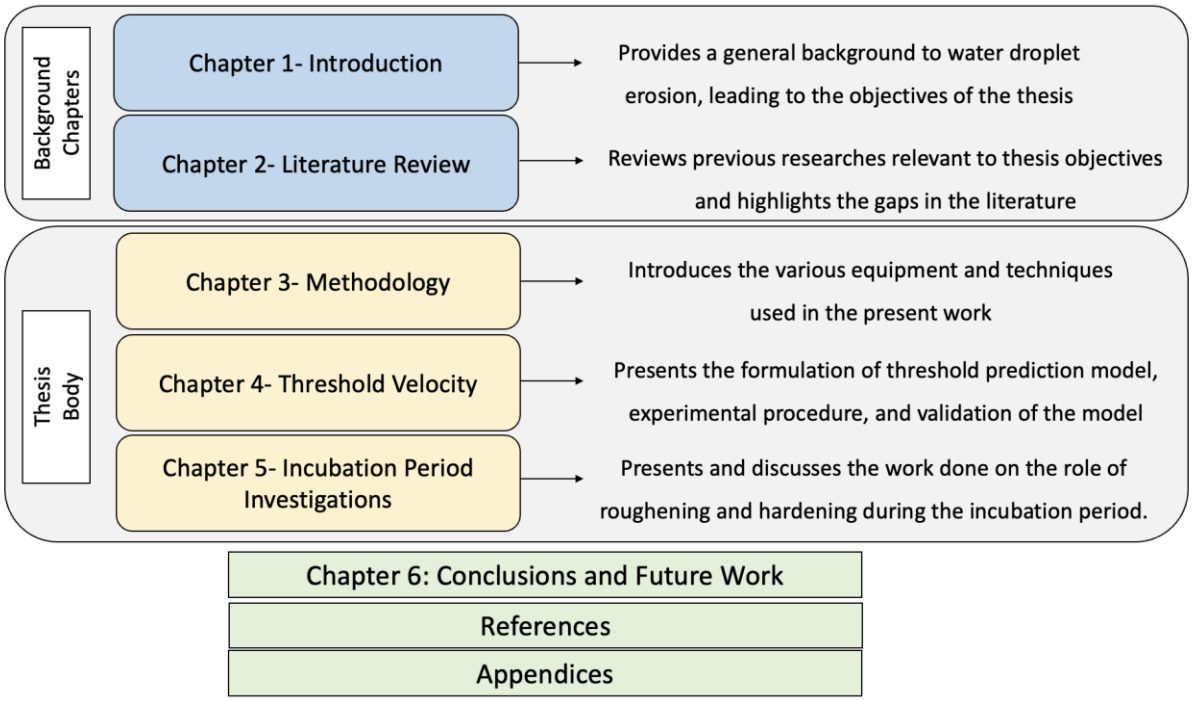

Figure 1-7 Thesis layout

2 LITERATURE REVIEW

This chapter surveys the relevant literature to the thesis objectives. The chapter consists of; (i) previous attempts made to predict the threshold velocity; (ii) mechanism of damage accumulation during the incubation period; and (iii) and role of hardening and mechanical properties during the incubation period. The end of the chapter presents the gaps in predicting the threshold velocity and understanding the incubation period.

2.1 Threshold Velocity and Its Prediction

2.1.1 Introduction to Threshold Velocity

The threshold velocity has traditionally been defined as the impact velocity below which the solid surface is not likely to experience water droplet erosion damage for any practical exposure duration [48,49]. It resembles the endurance condition in fatigue. The existence of such impact velocity can be linked to the impact pressure. This is because erosion damage is principally caused by the accumulation of stresses that result from the repeated pulses of high impact pressure induced during impingement events [9]. The impact pressure depends mainly on the impact velocity [31,50]. As such, the threshold velocity can be conceived as the impact velocity at which the resulting impact pressure and the consequent stresses are not sufficient to cause plastic deformation, initiate cracks, and/or to propagate existing cracks.

The origin of the concept may be traced back to the work of Honegger [51] in 1927, where the threshold (or limiting) velocity was mentioned as one of the important parameters needed to predict the erosion rate. In 1933, Dehaller [52] suggested that the threshold velocity is not an independent parameter but a function of droplet size. Therefore, threshold velocity should always

be reported at a given droplet size. Honegger [51] and Dehaller [52] provided no details about how to predict or experimentally evaluate the threshold velocity. It was not until the late 1960s that empirical and analytical investigations of the threshold velocity have become an essential aspect of studying water droplet erosion [41,53]. This was concurrent with then-efforts to treat the water droplet erosion phenomenon as a fatigue problem, and hence, the importance of the threshold was emphasized as the equivalent to the endurance limit [53]. From practical consideration, evaluation of the threshold velocity - as the parameter that represents the WDE endurance condition - is of paramount importance in the design and selection of materials for applications where WDE is among failure and reliability concerns.

2.1.2 Experimental Evaluation of the Threshold Velocity

When erosion tests are performed at the threshold velocity, no sign of erosion should be detected and the surface of the material should remain intact against infinite number of droplet impacts. Since erosion tests cannot be run indefinitely, threshold experiments are viewed as "erosion' tests performed to identify the condition of "no erosion". This presents researcher with an empirical pardox. To avoid this problem, testing methodology or a criterion through which a representative value to the threshold velocity can be estimated. The main feature of the criterion is to identify the time at which erosion tests must be stopped.

Historically, different researchers used different criteria. Thiruvengadam [41] considered the threshold velocity to be the velocity after which 10 million impact cycle are not enough to cause detectable damage, when the surface of the material is examined with x10 magnifying lens. The choice of 10 million in Thiruvengadam's work was related to fatigue strength of material. That is, for most of bulk metals, fatigue strength is often considered to be the stress value at

which 10 million cycle are barely enough to cause failure. Hence, Thiruvengadam [41,53] utilized the fatigue strength criterion to evaluate of the threshold velocity.

Kennedy and Field [40] adopted different approach for evaluating damage thresholds of brittle materials. They distinguished between damage threshold velocity, which indicates the impact velocity at which specified number of impacts initiate damage, and absolute damage threshold velocity which is the condition of no erosion regardless of the number of impacts. It is claimed in their work [40] that the absolute threshold velocity can be detected from the plateau of the plot of the impact velocity versus the number of impact needed to initiate damage. However, some of the materials do not show that plateau in erosion tests [48], which problematizes Kennedy and Field criterion for evaluating the absolute threshold velocity.

Mahdipoor *et al.* [54] considered the threshold velocity to be the impact velocity at which 1 million impact cycles do not cause detectable damage. No justification is given for the choice of the number of impacts in their study [54].

It can be concluded that a clear criterion for the experimental evaluation of the threshold velocity has not yet been established, and more research in this area is needed.

2.1.3 Prediction of the Threshold Velocity

In general, modelling different aspects of water droplet erosion (e.g., threshold velocity, incubation period, etc.) by tackling the phenomenon from first principles has always been a formidable task [47]. This is because of the complex, coupled liquid-solid interaction, and the repetitive nature of WDE failure [39,47]. Modeling efforts have, therefore, focused more on analytical approaches where underlying damage mechanisms are presumed and used to develop predictive models [45,53,55]. In addition, there are also empirical efforts to predicting water

droplet erosion, where statistical fitting of erosion data is used to provide prediction equations [40,48]. In the open literature, there is only one analytical model and two empirical equations developed for the prediction of the threshold velocity so far. These are outlined in the following discussion.

Thiruvengadam's threshold model

Thiruvengadam [41,53] considered water droplet erosion as a fatigue phenomenon. As such, he [53] assumed that at the threshold condition, the impact pressure is less than or equal to the erosion strength of the material, which is represented mainly by the endurance limit. This resulted in the following model:

$$V_c = \frac{\beta\, \sigma_e}{\rho_l^{1/2} E_m^{1/2}} \qquad (2\text{-}1)$$

where V_c is the threshold velocity, σ_e is the endurance limit of the material, ρ_l is the density of water, E_m is the elastic modulus of the material, and β is given by:

$$2\,\beta = \left(\frac{E_m}{K_l}\right)^{1/2} \qquad (2\text{-}2)$$

where K_l is the bulk modulus of the liquid (for water is 2.2 GPa). It is to be noted that Thiruvengadam's model of threshold velocity does not take into consideration the influence of the droplets size, which is known to affect water droplet erosion. This results in remarkable prediction errors. Nevertheless, his model remained the only threshold prediction model that is developed semi-analytically.

Empirical correlations of threshold velocity

Following Thiruvenagadam's work, two empirical equations were developed from curve fitting of erosion data to predict the threshold velocity. These are as follows:

$$V_c^2\, d = \ constant \qquad (2\text{-}3)$$

$$V_c^3\, d = \ constant \qquad (2\text{-}4)$$

where $V_c \ and \ d$ are the threshold velocity and droplet size, respectively. Heymann [48] used previously published data to arrive at equation (2-3) to predict the threshold velocity based on the average droplet size and a material constant. Equation (2-4) was developed by Kennedy and Field [40] from fitting erosion data of ceramic materials. Unlike Thiruvengadam's [53] equation, these two equations take into consideration the influence of the droplet size on the threshold velocity. However, estimation of the constant in both equation requires that the threshold velocity at a certain droplet size to be initially known (found from initial experiments). Once this velocity is known, other threshold velocities corresponding to different droplet sizes are calculated from the equation. Moreover, the two models do not describe how an approximate value of the threshold velocity can be obtained from the materials properties without performing experiments

No other attempts to predict threshold velocity could be found in the open literature, and most of the current prediction efforts focus on modeling other erosion damage parameters such as incubation period and erosion rate [55–57].

2.2 The Incubation Period

As mentioned, single or few droplet impacts do not result in erosion damage. Repetitive droplet impacts on the same area (i.e., impact area) are needed to initiate erosion damage. The incubation period is defined as the exposure duration (in time or number of impacts) needed to cause measurable erosion damage [39]. Traditionally, measurable erosion damage is considered to be either the appearance of large erosion pits on the surface and/or 0.1 mg mass loss from the material [38]. In this sense, the length of the incubation period determines how long a material can survive droplet impacts before showing signs of damage. In other words, the incubation

period is a primary indicator of erosion resistance of materials [49]. Therefore, developing models to predict the length of the incubation period is an important aspect of water droplet erosion research [1,46,55,57,58].

The successful prediction of the incubation period requires the identification of the three important aspects [38,45,47,59]: (i) the magnitude of stresses caused by the droplet impacting the surface with certain characteristics (i.e., impact velocity, droplet size, etc.), (ii) failure mechanisms to account for how impact stresses accumulate to cause material failure, and (iii) the mechanical properties of the solid target that represent the resistance of the solid to stress and damage accumulation.

The present work attempts to contribute to the understanding of the damage accumulation process and the role of surface and mechanical properties of the target material in the incubation period. As such, the state of knowledge in these two areas is reviewed in the following subsections.

2.2.1 Mechanisms of Damage Accumulation During the Incubation Period

Researchers have attempted to propose mechanisms to account for the way in which damage accumulates during the incubation period to end up with erosion failure. There are two main hypotheses; fatigue and accumulation of plastic strain.

Fatigue received considerable attention as the principal underlying mechanism responsible for erosion damage accumulation in water droplet erosion of metals [41,45,55]. This is mainly due to the similarities between water droplet erosion and fatigue of materials in two fundamental aspects; (i) the repetitive nature of the two damage processes, and (ii) the existence of endurance condition in both (i.e., the WDE threshold impact velocity and the fatigue

endurance limit) [60]. For these reasons, incubation prediction models based entirely on fatigue have been developed [45,55]. Notably, Springer's [45] model remains one of the most used incubation prediction model throughout water droplet erosion literature.

However, some literature findings seem to undermine the role of fatigue in water droplet erosion. In 1970s, Adler [38] performed thorough microstructural examination of eroded surface of Ti-6Al-4V and pointed out that fatigue plays only a secondary role in the damage initiation. He concluded that initial impacts are responsible for topological changes in the surface (roughness and surface depressions), while the damage is caused mainly by lateral jetting and hydraulic penetration. Despite Adler's [38] remarks about fatigue, most of WDE researchers continued to consider fatigue to be the main mechanism behind damage accumulation until the recent work of Gujba [18,61] and MaDina [62]. They [18,61,62] performed various surface treatment known to remarkably improve fatigue life (i.e., deep rolling, laser shock peening, and ultrasonic nanocrystalline modification) on Ti-6Al-4V. They then carried out erosion tests to compare the erosion performance of the treated samples with respect to the as-received samples. Interestingly, the treated surfaces showed little or no improvement in erosion resistance compared to the untreated ones. Hence, concluding that fatigue is likely to have limited contribution to the way in which damage accumulates during the incubation period of metallic materials. Moreover, fatigue-based models [45,55], when used to predict erosion data beyond the data used in their derivation, result in remarkable prediction errors [60].

Accumulation of plastic strain leading to fracture of surface fragments has been another hypothesis put forward to explain the damage accumulation during the incubation period. This may be traced back to the work of Rieger [63] in 1965, where he postulated that ductile metals, as an initial response to repetitive droplet impingements, will experience plastic deformation and

accumulate plastic strains. After sufficient number of impingements, a state of deformation is reached where the density and concentration of dislocations becomes very high. At these locations, the internal stresses exceed the fracture strength of the metal and cracks are formed. Material removal process is then thought of as extension and joining of these cracks.

The plastic deformation due to droplet impact is usually evidenced by the hardening of impact area, especially for metals. For instance, it was demonstrated in [64–66] that metals do strain harden by the action of droplet impact before signs of erosion are detected. Hardness was observed to increase till the end of the incubation period [64]. Generally, the hardening process cyclically alters the mechanical properties as well as the topology of the surface. These in turn, change the surface response to subsequent impacts. The dynamic change in the surface properties and its role in the damage accumulation process have not been considered in the literature.

In conclusion, fatigue and accumulation of plastic strain have been the main mechanisms proposed to account for the accumulation of erosion damage during the incubation period. However, empirical observations seem to undermine the role of fatigue in water droplet erosion or limit its influence to certain regimes. On the other hand, in accumulation of plastic strain hypothesis, there is no theoretical or empirical work that investigates the cyclic change in the properties the target due to the accumulated strains, and their role in the damage accumulation process during the incubation period. This will be attempted in this thesis.

2.2.2 Role of Solid Properties During the Incubation Period

In both single impact event and damage accumulation due to repetitive impacts, the mechanical properties of the solid target play a fundamental role. In single impact event, even though the magnitude of the water hammer pressure is considered to be independent of the target

properties, it has been shown that the stress generated from the pressure largely depends on the density, elastic modulus, sound and waves speed of the solid [38]. The work of Blowers [30], for example, analytically demonstrated how the response of an elastic solid to a droplet impact is dictated by the elastic modulus, sound and wave properties of the solid.

The mechanical and surface properties play important role in the repetitive-multiple impacts erosion damage [59]. This is because solid properties are responsible for the materials' resistance to water droplet erosion. Many studies have attempted to correlate erosion resistance to an individual property or a combined group of mechanical properties. Hardness, fracture toughness, fatigue strength, and tensile properties have been the main individual intrinsic properties thought to represent the erosion resistance of metallic materials. **Hardness,** in particular, received considerable attention [63,64,67,68] due to the fact that it indicates surface resistance to plastic deformation and has been successfully correlated with the resistance to other wear phenomena [69–71]. The length of the incubation period is found to increase linearly with the hardness of the same alloy systems [72]. Heymann [48] also reported that the inverse of the steady-state erosion rate is proportional to hardness raised to the power 2. However, Hammit and Heymann [72] argued that correlating hardness to erosion resistance withholds when different alloy systems are considered. The same conclusion have recently been affirmed by the experimental results and the analysis in the work of Ahmad *et al.* [4]. Therefore, hardness alone is not always a reliable predictor to erosion resistance of metals.

Studies aiming to correlate erosion resistance of materials to **fatigue strength** were also reported in the literature [41,71,73]. This was mainly motivated by the analogy between water droplet erosion and fatigue, particularly in the damage accumulation aspect of the two phenomena. Thiruvengadam *et al.* [41,53] correlated the threshold velocity in water droplet

erosion to the endurance limit of metals. Hattori and Itoh [73] found that the incubation period in cavitation erosion is proportional to the fatigue strength, but only for plastic materials. Bedkowski *et al.* [74] noted that cavitation erosion and fatigue can be described with a mathematical model of the same type. However, other studies [61,62] showed that improving fatigue strength does not improve erosion resistance, evidenced by lack of improvement in the length of the incubation period. Attempts to correlate **Fracture toughness** to the erosion response - particularly for ceramic materials – were also made. For example, in [40,75], fracture toughness was found to correlate well with the damage threshold velocity of ceramic materials. However, it does not -singlehandedly- explain the damage accumulation in regimes other than the threshold or effects of other classes of material.

The tensile properties (such as yield, tensile, and fracture strength) on the erosion resistance of metallic materials have extensively been investigated [36,46,64,76,77]. The significance of the tensile properties and the stress-strain curve is emphasized in studies that consider the plastic strain accumulation as the mechanism leading to erosion. Early investigations in this direction have focused on individual tensile properties. For instance, the work of Hoff *et al*. [64] concluded that erosion resistance of metals is proportional to the **tensile** strength raised to the power of 1.8 (the tensile strength can be linked to hardness). **Yield** strength has also been considered in the work of Thiruvengadam *et al.* [41]. Combination of tensile properties rather than an individual property seems to be more representative to erosion resistance of materials. In this regard, **strain energy** and **resilience** have received considerable attentions. Thiruvengadam [53] concluded that erosion rate in both cavitation and droplet impingement is inversely proportional to strain energy to fracture. However, Hobbs [76] found that ultimate resilience fits erosion resistance of metals more accurately than strain energy or tensile strength alone.

Moreover, Ahmad *et al.* [4] recently argued that elastic resilience best fits erosion resistance of several metals such as stainless steel and titanium alloys.

The previous attempts to investigate the role of solid properties on the response to water droplet impact overlooked the cyclic change in the properties with the exposure duration. That is, mechanical and surface properties evolve with exposure duration in different ways depending on the material and impact parameters, and that may influence the way in which damage accumulate to failure. For example, the role of strain hardening exponent (n) in water droplet erosion has not been taken into consideration. Given the repetitive nature of the WDE problem, the strain hardening rate of the material is likely to influence the damage accumulation process, and hence, the erosion response of the material. In some studies [61,62], it has been shown that mechanical surface treatments are not very effective in preventing or delaying erosion, because they introduce work hardening in the materials, and hence, duplicate the processes that occur during droplet impacts. As such, the strain hardening exponent of the material might have a strong influence on the length of the incubation period, because it could influence the rate of damage accumulation. This has not been studied before.

Surface roughness also influences the response of materials to water droplet impact [77–80]. Fujisawa *et al.* [79] illustrated that roughness greatly influences the distribution of the impact pressure on the contact zone. Kirols *et al.* [78] performed erosion tests on Ti-6Al-4V samples having various initial surface roughness values. It was concluded [78] that pre-existing surface irregularities in rough surfaces result in shorter incubation periods compared to that of smooth surfaces. This is because rough surface put the material one-step ahead in the damage process by eliminating the roughening stage that constitutes an important part of the incubation period [77,78].

However, the evolution of roughness with exposure to droplet impingements (roughening process) and its role on impact stresses have never been investigated. Different roughening profiles could alter the magnitude and distribution of the impact stress due to variation in stress concentration behavior. As such, the course of the incubation period could be significantly influenced by how the roughness changes as the exposure to droplet impingement continues.

2.3 Gaps in the Prediction Literature

Based on the presented discussion, and when it comes to predicting the threshold velocity and the incubation period, the following statements can summarize the gaps in the WDE literature:

1- Lack of experimental criterion to evaluate the threshold velocity. That is, there is no agreement about the number of impacts at which erosion tests are to be stopped to evaluate the threshold velocity. Such a criterion is needed and could be based on real lifetime of components.

2- Lack of a threshold prediction model. The only model to predict the threshold velocity (i.e., Thiruvengadam's [41,53] model) presupposes fatigue as a mechanism and ignores the influence of droplet size. Other equations [40,48] require initial experiments to obtain material constants. Therefore, a prediction model of the threshold velocity is needed.

3- Lack of understanding of the damage accumulation process during the incubation period. That is, the hypothesis that fatigue is the mechanism responsible to water droplet erosion could not be confirmed. Whereas, investigations to address the cyclic plastic strain accumulation process are still lacking.

4- The solid mechanical properties that are responsible of erosion resistance of materials are not fully identified. Moreover, the role of the rate of change in properties (e.g., strain hardening rate) has not been investigated.

5- The evolution of surface roughness due to droplet impacts, and its influence on the damage accumulation process have not been investigated.

3 METHODOLOGY

This chapter details the experimental methodology utilized to accomplish the objectives of the present thesis. The first part of the chapter overviews the tested materials. The following sections present the equipment used to carry out all the experiments (i.e., erosion test and various material characterization tests).

3.1 Tested Materials

3.1.1 Overview

Since the scope of this work is limited to metallic materials, five main alloys, namely; Ti-6Al-4V alloy, 17-4 PH stainless steel, stainless steel (X22CrMoV12-1), 7075-T6 aluminum alloy, and 2024-T4 aluminum alloy, are considered. These alloys are of significant importance in industrial applications where WDE presents a major concern. That is, stainless steels are commonly used as steam turbine blade material [81], Ti-6Al-4V is used as a blade material for compressor of gas turbines [82], and aluminum alloys are used in aerospace application [83]. The other reason for selecting these alloys is that they – together – offer a wide range of elastic and mechanical properties. This is needed to investigate the role of material properties on the threshold velocity. *Table 3-1* provides details about the companies from which samples of these materials were obtained.

Conditions of 17-4 PH. In addition to the 5 alloys, two heat treatment conditions of the 17-4 PH stainless steel are also considered in this work. This is because the 17-4 PH stainless steel is precipitation hardenable that can assume different conditions (each with different set of mechanical properties) through aging treatments. That is, the formation of copper-rich

precipitates within the laths of martensitic matrix of the 17-4 PH stainless steel enables variation in strain hardening and mechanical properties while the grain size remains the same [84–86]. The as-received condition of 17-4 PH will be referred to 'Condition-A'. The two heat treated conditions, namely, H925 and H1025, are achieved by aging Condition-A for 4 hours at 495°C and 550°C, respectively, followed by air cooling. ASTM A693 standard [87] is followed for the precipitation hardening treatments of 17-4 PH stainless steel.

Table 3-1 Materials details.

Material	Company	Specifications and Comments
Ti-6Al-4V Alloy	Titanium Industries, Inc. Montreal, Canada	ASTM B265, Grade 5
17-4 PH Stainless Steel (3 conditions)	Sandmeyer Steel Philadelphia, USA	ASTM A693-06
X22CrMoV12-1 Stainless Steel	ALSTOM Power Switzerland	A steam turbine blade material
2024-T4 Al alloy 7075-T6 Al alloy	McMaster-Carr. Elmhurst, Illinois, USA	ASTM B209

3.1.2 Properties of Test Materials

Basic and mechanical properties of the tested alloys relevant to the work are presented in Table 3-2. Hardness of these alloys was measured (as will be detailed later), while other properties were obtained from the open literature. These properties will be used to analyze the response of the tested materials to water droplet erosion.

Table 3-2 Properties of the tested materials relevant to the present work.

Material	Density (g/cm^3)	Speed of Sound (m/s)	Elastic Modulus (GPa)	Avg. Fracture Toughness ($MPa\sqrt{m}$)	Measured Hardness (Hv)	References
Ti-6Al-4V	4.43	5072	114	65	338	[88,89]
17-4 PH Steel	7.78	5006	195	90	360	[90,91]
X22CrMoV12-1 Steel	7.75	5316	219	100	310	[92,93]
7075-T6 Al	2.81	5026	71.7	35	187	[88,94]
2024-T4 Al	2.78	5124	73	38	149	[95,96]

3.1.3 Sample Preparation

Samples from the tested materials were prepared for erosion tests and the different characterization experiments. For erosion tests, the as-received strips of the five test materials were first cut to smaller pieces having each the dimension of 25×9×3.5 mm. These pieces were then hand-ground with silicon-carbide papers to arrive at the coupon (or insert) shape that – with the use of nut, bolt and washers - fits smoothly and tightly into the sample holders. Figure 3-1 illustrates how the coupons are secured to the sample holder as well as the approximate final dimensions of the coupon after the grinding process. Finally, the test surface of all coupons was progressively ground and finished to a 1200 grit silicon-carbide. In this way similar surface finish was ensured for all samples, and the influence of different initial surface roughness on the erosion response is avoided [78].

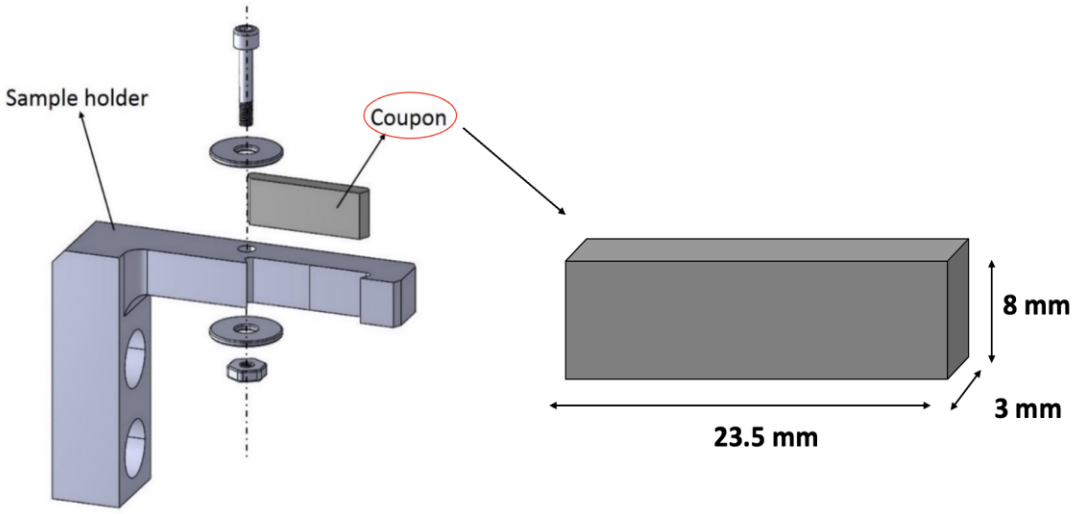

Figure 3-1 Coupon sample holder assembly.

3.1.4 Materials Used for the Specific Thesis Objectives

In general, a wide range of materials is needed to validate mathematical models and demontstrate their prediction capabilities. As such, all five alloys are included in studying the threshold velocity (thesis objective 1 & 2).

However, only **Ti-6Al-4V** is considered in investigating the evolution of hardness and roughness during the incubation period (thesis objective 3). This is because, among metallic materials, Ti-6Al-4V is the most studied material in water droplet erosion investigations. As such, understanding its roughening behavior will be valuable to water droplet erosion literature. Moreover, it is reasonable to assume that role of roughening and surface hardening can be demonstrated with one alloy without the need to duplicate the testing efforts.

As for investigating the role of strain hardening exponent (thesis objective 4), only **17-4 PH stainless steel** is considered. Each of the two discussed aging treatments of 17-4 PH has a different set of mechanical proeprties. As such, variation in the strain hardening exponent (n) is achieved. Moreover, by studying the same material with differet conditions, the influence of grain structure and rate sensitivity is minimized. This facilitates inferring the influence of the strain hardening exponent (n) without the risk of having other confounding factors.

3.2 Erosion Testing

3.2.1 Erosion Test Rig

In this work, all erosion tests were performed on a rotating test rig located at Concordia University and shown in Figure 3-2. The test rig allows accelerated erosion experiments to be conducted in accordance with the ASTM G73 standard [97]. It consists of an 18-inch (~ 45 cm) disc rotating horizontally in a closed chamber. The chamber can be maintained under 30-50 mbar vacuum pressure during tests, which helps to minimize the air friction. This is crucial because friction can result in considerable temperature rise that may cause droplets evaporation during erosion tests. The disc is driven by a compressed-air turbine operating with 100 psi pressure. The impact velocity in this rig is considered as the linear speed of the rotating disc at the point of impact. The rotational speed of the disc can reach up to 20,000 rpm, which allows the impact velocity to be varied up to 500 m/s.

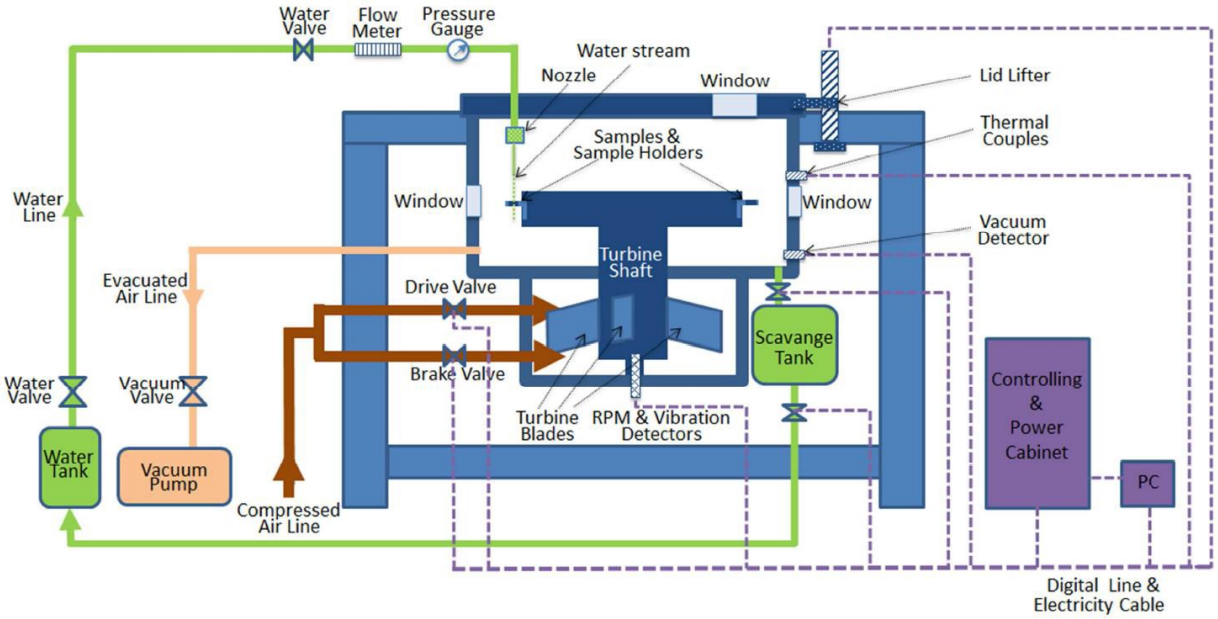

Figure 3-2 Schematic of water droplet erosion rig.

The rig is also equipped with a computer and a special software. The software enables the operation, control and real-time monitoring of various operating parameters such as rotational speed, chamber pressure, vibration level, chamber temperature, and bearing temperature.

3.2.2 Droplet Generation System

Water droplets are introduced to the rig through droplet generation system. This system, illustrated in Figure 3-3, consists of a water reservoir, a rotary pump and waterflow control units (valves and flowmeters). Water is pumped from the reservoir to the nozzle located inside the chamber of the erosion rig. Through controlling the flow rate and water line pressure, the nozzle can generate a water streak that consists of discrete droplets.

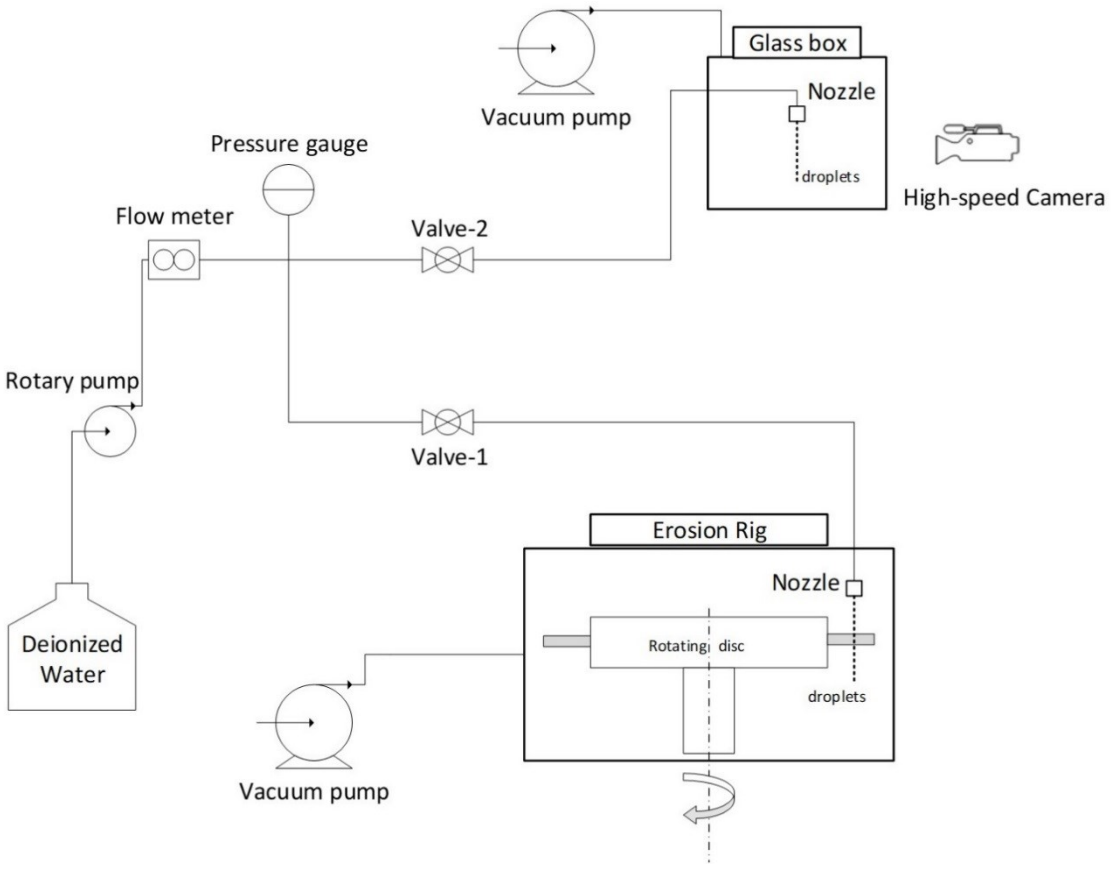

Figure 3-3 Schematic of water droplet generation system.

Two nozzles, having orifice diameters of 400 and 600 μm, are used in this work. Each nozzle is characterized before being installed in the erosion rig. During the characterization process, the nozzle is installed in a separate transparent "glass box" that simulates the condition inside the rig as shown in Figure 3-3. Water is introduced to the nozzle in the glass box (through valve-2), and a high speed camera is used to observe the streak generated from the nozzle. Then, the line pressure and water flow rate are continuously adjusted until the desired break-up distance (i.e., the distance at which the falling water streak breaks into discrete droplets) is achieved for each nozzle. Since not all droplets breaking-up from the water streak have the same size, the diameter of 200 droplets was measured and their size distribution is plotted for each nozzle. The resulting size distributions are shown in Figure 3-4 and Figure *3-5* for 400 and 600 μm respectively.

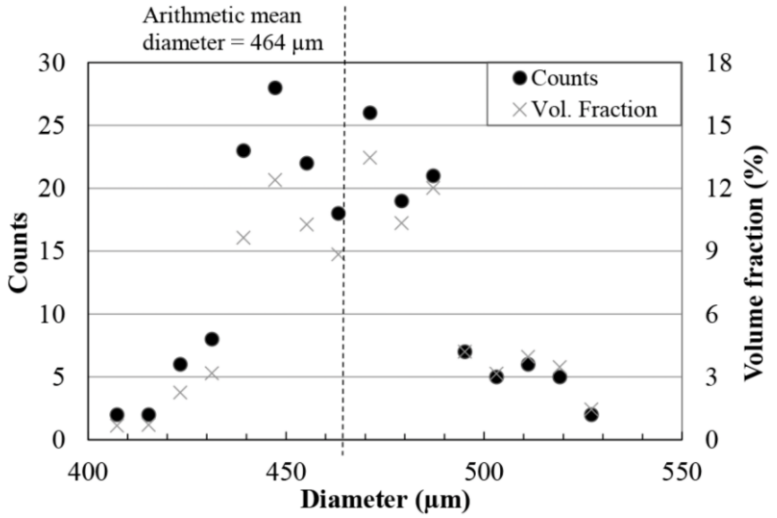

Figure 3-4 Droplet size distribution of a 400 μm nozzle [98].

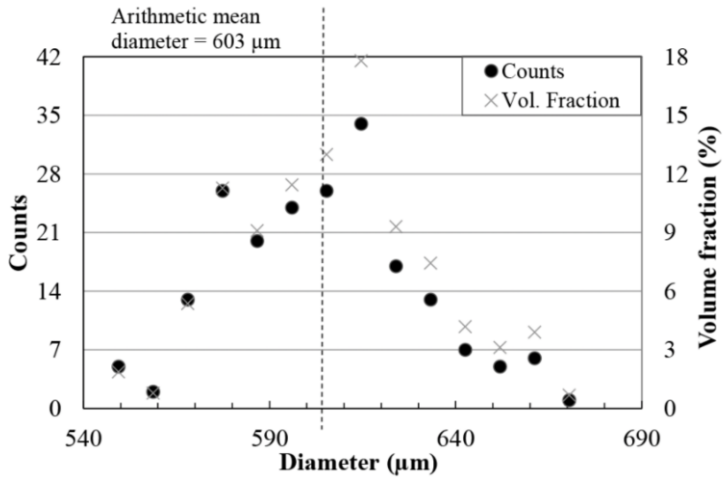

Figure 3-5 Droplet size distribution of a 600 µm nozzle [98].

Table 3-3 summarizes the characteristic of the two nozzles used in this work. For each nozzle, the arithmetic mean diameter of 200 droplets (as shown in Figure 3-4 and Figure 3-5) is considered the defining average droplet size. This was found to be 464 µm and 603 µm for 400 and 600 nozzles respectively. The number of droplets impacting the surface of a coupon (the width of which is 8 mm according to Figure 3-1) per each revolution as well as the area exposed to droplet impact (i.e., impact area) were also measured for the two nozzles. The number of droplets per revolution were found to be 6 and 4 droplets for 400 and 600 nozzles respectively. The area exposed to droplet impact is 4.8 mm^2 in case of 400 nozzle, and 6 mm^2 in case of the 600 nozzle [98].

Table 3-3 Details of the used droplet generation nozzles.

Nozzle	Break-up distance (cm)	Average Droplet size (µm)	Number of droplets per revolution	Area exposed to water droplet (mm^2)
400	5	464	6	4.8
600	5	603	4	6

3.2.3 Test Procedure

A single erosion test is performed in several cycles (or intervals) until the full duration of the test is completed. During a test interval, the coupon-holder assembly (shown in Figure 3-1) is mounted on the periphery of the disc. Then, the disc is rotated to a specific speed (in rpm) so as to achieve a desired test impact velocity. When the desired impact velocity is achieved, water droplets are introduced to the chamber through the nozzle such that test surface of the coupon experiences normal droplet impacts (90°). At the end of the interval, water flow is cut to stop the droplets impact and the disc is gradually brought to stop. The water accumulated during the erosion test in the chamber is drained to a scavenge tank beneath the chamber. The test chamber is pressurized to atmospheric pressure before the samples are removed from the disc. The samples are removed from the disc and cleaned thoroughly. The samples are then weighed on a sensitive balance to measure the eroded mass (if any). Images of the test surface are also taken during the interruption intervals. In some tests, scanning electron microscopy (SEM), roughness and hardness measurements are performed on the impact area at selected intervals. Samples are then mounted to the rig and next test interval is started. The WDE test parameters studied in the present thesis are summarized in Table 3-4.

Table 3-4 Erosion test parameters and conditions used.

Test Parameter	Value
Linear impact speed (m/s)	350, 300, 250, 225, 200, 175, and 150
Average droplet size (μm)	464 and 603
Flow rate (liters/min)	0.05 and 0.1
Impact angle (°)	90
Test chamber pressure (mbar)	30-50
Initial waterline pressure (psi)	30

The number of intervals, duration of each interval, and hence the total duration of an erosion test, depend on test parameters and the objective of the erosion test. This could be tests carried out to evaluate the threshold velocity, incubation period, or to obtain the full erosion curve for a certain material.

Number of Incubation mpacts. In this work, the duration of the incubation period at a specific impact velocity is indicated by either "time" or "number of droplet impacts" needed to result in a mass loss of 0.1 mg. This also corresponds to the appearance of a uniform pitting in impact area. The conversion between erosion "time" and "number of impacts" is achieved through the following equation:

$$Number\ of\ Incubation\ impacts\ (N) = RPM * incubation\ time\ (min) \qquad (3\text{-}1)$$

The number of incubation impacts (N) is used to construct the $V - N$ erosion curve, from which the threshold velocity is inferred. This will be detailed in the following chapters.

3.3 Characterization

Various characterization techniques were utilized in the present work to obtain information that helps in analyzing the erosion test results for a particular objective. These include mass loss measurement, optical imaging, scanning electron microscopy (SEM), hardness and surface roughness measurements. Equipment used and the purpose of utilizing each of these techniques are detailed in the ensuing discussion.

3.3.1 Mass Loss Measurement and Optical Imaging

A high precision balance (having $\pm$ 0.1 mg accuracy) was utilized to measure the samples at every test cycle\interval. This was done to calculate the mass lost during the interval so that

the erosion curves (i.e., Figure 1-5) could be constructed. Simultaneously, a standard stereo optical microscope was also employed to visually observe the progression of erosion damage during erosion tests. Optical macrographs of the impact area were obtained for each interval during the tests.

3.3.2 Scanning Electron Microscopy

Scanning electron microscope (SEM, Hitachi S-3400 N) was used to examine the surface of the tested samples. SEM micrographs of the coupons were first obtained before the erosion tests. Then, for specific test samples, SEM analysis of the impacted area at selected test intervals were performed to reveal and measure damage features as well as to identify potential erosion damage mechanisms. Moreover, micrographs of the cross section of selected samples were also obtained. For this purpose, samples were cut at the desired cross section using a slow cutting machine. The samples were then mounted in epoxy and polished with up to 1 μm diamond suspension. The polished cross sections were then examined by SEM.

3.3.3 Hardness Testing

Vickers hardness testing machine (Mitutoyo MVK-H1) was utilized to measure the hardness of the tested samples. Load of 300 gf for a holding time of 15 seconds was utilized for the five alloys used in this work to avoid discrepancy that may result from using different loads. An average of 10 readings was considered for each hardness data point. At first, the initial surface hardness of all tested coupons was measured before the erosion test. Then, hardness of the impacted area was evaluated at several test intervals during the incubation period such that droplet hardening process is evaluated.

3.3.4 Roughness Measurement

Surface roughness was measured using Confocal Laser Scanning Microscope (CLSM, LEXT-OLS4000, Olympus, Japan). CLSM enables a non-destructive scanning of the 3D surface topography, which helps in assessing surface roughness of the tested samples at various intervals during erosion tests. In this work, the initial average surface roughness (S_a) of test samples were routinely measured before erosion tests to ensure that test pairs have similar roughness. Moreover, the average surface roughness (S_a) and skewness (S_{sk}) were evaluated at every test interval during an erosion test performed on Ti-6Al-4V with 603 μm droplets at 250 m/s. This was done to study the influence of droplet impingements on the evolution of surface roughness (i.e., roughening). The use of average surface roughness and skewness is favored due to their consistency in terms of trend seen in the variation of values between each interval during erosion tests [58].

Further details - about how each of the above-mentioned experimental techniques is appropriated to a specific thesis objective – will be given at the pertinent chapter. Beside the presented experimental equipment, Finite Element Analysis (FEA) of impact stress is performed in collaboration with Dr. Mason Marzbali from American University in Dubai. Details about the finite element analysis are presented in Chapter 5 and Appendix-B.

4 THE THRESHOLD VELOCITY

This chapter presents the results of work done on the threshold velocity in water droplet erosion. The first section of the chapter discusses the theoretical part of the work, which consists of model formulation and predicted values of the threshold velocity. The following section outlines the experimental procedure proposed in this work to evaluate the threshold velocity. Finally, the chapter ends with discussion and comparison between the experimental and theoretically predicted values of the threshold velocity.

4.1 Prediction of the Threshold Velocity

4.1.1 Formulation of the Prediction Model

As mentioned, first principles analysis of water droplet erosion is an extremely difficult endeavor. Instead, assumed damage mechanisms are often used to drive analytical models. For predicting the threshold velocity, the current work draws from two areas in solid mechanics; the theory of dynamic threshold for crack propagation and dynamic fracture and wear of metals. These are summarized in Figure 4-1.

The use of dynamic threshold for crack propagation theory in predicting the threshold velocity was motivated by the conclusions from microscopic observations of eroded metals. It has been shown [82,99] that cracks nucleation and propagation are the main microscopically observable material removal mechanisms in metals. As such, at some level, the threshold velocity in water droplet erosion can be viewed as the condition where crack propagation is absent. In other words, at the threshold condition, the stress impulse caused by the impingement of a liquid

droplet has an amplitude that is neither sufficient to initiate new nor to propagate pre-existing cracks.

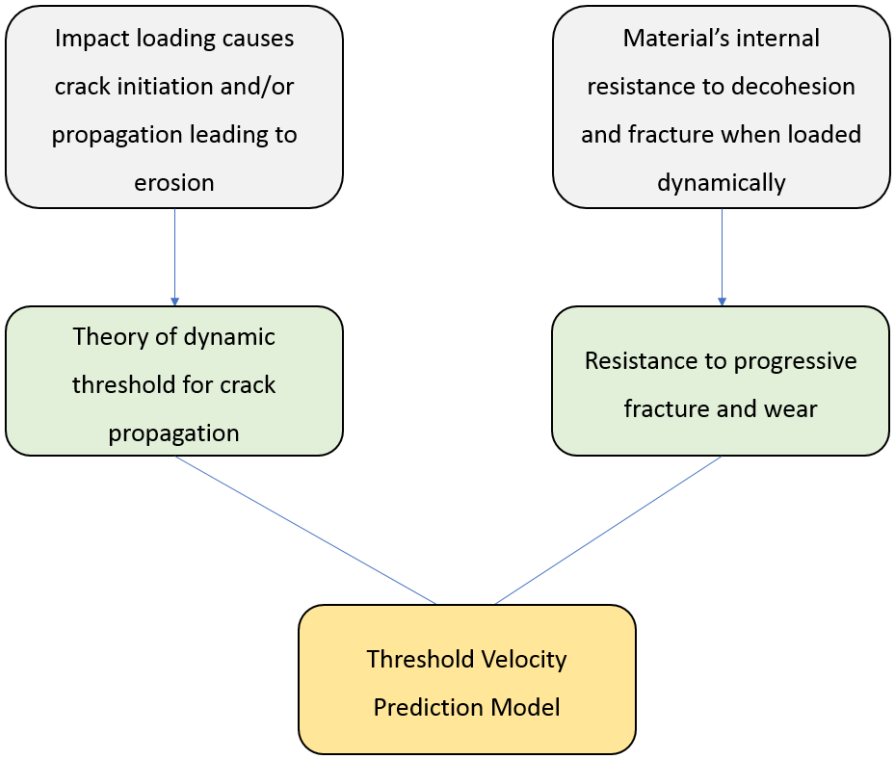

Figure 4-1 Basic assumptions of the threshold prediction model.

On the other hand, the use of dynamic fracture and wear of materials was motivated by the need to derive an expression for the erosion resistance of the target material at the threshold condition. The assumption was that, at the threshold velocity, the material has an internal erosion strength property that matches (in magnitude) the impact pulse, and hence preventing stress buildup and the eventual fracture of the material. Since, water droplet erosion is a dynamic process, this erosion strength can be viewed as the ability of the material to resist dynamic fracture.

Based on the preceding discussion, the formulation of the model was done in two parts. The first part is the mathematical modeling of the dynamic threshold condition for crack propagation. This was based on the work of Steverding and Lehnigk [100], where a differential equation that describes the process of dynamic crack propagation subjected to a tension pulse (σ) of a certain amplitude was developed. The equation was formulated for failure phenomena where ***time*** is considered as an active independent parameter (e.g. fatigue, fracture, yielding, etc.), which encompasses water droplet erosion phenomenon. The equation is as follows:

$$\left(\frac{4\rho\sigma^2}{Eh^2}\right)\ddot{c}c^7 + \left(\frac{26\rho\sigma^2}{Eh^2}\right)\dot{c}^2c^6 + \left(\frac{C_s\,\rho\sigma^2}{Eh^2}\right)\dot{c}c^7 = \frac{\sigma^2c^4}{2} - \frac{\gamma\,Eh^2}{3} \qquad (4\text{-}1)$$

where E is the elastic modulus, c is crack length, ρ is the density of the material, C_s is the speed of sound in the solid, γ is the specific surface energy, and $h = C_s\,t$, where t is time. In this main differential equation 4-1, the threshold conditions are considered as the limiting case where the repeated loading impulses are not enough to cause crack propagation (i.e. all derivatives of crack length are equal to zero). Therefore, the differential equation for crack propagation (equation 4-1) can - at threshold condition - be reduced to the following form [100]:

$$\sigma^2\,\frac{t}{2\,E} = C \qquad (4\text{-}2)$$

where σ is the pulse (stress) amplitude, t is the time duration of the pulse, E is the elastic modulus of the material, and the constant C depends on the mechanical properties of the material. For most of materials, especially metals, the elastic modulus is almost structure insensitive. Therefore, equation 4-2 can be written as:

$$\sigma^2\,t = C \qquad (4\text{-}3)$$

For water droplet impingement erosion, the impact pulse can be approximated by the water hammer pressure as follows [9]:

$$\sigma = P = \rho_l C_l V \qquad (4\text{-}4)$$

where V is the impact velocity, $\rho_l \; and \; C_l$ are the density and speed of sound in the liquid respectively. The duration of the impact pressure pulse is given as [24]:

$$t = \frac{d\,V}{2\,C_l^2} \qquad (4\text{-}5)$$

where d is the size of the impacting droplet. Substituting equations 4-4 and 4-5 into equation 4-3 and considering the impact velocity V to be the threshold velocity V_c results in:

$$\rho_l^2\, V_c^3\, d = C \qquad (4\text{-}6)$$

Equation 4-6 gives the threshold velocity V_c at a given droplet size d. The constant C in equation 4-6 characterizes the material's resistance to the probability that decohesion of a certain volume of matter occurs at a given area (for our case, the impacted area). As such, the second part in the formulation of the prediction model is defining C in equation 4-6 from the basic properties of materials. This was based on the theory of dynamic fracture and wear of materials. For dynamic fracture of brittle materials, the constant C in equation 4-6 can directly be linked to the specific surface energy γ (which in turns can be linked to fracture toughness) and the speed of sound in the material as shown in [100]. The primary focus of the current work, however, is metallic materials. For ductile metals, non-conservative forces (such as plastic deformation and strain hardening) may become active during the impact process. This entails that mechanical properties of the material that are responsible for the mechanisms by which matter is separated from the surface should be considered. Considering metals resistance to dynamic wear phenomena and following the work of Freund [101] and Hornbogen [102], one can deduce that the constant C in equation 4-6 maintains the following proportionality:

$$C \propto \frac{\sigma_y\, K_{IC}^2}{E} \qquad (4\text{-}7)$$

where, σ_y and K_{IC} are the yield strength and fracture toughness of the material respectively. Substituting equation 4-7 in equation 4-6 yields:

$$\rho_l^2 \, V_c^3 \, d = k \, \frac{\sigma_y \, K_{IC}^2}{E} \qquad (4\text{-}8)$$

where k is the proportionality constant. The constant k in equation 4-8 must have a unit of s/m to achieve dimensional consistency. This may indicate that k is related to the speed of sound in the solid material. The presence of speed of sound in the equation can be linked to the material's ability to impede crack propagation. Following the work of [100], we consider the constant k to be $1/2C_s$, where C_s is the speed of sound in the solid. Therefore, Equation 4-8 can then be written as:

$$V_c^3 \, d = \frac{\sigma_y \, K_{IC}^2}{2 \, \rho_l^2 \, E \, C_s} \qquad (4\text{-}9)$$

Equation (8) can be rearranged as:

$$V_c = \left(\frac{\sigma_y \, K_{IC}^2}{2 \, \rho_l^2 \, E \, C_s \, d} \right)^{1/3} \qquad (4\text{-}10)$$

Equation 4-10 gives the threshold velocity V_c at a given droplet size d, depending on the properties of the impacting liquid and the solid material. The challenge of accurately predicting threshold velocity values using equation 4-10 lies partially on the precise determination of mechanical properties representative to the dynamic, high strain rate, repetitive nature of water droplet impingement erosion. Whenever available, dynamic yield strength σ_{yD} and dynamic fracture toughness K_{ID} should be used instead of their quasi-static values.

4.1.2 Theoretical Evaluation of the Threshold Velocity for the Tested Materials

The theoretical values of the threshold velocity of the five metallic alloys are calculated using equation 4-10 for the two droplet sizes considered in this work (i.e., 460 µm and 600 µm). Density of the liquid is considered to be that of water (1000 kg/m^3). For the solid materials, speed of sound, elastic modulus, and fracture toughness values listed in Table 3-2 are considered. Yield strength values are derived from hardness measurements as shown in Table 4-1. This was done to obtain localized yield strength values that best represent the condition in water droplet erosion. The use of localized yield strength from hardness was introduced and validated by Ahmad *et al.* [4]. Tiryakioğlu [103] provided an equation that evaluates the yield strength from Vickers hardness for aluminum alloys. His [103] equation was employed for the two alumium alloys of this work. Whereas for steels and Ti-6Al-4V, yield strength was considered to be one-third of the Vickers hardness value [104].

Table 4-1 Yield strength from hardness measurements.

Material	Hardness, Hv (MPa)	Yield Stress (MPa)	Converting Equation	References	Theoretical Threshold Velocity (m/s)	
					460 µm	600 µm
17-4 PH	360 (3531)	1177	$\sigma_y = \frac{H_v}{3}$	[104]	219	201
Ti-6Al-4V	338 (3315)	1105			207	191
X22CrMoV12-1	310 (3040)	1015			211	194
7075-T6	187 (1834)	702	$\sigma_y = \frac{H_v}{2.61}$	[103]	137	126
2024-T4	149 (1461)	560			132	121

Theoretically calculated threshold velocities are shown in Table 4-1. It can be observed from Table 4-1 that stainless steels (17-4 PH and X22CrMoV12-1) have the highest threshold velocity, whereas aluminum alloys (2024-T4 and 7075-T6) have the lowest values. This is expected because

the stainless steels are known to have high erosion resistance compared to the other alloys tested in this work. Interestingly, the threshold velocity of Ti-6Al-4V is only slightly lower (5%) than that of 17-4 PH stainless. This is because Ti-6Al-4V has a lower elastic modulus with relatively high hardness induced yield strength, which according to equation 4-10, are expected to result in high threshold velocity. The next section discusses the experimental threshold velocity.

4.2 Experimental Threshold Velocity

As mentioned before, experimental evaluation of the threshold velocity is an erosion testing conundrum. This is because the threshold velocity indicates the condition where no erosion is to be detected even for an infinite number of droplet impacts, while erosion tests can not be run indefinitely. This necessitates a test criterion to indicate the end of the threshold erosion experiments. In this work, we developed an experimental procedure and a criterion to evaluate the threshold velocity. The developed criterion and the experimental values of the threshold velocity for the five tested materials are discussed in sections 4.2.1 and 4.2.2, respectively.

4.2.1 Threshold Velocity Evaluation Criterion

To evaluate the threshold velocity (at a given droplet size), the number of the droplet impacts needed to end the incubation period (beginning of damage) was first plotted against impact velocity. This results in a curve (shown in Figure 4-2) that is analogous to fatigue $S-N$ curve and will be referred to henceforth as "$V-N$ erosion curve". As illustrated in Figure 4-2, each point on the $V-N$ curve represents the number of droplet impingements necessary to initiate erosion damage (end of incubation period in mass loss curve) for test conducted at a particular impact velocity. As can be seen from Figure 4-2, the higher the impact velocity, the

smaller the number of incubation impacts. Figure 4-2 also illustrates the influence of droplet size on the $V-N$ curve, where d_2 represent the larger average droplet size and d_1 represent the smaller one. The larger the droplet size, the lower the $V-N$ erosion curve, and hence, the lesser the number of droplet impingements to failure.

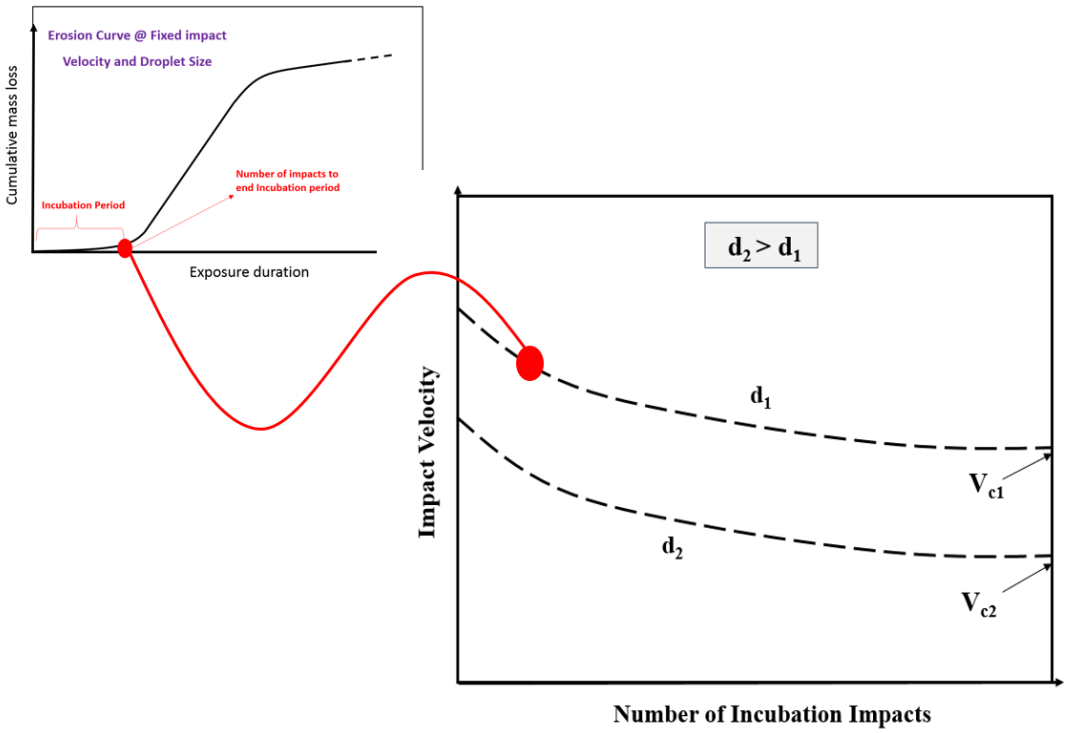

Figure 4-2 Impact velocity against number of incubation impacts ($V-N$) curve.

Ideally, threshold velocity should be the impact velocity that results in an infinite number of incubation impacts. This should correspond to a knee or a plateau in the $V-N$ erosion curve in a way that is analogous to the endurance limit in fatigue $S-N$ curves. However, It is to be mentioned that, for rotating erosion testing devices, the $V-N$ erosion curve can be approximated through the following power law [42]:

$$V = a\,N^{\,n} \qquad (4\text{-}11)$$

where V is the impact velocity, N is the number of impacts to end the incubation period, a and n are constants depending on material properties, liquid properties, and droplet size. Equation 4-11, when plotted in a log-log scale, results in a linear relationship suggesting that lower impact velocities can still result in erosion even after excessively long exposure duration to droplet impacts. For this reason, the threshold velocity in this work is disassociated from the plateau in $V - N$ erosion curve. In other words, it is not necessary to arrive at plateau in the $V - N$ erosion curve in order to estimate the threshold velocity. Rather, a testing criterion where the absence of erosion damage after a specific/particular number of impacts (test duration) is considered as indication of the threshold condition. This is analogous to the way in which fatigue strength is defined (e.g. at a particular number of cycles) in studies of fatigue properties of materials that show no clear sign of endurance. Based on this, the threshold velocity is considered the impact velocity at which 1 million droplet impacts per mm^2 is not enough to cause erosion damage. In our erosion rig, 1 million per mm^2 is equivalent to 1 million test cycles.

The choice of the 1 million droplet impact per mm^2 is based on practical in-service erosion lifetime. To arrive at this number, the following assumption was first made:

For a component operating under environment containing liquid droplets, threshold condition is met if the component completed its intended service life without experiencing erosion damage initiation.

In other words, the threshold velocity is considered as the impact velocity at which the total number of droplet impingements over an area of mm^2 during the entire service life of a component is less than the number of impacts needed to end the incubation period in that area. Secondly, based on the first assumption, calculations (shown in **Appendix-A**) that utilize meteorological rain and wind turbine statistics have been performed to show that 20 years of service of a wind turbine blade are not enough to result in 1 million raindrop impacts over an

area of 1 mm^2 even in extreme rain conditions. This can safely be extended to gas and steam turbine applications, where the design lifetime of the blades in compressor of gas turbines and in the blades of low pressure stage of steam turbines are shorter than that of wind turbine blades, and the size of droplets encountered in these applications are much smaller compared to raindrops [9].

Therefore, lack of signs of erosion damage after 1 million droplet impacts per mm^2 is adopted and proposed to WDE researchers as a criterion to evaluate the threshold velocity.

4.2.2 $V - N$ Curves and Experimental Values of the Threshold Velocity

Figure 4-3 shows V − N erosion curves of the tested materials for the two droplet sizes 460 µm and 600 µm. As mentioned earlier, each data point on the $V - N$ erosion curves represents the number of droplet impacts needed to end the incubation period when the test is performed at a particular impact velocity. Red empty circles and diamonds in all curves indicate that at the corresponding impact velocities, 1 million cycles were not sufficient to cause any detectable erosion damages. The impact velocity corresponding to these particular experiments is considered the threshold velocity of the material. Table 4-2 lists values of threshold velocity of materials for droplet sizes of 460 and 600 µm. The 17-4 PH stainless steel has highest threshold velocity compared to the rest of the alloys due to its high strength and hardness property. Similar to the theoretical values, the threshold velocity of Ti-6Al-4V, however, is only slightly lower than that of 17-4 PH due to its lower value of elastic modulus, which results in greater ultimate resilience that is reported to play an important role in the overall erosion strength of the alloy [59].

Additional data point representing a prolonged test that was performed on Ti-6Al-4V alloy at an impact velocity of 175 m/s and droplet size of 460 µm is shown in *Figure 4-3* (b).

This was done to verify that the region below the threshold velocity is considered a safe region even if the material is exposed to extremely large number of water droplet impingements. Although a clear plateau in the V-N erosion curve could not be guaranteed in this experiment, no sign of erosion could be detected after close to 6 million cycles. This indicates that the experimental approach proposed and followed in this work to evaluate the threshold velocity is sound.

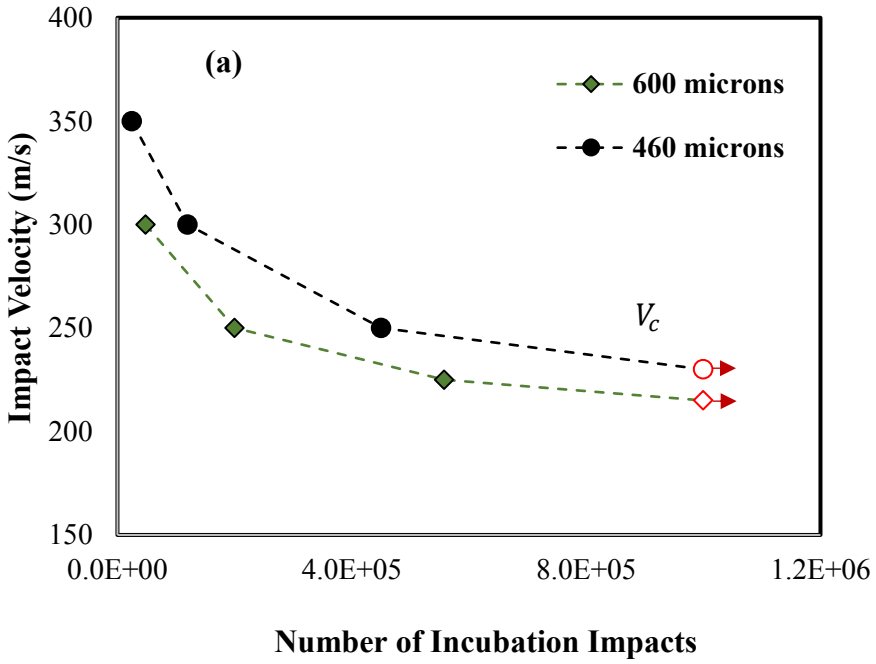

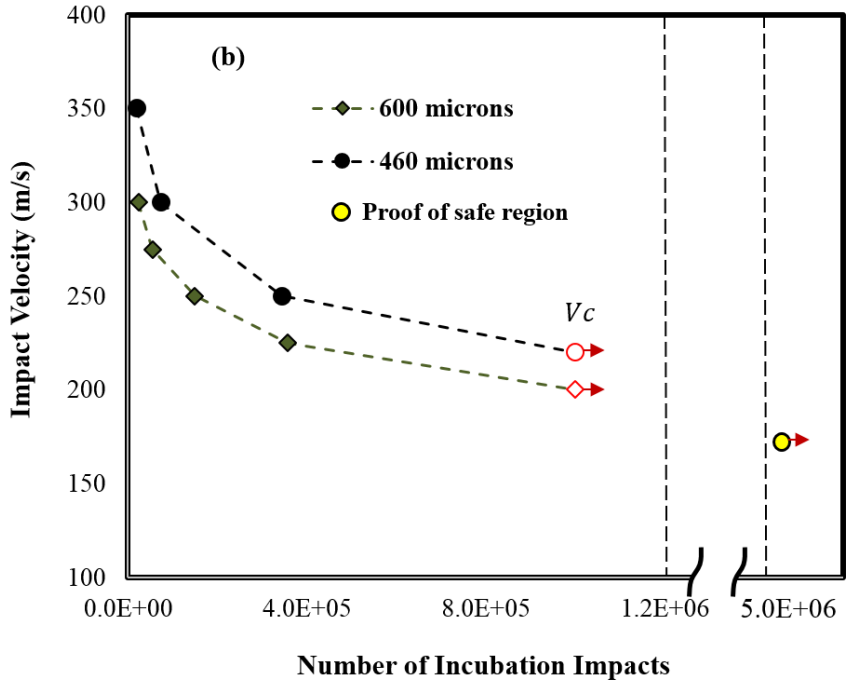
(b)
600 microns
460 microns
Proof of safe region
Vc
Impact Velocity (m/s)
400
350
300
250
200
150
100
0.0E+00
4.0E+05
8.0E+05
1.2E+06
5.0E+06
Number of Incubation Impacts

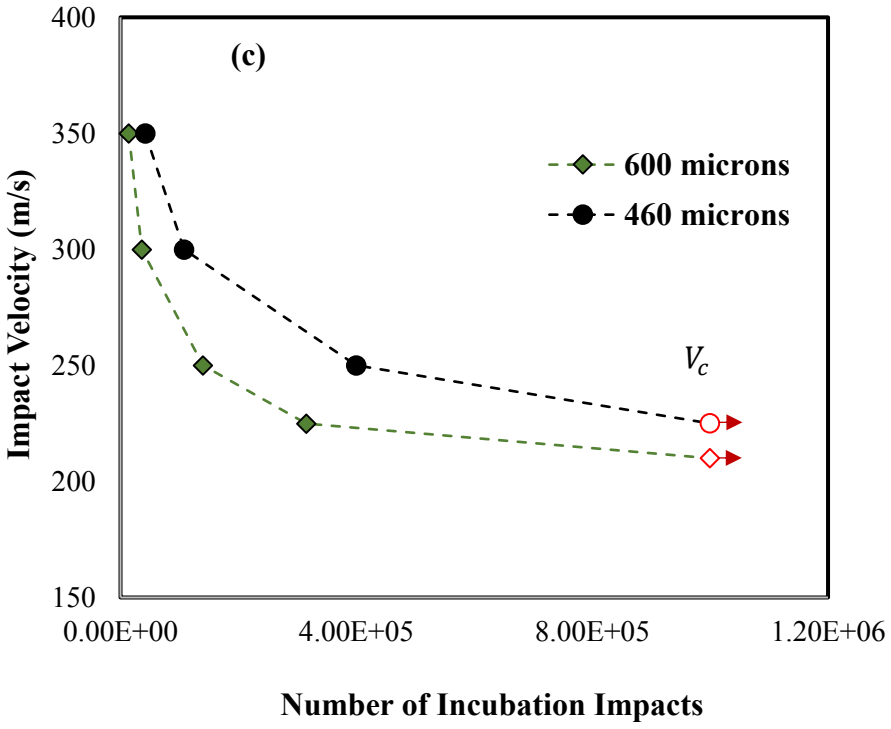
(c)
600 microns
460 microns
Vc
Impact Velocity (m/s)
400
350
300
250
200
150
0.00E+00
4.00E+05
8.00E+05
1.20E+06
Number of Incubation Impacts

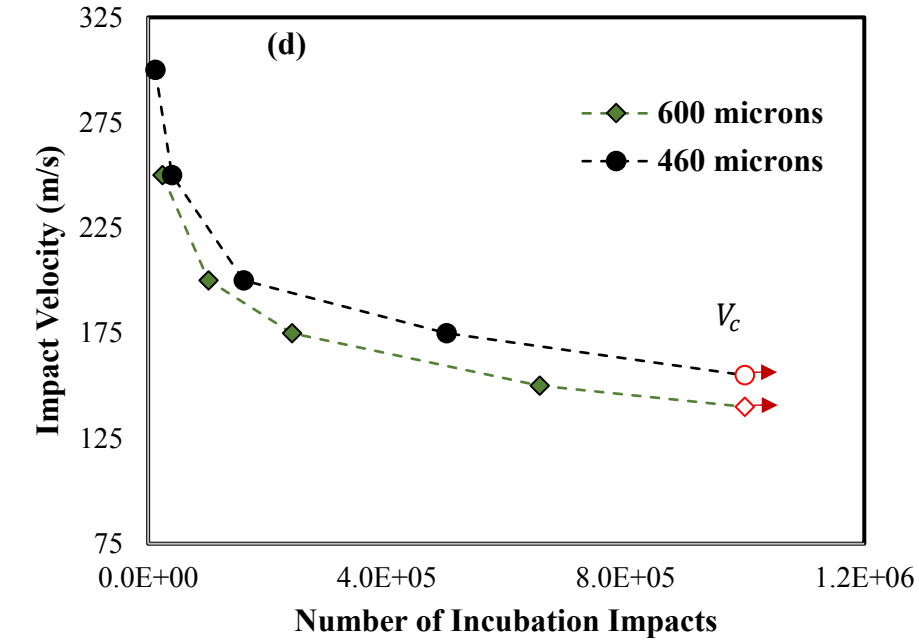

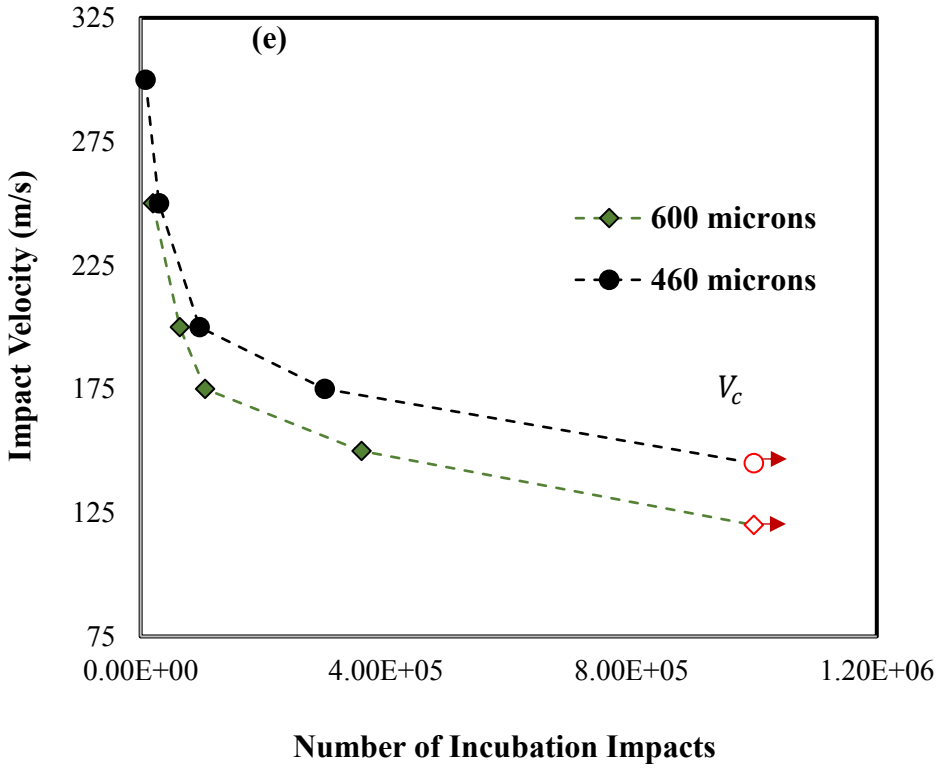

Figure 4-3 $V - N$ erosion curves; (a) 17-4 PH Stainless Steel, (b) Ti-6Al-4V Alloy, (c) X22CrMoV12-1 Stainless Steel, (d) 7075-T6 Aluminum Alloy, and (e) 2024-T4 Aluminum Alloy.

Table 4-2 Experimental and theoretical values of threshold velocity

Material	V_c (m/s) at d=460μm		V_c (m/s) at d=600μm	
	Experimental	**Theoretical**	**Experimental**	**Theoretical**
17-4 PH steel	230	219	215	201
Ti-6Al-4V	220	207	200	191
X22CrMoV12-1	225	211	210	194
7075-T6	155	137	140	126
2024-T4	145	132	130	121

4.3 Discussion

4.3.1 Comparison Between Theoretical and Experimental Threshold Velocity

It can be noted from Table 4-2 that the theoretical threshold velocities of the tested materials are very close to the experimentally measured values. This indicates the accuracy of the developed model. In general, the predicted threshold velocity is slightly lower than the experimentally measured values. The difference between theoretical and experimental threshold velocities can be attributed to two main reasons. The first one is the difficulty associated with obtaining mechanical properties representative of the high strain rate impact condition (up to 10^6 s^{-1} [47]) that is characteristic of water droplet erosion [105,106]. This applies in particular to the dynamic fracture toughness because it is raised to power 2 in the developed model. Bragov *et al.* [107] provided a relationship to deduce dynamic fracture toughness value from the quasit-static fracture toughness. Such relationships can be very useful given the difficulty associated with experimentally evaluating dynamic fracture toughness [106].

The other reason behind the discrepancy between experimental and theoretical values perhaps pertains to the outlined experimental approach employed to evaluate the threshold velocity. As mentioned, threshold velocity is considered to be the impact velocity where 1 million impingements per mm^2 are not sufficient to cause erosion damage. Admittedly, this approach only constitutes a practical methodology to evaluate threshold velocities and does not inherently account for microscopic phenomena taking place in the threshold regime, such as elastic stress ranges and absence of crack initiation and propagation. Such microscopic phenomena demand an extremely precise single droplet impact erosion devices, which is not currently available in the open literature. This might have resulted in slight over or underestimation of the precise value of the threshold velocity. However, an important observation is made when the evolution of hardness due to droplet impingements on Ti-6Al-4V is evaluated and compared for two different erosion tests (both performed with droplet size of 600μm). One test was performed for samples impacted at 250m/s which is higher than V_c, while another was performed at the threshold velocity (200m/s). Hardness was measured at 4 intervals during each test. The results are summarized in Figure 4-4. At 250 m/s, it can be seen from Figure 4-4 that remarkable hardening occurs due to droplet impacts. However, when erosion test is performed at the threshold velocity, the change in hardness due to droplet impacts is insignificant. Hardening during incubation period stage has traditionally been attributed to the accumulation of plastic strain due to deformation caused by droplets impact [38]. This may indicate that the maximum impact stress corresponding to threshold velocity is not sufficient to produce material flow, and the material could be responding in a completely elastic manner. This demonstrates the practical significance of the threshold velocity and corroborates the effectiveness of the outlined experimental criterion for threshold velocity evaluation.

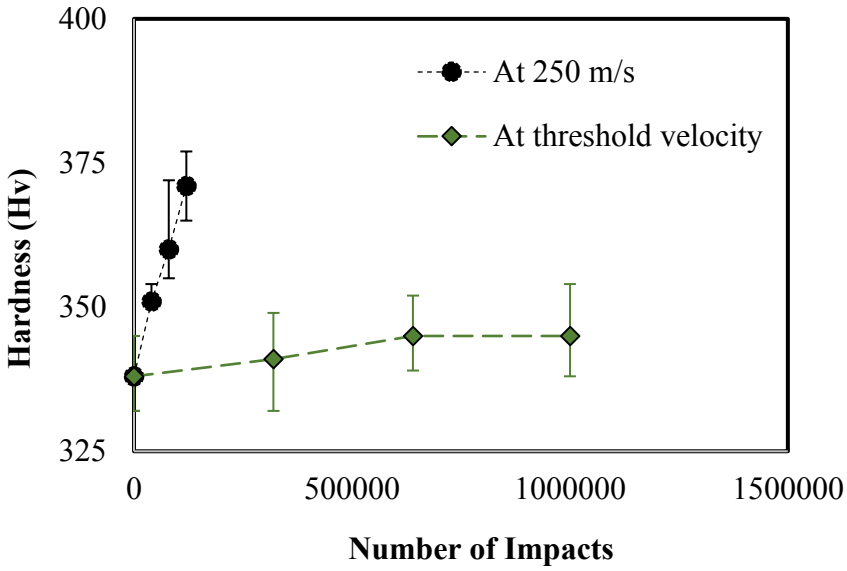

Figure 4-4 Evolution of hardness during erosion test performed on Ti-6Al-4V with droplet size of 600 μm.

4.3.2 Comparison Between the Developed Model and the Literature's

The developed model is compared to that of Thiruvengadam's [53] (i.e., equations 2-1 and 2-2) for the five materials tested in this work. This is because Thiruvengadam's [53] model has been the only prediction model where the threshold velocity can directly be estimated from liquid and material properties. Values of endurance limit of the tested materials were obtained from the literature [88,95,108,109] and used to calculate threshold velocity according to equation 2-1. It can be seen from Figure 4-5 (a) that the present model matches the experimental results more accurately than Thiruvengadam's model [53].

Furthermore, the validity of the current model beyond the experimental data of this work was examined using experimental threshold velocity values obtained from the literature for four different materials. These experimental threshold values were extrapolated from erosion data of incubation periods provided at different impact velocities. Table 4-3 provides details about the

references and test conditions from which these threshold values are extracted. Then, the corresponding threshold velocities for these four materials were predicted by the present model and that of Thiruvengadam [53], as shown in Figure 4-5 (b). It can be seen from Figure 4-5 (b) that the developed model predicts the threshold velocity of literature data with reasonable accuracy. Moreover, the present model is more precise than that of Thiruvengadam's [53]. Also, Thiruvengadam's [53] model does not take into consideration the influence of droplet size. This results in predicting a single threshold velocity value for each material. Whereas the threshold velocity value depends on the droplet size, which is captured by the present model.

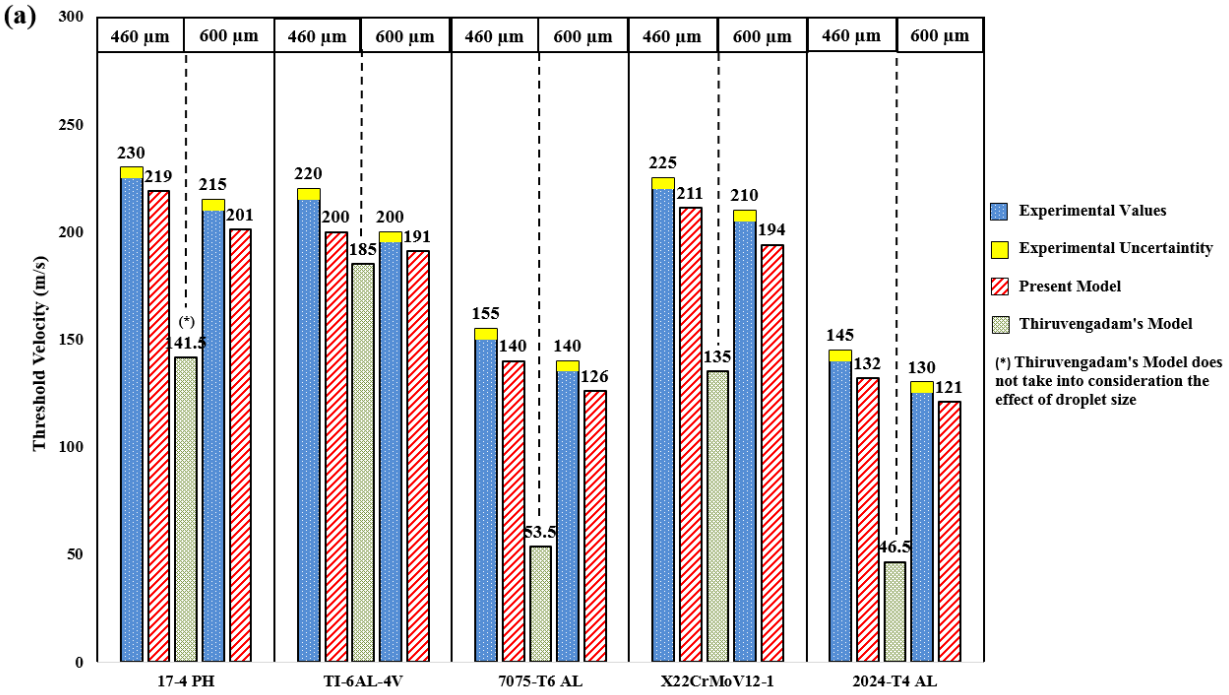

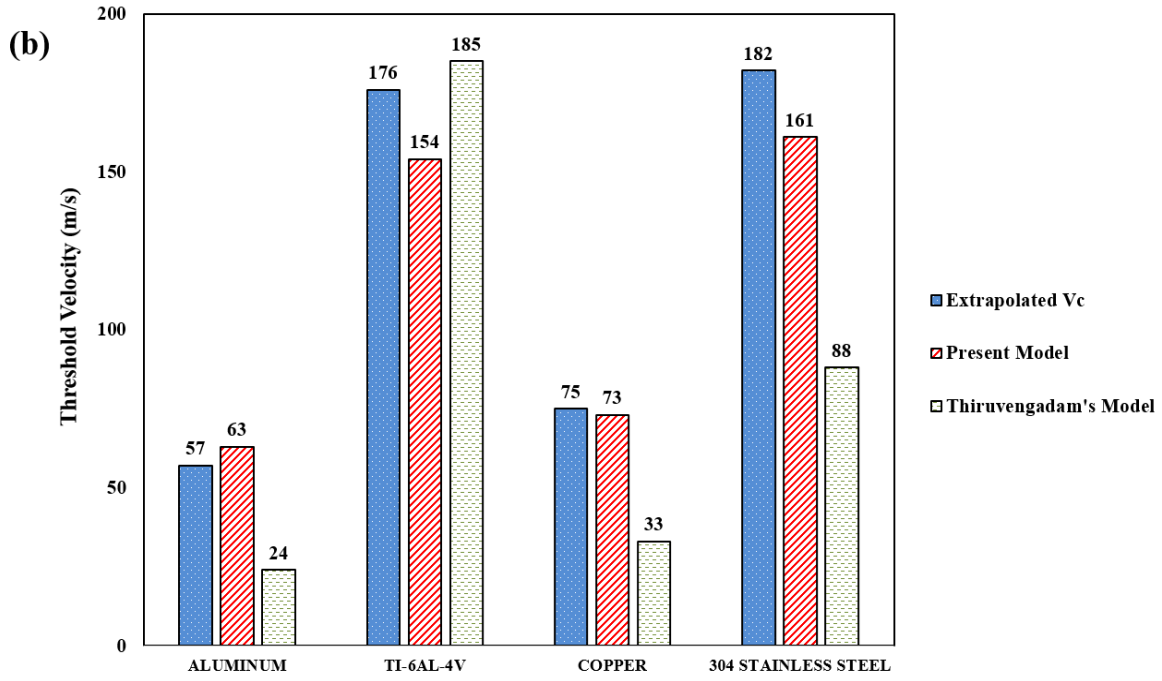

Figure 4-5 Comparison between experimental, present model, and Thiruvengadam's model: (a) materials tested in the present work, and (b) experimental data extrapolated from the literature [110–112].

Table 4-3 Threshold velocity values extrapolated from the literature.

Material	Extrapolated Vc (m/s)	Droplet size (m)	Predicted Threshold Velocity (m/s)		Reference
			Present Model	Thiruvengadam's model	
Aluminum	57	0.0012	63	24	Behrendt [110]
Ti-6Al-4V	176	0.0012	154	185	
Copper	75	0.0012	73	33	King [111]
304 Stainless Steel	182	0.0012	161	88	Ripken [112]

4.4 Significance and Limitations

The importance of the developed mode lies in its ability to predict threshold velocity of metallic materials directly from their basic mechanical properties and the parameters of erosion environment. As such, the present work reintroduces the concept of the threshold velocity and its prediction as important tools for the design and selection of water droplet erosion resistant materials. The concept can also be employed to rank materials according to their erosion endurance. ..

The model, however, does not take into consideration erosion environments characterized by polydisperse, non-uniform distribution of the size of impacting droplets. These conditions best describe the real in-service situations for most of engineering components subjected to water droplet impingement erosion. Extension of the model in these directions can be a subject of future work.

4.5 Summary

The following points summarize the work done on the threshold velocity:

- A model to predict the threshold velocity was successfully developed in this thesis. The formulation of the model is based on the dynamic threshold of crack propagation and dynamic fracture and wear of materials.
- A criterion and experimental procedure to evaluate the threshold velocity is established in this work based on service lifetime of turbine blades.
- The developed model was used to predict the threshold velocities of the five materials studied in this work. The theoretical threshold velocities match the experimental values to very high accuracy.

- The developed model was compared to Thiruvengadam's model. The current model is found to be more accurate than that of Thiruvengadam.

5 INCUBATION PERIOD INVESTIGATIONS

This chapter presents and discusses the investigations carried out in this work on the incubation period in water droplet erosion of metals. As outlined in the thesis objectives, the aim of these investigations was to identify and understand some of the parameters controlling the damage accumulation process during the incubation period, namely; roughening and strain hardening behavior. As such, the first part of the chapter addresses the role of change in surface topography (roughening process) on the stresses during the incubation period of Ti-6Al-4V. The second part addresses the role of mechanical properties and strain hardening exponent on the incubation period, through studying the erosion performance of 17-4 PH steel in three different conditions (as-received and two heat treated conditions).

5.1 Part-I: Roughening During the Incubation Period of Ti-6Al-4V

5.1.1 Background

As discussed in the introduction of this thesis, the incubation period represents the duration where the droplet impacts do not cause any detectable damage on the impacted surface. The incubation period ends when fracture of surface fragments (i.e., appearance of erosion pits) is observed and mass loss begins.

During the incubation period, the surface experiences plastic deformation due to droplet impingements. The plastic deformation results in continuous changes in two important-measurable surface properties; hardness and surface topography, (i.e., impact hardening and impact roughening). The focus of this part of the chapter is on roughening. Previous work such as Kirols' [78] investigated the role of starting/initial surface roughness on the length of the incubation period. However, the way in which roughness evolves with the continuation of

exposure to droplet impact (i.e., roughening profile) has not been studied before. Roughening profile of material may influence the length of the incubation period, because the change in surface topography influences the impact stress due to geometrical stress concentration. Moreover, different materials would have different roughening profiles, which leads to different magnitudes of stress concentrations.

The evolution of impact stresses with roughening profile during the incubation period is studied. First, an experimental erosion test was conducted on Ti-6Al-4V samples at an impact velocity of 250 m/s and average droplet size of 600 μm using the erosion rig and test procedure described in Chapter 3. The test was performed until the end of the incubation period (appearance of visible erosion pits). The 250 m/s impact velocity was chosen because it results in a relatively longer incubation period (>15min). This enabled several interruptions (intervals) during the test, which helped in capturing the different microscopic events taking place during the incubation period. At each time the test is interrupted, hardness and surface roughness were measured before the test is resumed. As such, the roughening and hardening profiles over the span of the incubation period could be carefully evaluated. Moreover, Scanning Electron Microscopy (SEM) was conducted on the impact area at several intervals during the incubation period. Based on the SEM images, finite elements analysis were carried out (details in Appendix-B) to obtain the impact stresses on different surface profiles. The results are presented and discussed in the following sections.

5.1.2 Erosion Test Result of Ti-6Al-4V

The microstructure of the received Ti–6Al–4V is shown in Figure 5-1. The microstructure consists of equiaxed α grains representing the matrix of the alloy along with uniformly distributed β phase.

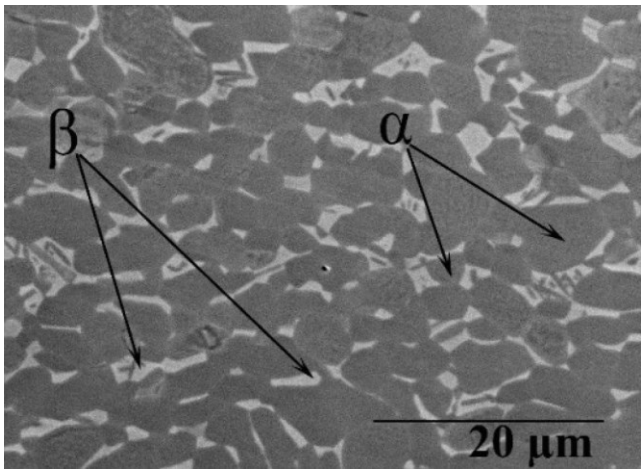

Figure 5-1 Microstructure of the as-received Ti-6Al-4V samples.

Figure 5-2 (a) shows the erosion curve of the tested Ti-6Al-4V alloy in which the cumulative material loss (in grams) is plotted against cumulative exposure duration (in minutes). Macrographs of the Ti-6Al-4V samples at different intervals during the erosion test are also shown in Figure 5-2 (b). The macrographs show the erosion line that represents the impacted area on which roughening is to be studied. As such, the evolution of the impacted area until the end of the incubation period can be traced in these macrographs. End of the incubation period in this work is considered as the time (or number of impacts) at which uniform erosion pitting appears on the impacted area. This also corresponds to a mass loss of around 0.1 mg, which has historically been standardized as the criterion to mark the end of the incubation and used in [54,78,82]. According to Figure 5-2, the end of the incubation period takes place between 12 and 16 min of continuous exposure to droplets impacts.

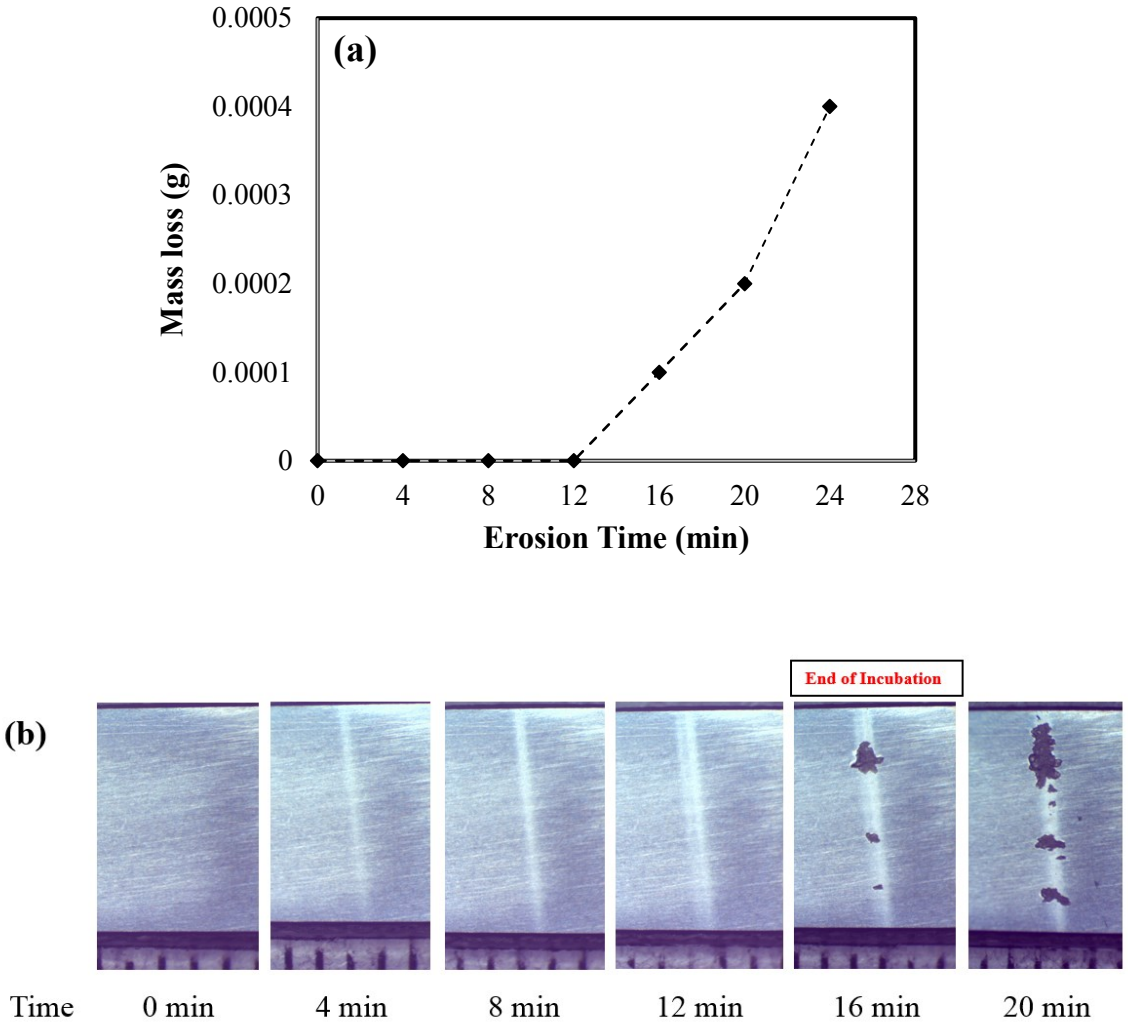

Figure 5-2 Erosion test on Ti-6Al-4V; (a) Erosion curve and (b) Optical images of the impacted area.

5.1.3 Damage Mechanisms During Incubation Period

Figure 5-3 shows SEM micrographs of the impact area at different intervals during the incubation period of Ti-6Al-4V. The interaction between water droplets and Ti-6Al-4V surface leading to WDE damage at the end of the incubation period can be interpreted as follows. Initial droplet impacts (up to 4 min of exposure) seem to have little effects on the topography of the surface of the alloy, where the surface remains relatively smooth and unaffected. During this stage, the surface seems to absorb the transferred energy of the impacting droplet and plastically

deforms. The magnitude of plastic deformation at the early stage of erosion initiation can be deduced from surface hardening in the impact area (as presented in the next section). After 8 min of exposure, however, further droplet impingements result in indentations on the surface, as shown in Figure 5-3 (b). These indentations are often recognized in erosion of ductile metals and commonly referred to as surface depressions [82,113,114]. The appearance of surface depressions seems to be accompanied by networks of localized cracks. These cracks potentially stem from the deformation of the β phase causing its separation from the matrix of the Ti-6Al-4V alloy, as suggested in [66,115]. Also, these depressions represent a significant change in the surface roughness of the alloy, which in turn influences the erosion process [79].

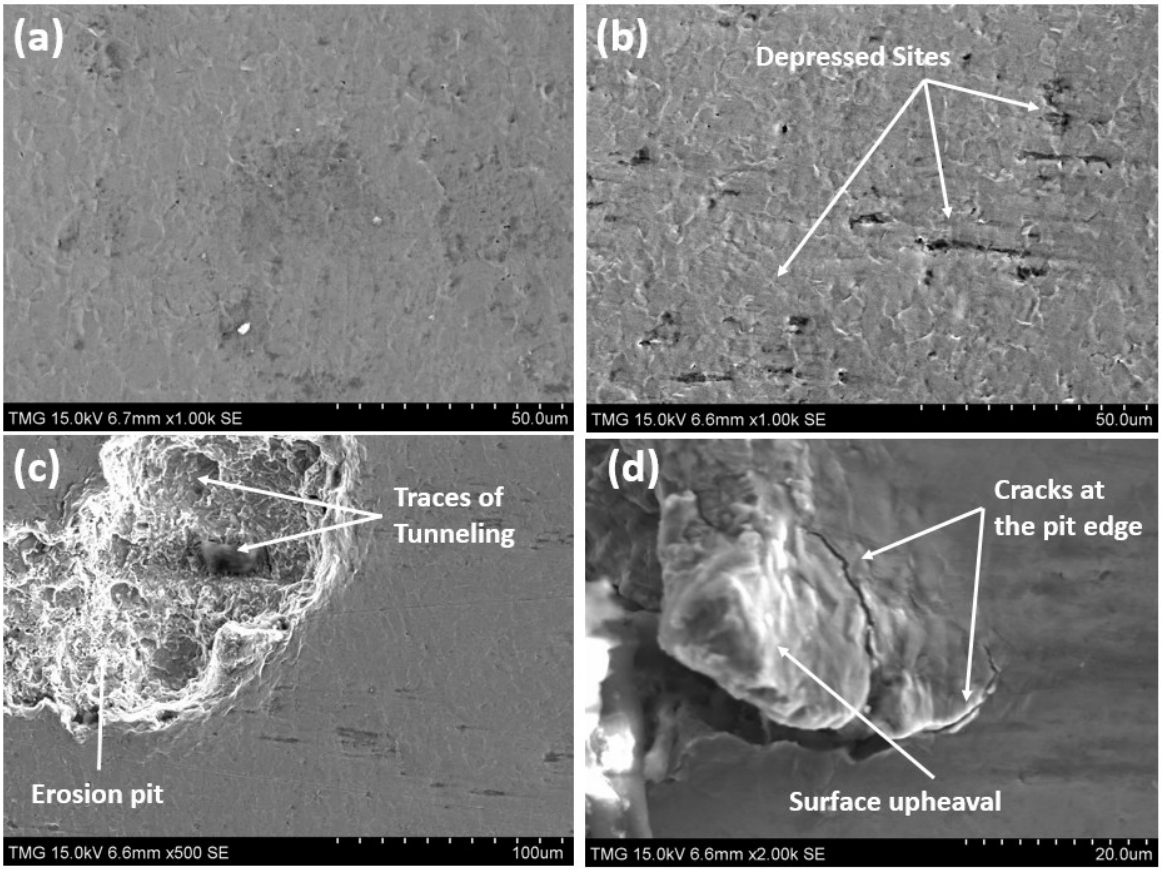

Figure 5-3 SEM micrographs of impacted area at; (a) 8 min, (b) 12 min, (c) and (d) 16 min.

As the end of the incubation period is approached, erosion pits develop on the surface of the alloy, as shown macroscopically in Figure 5-2 (b) and microscopically in Figure 5-3 (c) and (d). Erosion pits may initiate from the coalescence of microvoids in the surface and intense cracking. Moreover, traces of tunneling process can be seen inside the erosion pits. This tunneling process accelerates erosion damage as large chunks of materials are removed from the inside and the periphery of the erosion pits, as shown in Figure 5-3 (c). The tunneling process is enhanced by the brittle fracture of the β phase within the pits along with the increased formation of localized cracking within the grains, as can be supported by the work of Huang *et al.* [115]. As the exposure to droplet impacts continues, these tunnels deepen. The intense impact pressures within the tunnels seem to bend the overlying material at the edge of pits, resulting in the material upheaval shown in Figure 5-3 (d). Surface upheavals are likely to be removed or washed away by lateral jetting from subsequent impacts. Hence, the end of incubation period (initiation of erosion damage) can be seen as the combination of pitting and shearing of surface upheavals and irregularities (formed on the edge of erosion pits) by lateral jetting.

5.1.4 Evolution of Hardness and Roughness During the Incubation Period

As mentioned, the hardness (H_v) and average surface roughness (S_a, area roughness) of the initial polished sample surface were first evaluated. Then, hardness and average surface roughness were measured at 4 intervals during the incubation stage of Ti-6Al-4V. The result is shown in Figure 5-4. It can be seen from Figure 5-4 that hardness increases almost linearly with the exposure to droplet impacts (i.e., linear hardening behavior). The percentage of hardness increase is approximately 15%. Hardening during incubation period stage has traditionally been attributed to the accumulation of plastic strains due to the deformation caused by droplet impact [38].

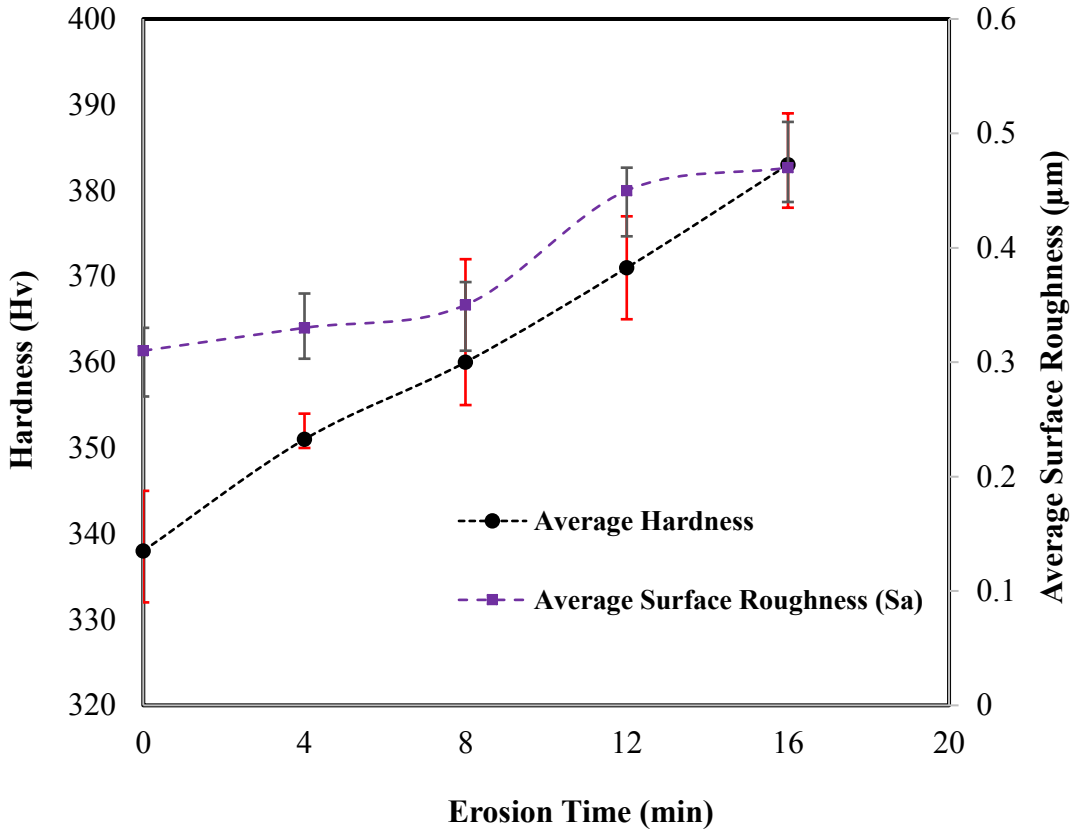

Figure 5-4 Change of hardness and average surface roughness during incubation period of Ti-6Al-4V tested at 250 m/s.

Figure 5-4 also depicts how the average surface roughness S_a changes simultaneously with hardness (i.e., roughening process) over the span of the incubation period. This increase in surface roughness comes from the interactions (i.e., the impact and spreading) of the droplets with the solid surface. It can be attributed also to the plastic deformation, which changes the topography of the impact area. It can be observed from Figure 5-4 that the magnitude of S_a increases only slightly during the first 8 min of exposure to droplet impacts. This is consistent with the microstructural observations in Figure 5-3 and may correspond to the initial stages of the formation of crack networks and surface depressions. Between 8 min and 12 min of exposure,

a noticeable change in the average roughness occurs, possibly due to the increase in the formation of localized surface depressions and their distribution over the impact area. As the exposure to subsequent impacts continues beyond 12 min into the incubation period, the rate of surface roughening decreases slightly. The overall increase in the average surface roughness towards the end of the incubation period is more than 50%.

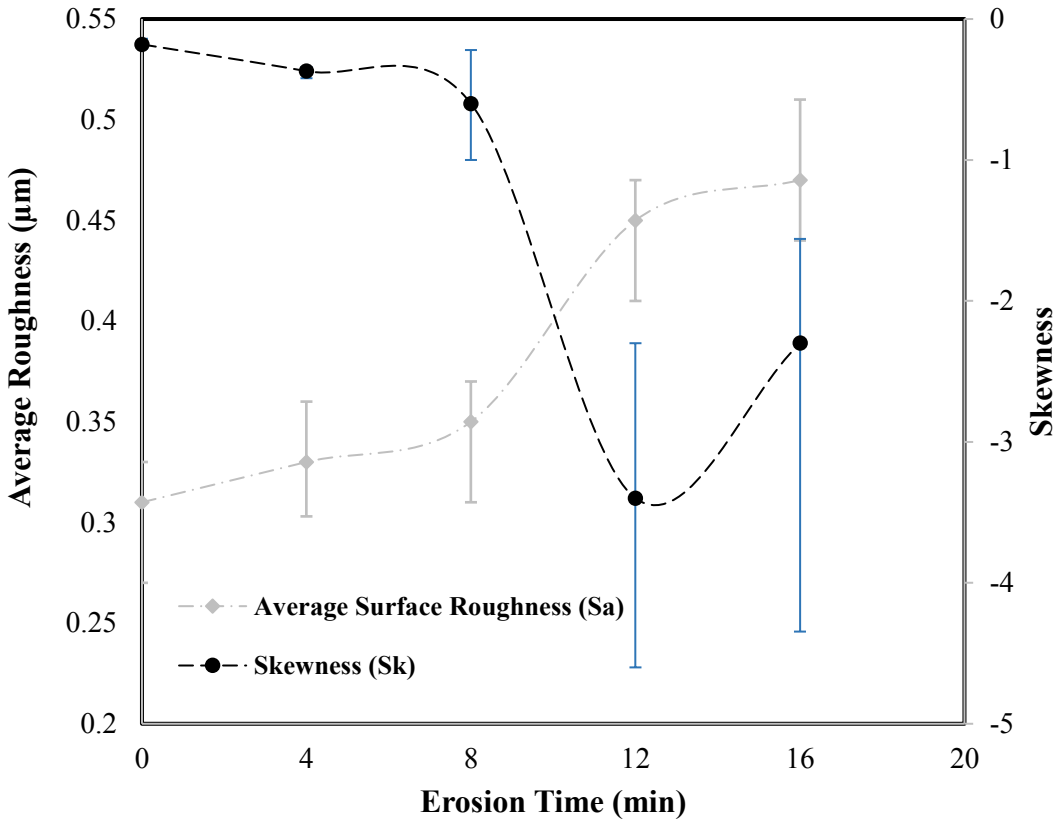

Figure 5-5 Change in skewness and average surface roughness during incubation period of Ti-6Al-4V tested at 250 m/s.

The change in skewness during the incubation period has also been measured to understand the nature of change in surface topography due to droplet impacts. The result is shown in Figure 5-5. Skewness represents the deviation of the roughness profile from symmetry. A

negative value of skewness indicates that the surface is made up mainly of valleys. According to Figure 5-5, skewness maintains a negative value throughout the incubation period, which confirms the domination of valleys in the roughness profile of tested Ti-6Al-4V. The value of the skewness is close to zero during the first 8 min of exposure. After 8 min, the value of skewness decreases drastically, coinciding with the sharp increase in average surface roughness. This suggests that the valleys in roughness profile of the test sample increase in number and depth, which confirms the formation of uniformly distributed surface depressions during the incubation period. This is also supported by the work of Mahdipoor *et al.* [99], where roughness profile including surface depressions is captured in TiAl using atomic force microscope (AFM). Interestingly, an inflection point in skewness is seen after 12 min of exposure, which indicates a sudden shift in the rate of change in valley's formation on roughness profile. This could be an indication of widening of the surface depressions.

The evolution of hardness and surface roughness could not be accurately evaluated after the formation of pitting on the sample's surface. This is because the variation in the hardness, as well as the roughness parameters, is greatly affected by the surface discontinuities presented by the erosion pits, which results in a large discrepancy in the measured values.

5.1.5 Numerical Analysis of Impact Stresses

In this work, numerical analysis was used to understand the influence of surface roughening on the incubation period. In particular, the aim was to investigate the effect of surface depression on impact stresses, and how this may influence the damage accumulation process. The numerical analysis (consisting of impact pressure and finite element analysis) is done in collaboration with Dr. Mason, Marzbali from (from American University in Dubai), and is described in Appendix-B.

The numerical analysis was employed to model several cases. Initially, the coupon was modeled as an ideal solid material, free of defects and with a flat (smooth) surface. This was done to obtain a benchmark for the impact stress to which the magnitude of the stress concentration from any surface irregularities can be compared. Then, in addition to the flat surface, a series of simulations were performed on a surface containing uniform surface features, as shown in Figure 5-6. This was done to simulate the influence of change in surface topology (in particular, the presence of surface depressions) on the magnitude of the impact stresses. In this regard, 9 cases of uniformly distributed surface depressions each having a rectangular shape have been considered. The rectangular shapes are used as an idealization, which facilitates the process of meshing. The dimension of the simulated depressions are listed in Table 5-1. The dimensions have been varied in such way that the influence of width and depth of surface depressions is studied. The size scale of the depression has been approximated from SEM micrographs taken at different intervals during the incubation period

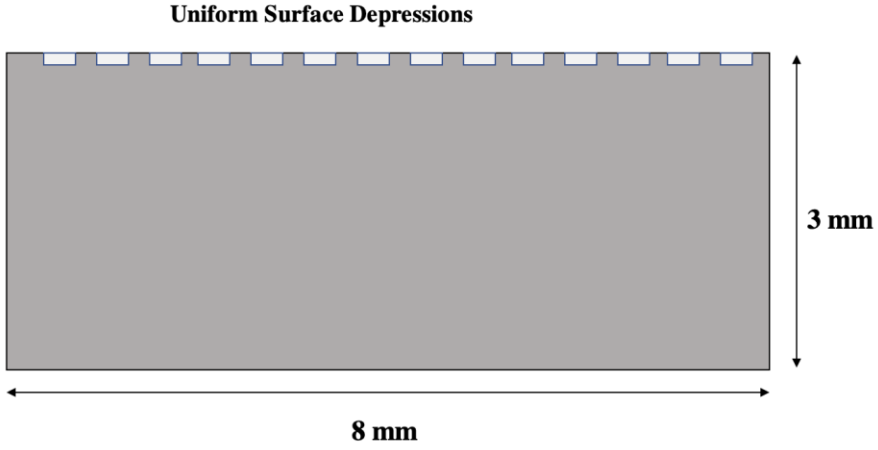

Figure 5-6 Illustration of the surface depression; (a) model of uniform surface depression and (b) SEM micrographs of depression.

Table 5-1 Simulations performed in the finite element analysis.

#	Simulation	Description	Width (μm)	Depth (μm)
	1	Flat (smooth) surface		
	2	Uniform surface depression (1)	10	10
	3		10	20
	4		10	30
	5	Uniform surface depression (2)	20	10
	6		20	20
	7		20	30
	8	Uniform surface depression (3)	30	10
	9		30	20
	10		30	30

For demonstration, the temporal distributions of the maximum Von-Mises stresses in the substrate during the impact on a flat surface is shown in Figure 5-7. It can be observed that the peak of the maximum stress occurs at the beginning of the impact process ($\sim 2.5\times 10^{-8}$ sec), which is the time corresponding to the peak impact pressure [see Appendix-B]. The maximum stress in the substrate decreases rapidly after the peak value, which also follows the distribution of the impact pressure. This temporal distribution of the maximum stress is almost the same for the all the 10 simulated cases except that the magnitude of the peak stress is different for each simulation case.

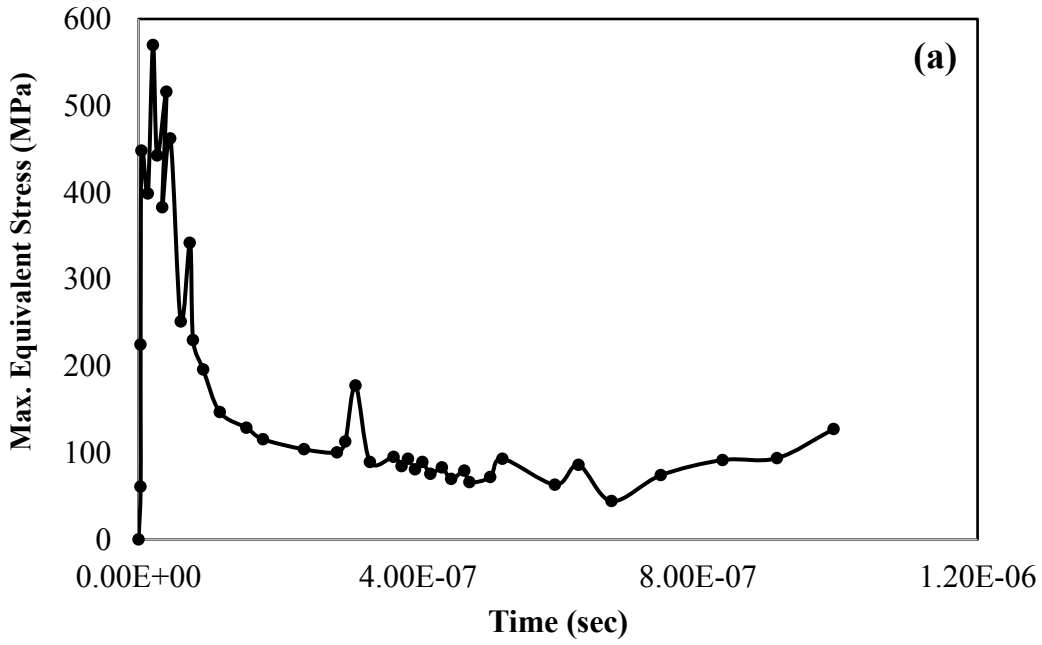

Figure 5-7 Temporal distribution of the maximum equivalent (Von-Mises) stress for a compressible impact of four 600 μm spherical water droplets impinging at a velocity of 250 m/s on a flat surface.

Due to its importance in damage initiation, the peak value of the maximum stress of the simulated cases - described in Table 5-1 - are shown in Figure 5-8. For comparison, the peak of the maximum stress resulting from the impact on flat surface (which is about 570 MPa) is shown as the red horizontal line. The bars represent the peak stress values of the droplet impact on samples with uniform surface depressions of varying depth for fixed width of 10, 20 and 30 μm. It can be observed from Figure 5-8 that the value of the peak stress is markedly higher in all the cases of surface containing depressions compared to the smooth one. For instance, the lowest peak stress value for surface containing depressions having width of 10 μm, 20 μm and 30 μm is about 1208 MPa, 1070 MPa and 984 MPa respectively, all of them occurring when the depression depth is 10 μm. This is approximately about 112%, 88% and 73% higher than the peak stress value in the smooth surface.

The influence of the depression width and depth on the resulting value of peak stress can also be inferred from Figure 5-8. It can be seen from Figure 5-8 that, for the same width, the peak stress value is proportional to the depth of the surface depression. On the other hand, the peak stress value decreases with the width of the depression (expect at 30 µm depth, where all peak stress for all widths have very close values, possibly due to plateauing of the stress concentration effect). This is consistent with trends observed with stress concentration factor (K_t) for notches with flat bottoms in semi-infinite body subjected to tension [116].

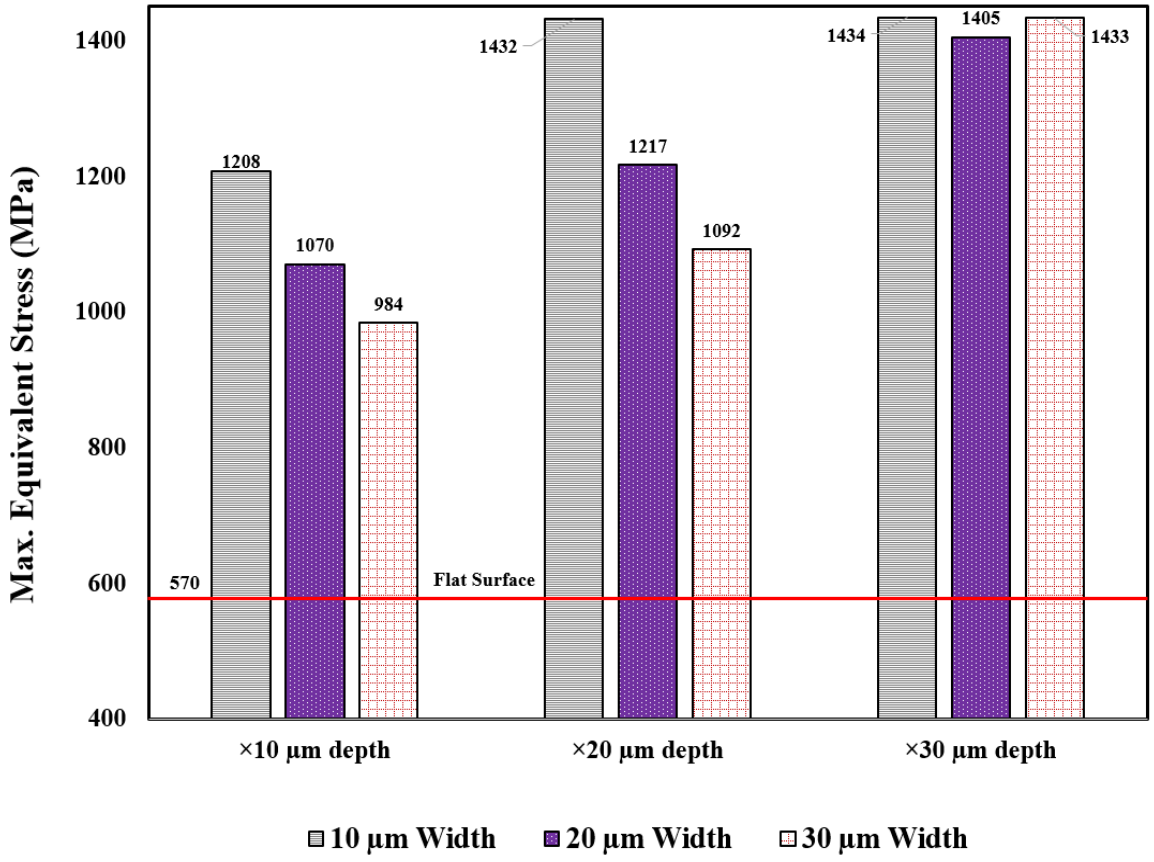

Figure 5-8 Change of peak stress with Surface Condition.

5.1.6 Discussion

5.1.6.1 Change of Stresses Due to Roughening

As presented in Figure 5-4, hardness of the Ti-6Al-4V surface increases by about 15% due to work hardening. The increase in hardness is generally accompanied by an overall increase in erosion resistance of metallic alloys, as demonstrated in the work of Ahmad *et al.* [4]. This entails that every impact cycle is required to cause slightly higher impact stress than the precedent impact cycle, such that the improved resistance can be overcome. That is, the magnitude of the impact stress should be progressively increasing during the incubation period in order to meet the progressive improvement in erosion resistance due to impact hardening. However, as the impact velocity is constant (i.e., at 250 m/s), the incident impact pressure is fixed. Therefore, it is reasonable to assume that a source of stress magnification for the same impact pressure is needed to overcome this hardening-improved-erosion resistance of the surface.

The magnification of impact stress could come directly from the roughening process, taking place simultaneously with the hardening. That is, besides hardening, the plastic deformation of the surface also results in drastic and continuous change in the surface topography. This is evidenced in the present work by the change in roughness parameters illustrated in Figure 5-5 as well as the microscopic observation of the formation of surface depressions (e.g., Figure 5-3 (b)). Moreover, the finite element analysis presented in Figure 5-8 showed that, for the same impact pressure, the peak value of the maximum impact stress for surfaces containing depressions is always higher than that of the smooth surface (i.e, 570 MPa). According to the simulated cases, the increase of impact stress due to the presence of depression can reach up to 2.5 times (i.e., ~1430 MPa) that of the smooth surface. This is mainly due to stress concentration caused by the presence of surface depressions.

It is to be mentioned that the yield and tensile strength of Ti-6Al-4V are around 880 MPa and 950 MPa respectively (see Table 3-2). This indicates that, at an impact velocity of 250 m/s, the impact pressure and the consequent stresses are not likely to cause plastic deformation on a perfectly smooth Ti-6Al-4V (i.e., threshold conditions). This is because, according to the finite element results, the maximum peak stress on a perfectly smooth Ti-6Al-4V surface is around 570 MPa, which is well below the static yield strength of the alloy. It follows that initial surface irregularities are also responsible for certain degrees of stress concentration.

Moreover, the finite element results showed that the magnitude of stress concentration changes significantly with the change in the depression size. According to Figure 5-8 , the peak stress is proportional to the depth of the uniform depression. This is important because depressed regions are likely to deepen with further droplet impacts. This is supported by the work of Huang *et al.* [115], who studied the mechanisms of damage initiation in Ti-6Al-4V subjected water droplet impact loading during waterjet erosion using SEM and atomic force microscope (AFM). It was argued [115] that lateral jetting results in preferential damage to grain boundary regions, which leads to the formation of damage features such as surface irregularities and microvoids. Then, hydraulic penetration into these damage features lead their deepening [115]. This can further be evidenced by the change in skewness observed in this work. As mentioned, the lower the value of skewness, the deeper the valleys in the roughness profile. Roughness measurement in this work revealed that the value of skewness decreases with the exposure to droplet impacts, as shown in Figure 5-5. This means that, on average, the depressed regions are likely to deepen continuously with the exposure to droplet impingement. It follows that the magnitude of stress to which the surface is subjected increases with exposure duration due to the formation and deepening of surface depressions. This trend is likely to continue until several cracks and voids

merge together to form large erosion pits and craters. From a failure point of view, the cyclic increase in the magnitude of the peak stress due to surface roughening overcomes the cyclic increase in erosion resistance due to work hardening.

5.1.6.2 Periodic Polishing to Prevent Roughness Buildup

To test this hypothesis, an additional sample of Ti-6Al-4V was tested at the same test conditions (i.e., impact velocity of 250 m/s) against a reference sample shown in Figure 5-2 (b). Both samples were polished with 1200 grit paper before the start of the erosion test. Then, the erosion test was interrupted every 4 min and one of the samples was re-polished with 1200 grit to remove the accumulated roughening, in an attempt to restore the initial surface conditions. The other sample was kept as a reference sample without re-polishing. The mass lost during every re-polishing process was less than 0.0004 g. Given the density of the Ti-6Al-4V being around 4.43 g/cm^3, this results in a volume loss of around 0.09 mm^3 and a maximum thickness loss of 3μm over the entire surface of the sample (i.e. 8mm×3mm). In most of the cases of impact treated samples, the depth of the hardened layer is greater than 10 μm, as was shown by Child *et al.* [117] for shot peening and Gujba *et al.* [18] for ultrasonic nanocrystalline modification treatment. Hence, it can be said that the polishing is done in such a way that only the roughness is removed without removing the entire hardened layer.

Figure 5-9 shows the impact area in the reference un-polished sample, the test sample before polishing, and the test sample after polishing. It can be seen from Figure 5-9 that continuous polishing of the sample resulted in delaying the formation of erosion pits and in a longer incubation period. This confirms that removing the rough layer from the impact area influences the stress accumulation process by eliminating the stress concentration due to the

surface irregularities. To the best of our knowledge, this is the first time where such an experiment has been carried out.

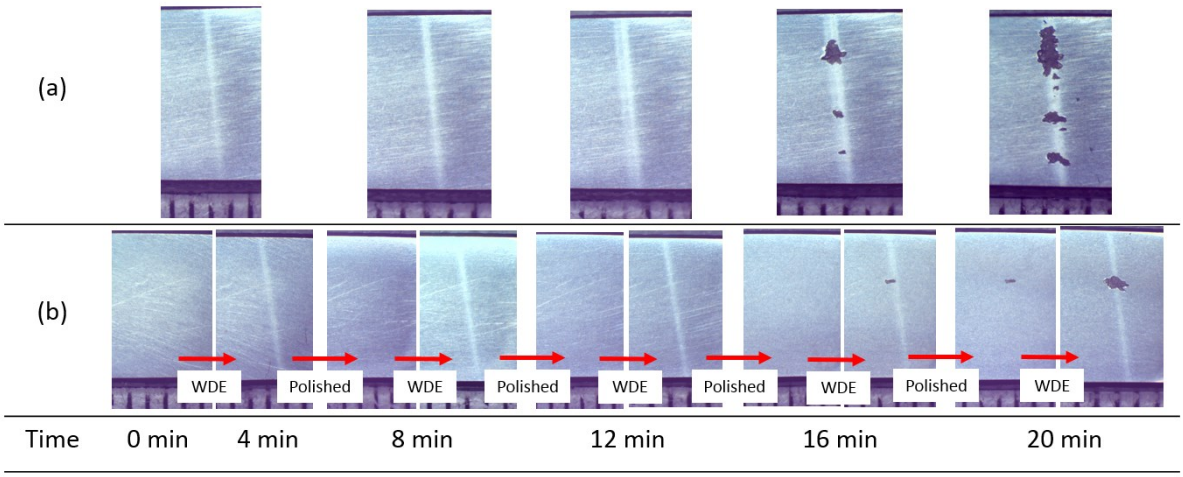

Figure 5-9 Images of the impact area on the (a) reference sample, (b) sample that is continuously polished after each test.

It is noteworthy that regularly restoring the initial surface condition alone did not completely prevent the eventual erosion of the sample as a pit eventually formed after 16 min. This is interesting because it indicates that, with slight help from the initial roughness, the direct impact pressure on the surface and the stress waves resulting from it may singlehandedly cause detectable material damage. It is possible that the stress waves may cause internal stresses beneath the surface that could result in potential subsurface cracks. These cracks then accumulate into networks and lead to formation of surface fragments, as shown in Figure 5-9 (b). The continuous polishing seems to eliminate or reduce the contribution of lateral jetting and stress concentration that would otherwise enhance and accelerate the damaging process.

Although the present analysis of the impact stresses is qualitative in nature, it sheds light on the role of roughening on the damage accumulation process during the incubation period.

Roughening is an important factor that has never been considered in the modeling and prediction of the incubation period [45,55,56]. That is, previous studies focused only on the initial roughness and hardness values without giving much attention to the way in which these parameters evolve with exposure to impingements. For instance, the work of Ruml *et al.* [46] represents the only model that considered the initial surface roughness (Ra) in the prediction of the incubation period. They [46] did not, however, discuss the evolution of roughness and its role in the damage process.

It should be mentioned that the value of the peak stress and its evolution with surface depression depend on the size of the impacting droplets [79]. Moreover, the evolution of surface depression - caused by droplet impacts - can be viewed as a function of the mechanical properties of the surface. This is because depressed regions result from plastic deformation, which is governed by the mechanical properties and the way in which they change with exposure to impingements (i.e., hardening). As such, it can be concluded that hardening and surface roughening are crucial parameters that both need to be considered in predicting the duration of the incubation period.

5.1.7 Summary

In this first part of the chapter, the effect of surface roughening on damage accumulation during the incubation period of Ti-6Al-4V is studied. The main findings are as follows:

- Initial droplet impingement causes plastic deformation on the surface of the impacted metal. The plastic deformation results in a steady increase in surface hardness that reach up to 15% by the end of the incubation period.
- Droplet impingements are also found to cause more than 50% increase in surface roughness and result in formation of surface depressions. Measurement of skewness indicated that

these depressions gradually deepen with continuous exposure to droplet impingements, potentially through hydraulic penetration.

- Finite element simulations of surface containing depressions of different size showed that the peak stress value is markedly higher in rough surfaces compared to flat/smooth one. The peak stress also increases significantly with the depth of the depression.
- Hardening results in a dynamic improvement in erosion resistance of the surface. This improvement in erosion resistance is overcome by the concentration of impact stresses due to roughening process.
- Elimination of the roughening factor through periodic polishing of the surface was found to increase the length of the incubation period by eliminating the stress concentration.

5.2 Part-II: The Role of Strain Hardening Exponents In the Incubation Period

5.2.1 Background

From the previous experiments on Ti-6Al-4V, it has been shown that hardness increases significantly during the incubation period (i.e., impact hardening) due to the plastic deformation caused by droplet impingements. The change of hardness over the span of the incubation period depends on the initial hardness value as well as on the strain hardening behavior of the material. As such, different strain hardening behaviors are likely to result in different impact hardening profiles, which in turn leads to different surface responses to droplet impacts. In this part of studying the incubation period, the role of strain hardening behavior (represented by strain hardening exponent (n)) of the material on the damage accumulation process is investigated. ..

For this purpose, 17-4 PH stainless steel is selected. Three conditions of the 17-4 PH are considered in this part of the work, namely; the as-received or condition-A, H-925, and H-1025.

The details about the heat treatment are discussed in section 3.1.1. Several characterizations were performed on the samples of the three conditions of the 17-4 PH before the erosion test. Firstly, Scanning electron microscopy (SEM) and Confocal Laser Scanning Microscopy (CLSM) were carried out on the surface of the samples to ensure that the three conditions have nearly similar grain size and surface roughness. Then, tensile test and Vickers Hardness test were also carried out to evaluate the mechanical properties, including the strain hardening exponent (n). Finally, water droplet erosion tests were carried out on the three conditions of the 17-4 PH using 460 μm average droplet size and two impact velocities (250 m/s and 300 m/s). The results are detailed in the ensuing discussion.

5.2.2 Microstructure and Mechanical Properties

Figure 5-10 shows the SEM micrographs of 17-4 PH stainless steel, where equiaxed martensitic grains of about 30-50 μm are observed in each three conditions. It can be concluded from Figure 5-10 that no significant changes in grain size were observed due to aging treatments. This is also in accordance with previous studies [84,85]. Moreover, the average surface roughness of all samples, measured by CLSM, is found to be 0.012 μm with a standard deviation of 0.002 μm. This also demonstrates the consistency of the surface preparation process. Similar surface roughness among the samples is desired in this work, as different surface roughness may change the erosion incubation time for the same impact conditions [78].

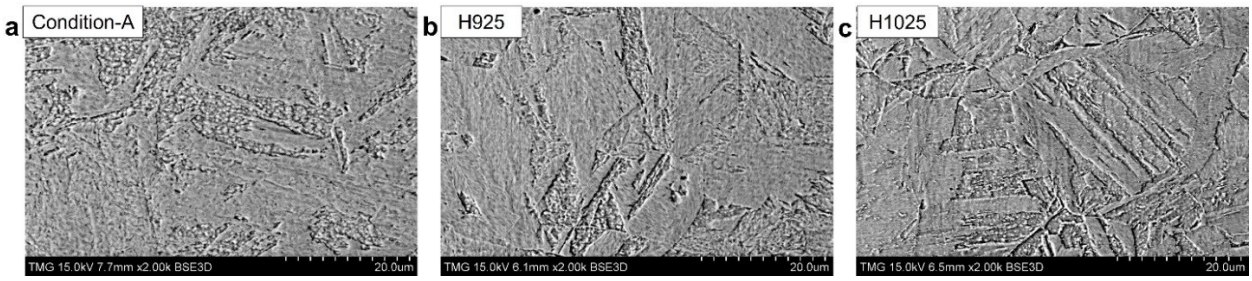

Figure 5-10 SEM micrographs of the test conditions (a) Condition-A, (b) H925 and (c) H1025. Ref [118].

The hardness values along with the mechanical properties obtained from the tensile test for the three conditions of 17-4 PH are listed in Table 5-2. It can be seen from this table that Condition-A is the softest among the three with hardness value of 321 HV. The aged conditions of H925 and H1025 have relatively high and moderate hardness values of 401 and 347 HV, respectively, which are close to the ones reported in the literature [84–86]. It is to be noted that the peak hardness of 17-4 PH can be achieved at aging temperature of about 480ºC [85]. As such, condition H925 -being close to the optimum aging treatment- has the greatest hardness. The lower hardness of H1025 compared to H925 could indicate overaging, which is known to reduce the mechanical properties of 17-4 PH [84,85].

Table 5-2 Measured tensile properties and hardness of the 17-4 PH conditions.

Sample condition	**Young's modulus (GPa)**	**0.2% offset Yield strength (MPa)**	**Tensile strength (MPa)**	**Strain hardening exponent 'n'**	**Elastic resilience (MJ/m^3)**	**Hardness (Hv)**
Condition-A	187	830	1056	0.15	3.35	321
H925	195	1257	1324	0.06	6.68	401
H1025	196	1133	1153	0.02	5.65	347

Table 5-2 also shows the tensile properties for the solution treated condition-A, and H925 and H1025 aged conditions obtained from their engineering stress-strain curves. The modulus of

elasticity (E) for both H925 and H1025 aged conditions is about 195 GPa, whereas Condition-A has a slightly lower value at 187 GPa. This is consistent with Rack *et al.* [119] results. Moreover, Condition-A has the lowest yield and tensile strengths, whereas H925 has the highest. H1025 has a relatively intermediate yield and tensile strength. Elastic resilience and strain hardening exponent (n) have also been evaluated for the three conditions of the 17-4 PH steel. The Elastic resilience (which depends on the yield strength and the elastic modulus of the material) is found to be 3.35, 6.68 and 5.65 MJ/m^3 for Condition-A, H925 and H1025, respectively. The strain hardening exponent (n) of Condition-A is the highest among the three conditions at about 0.15 and that of H1025 is the lowest at about 0.02. H925 condition has an intermediate n-value of about 0.06.

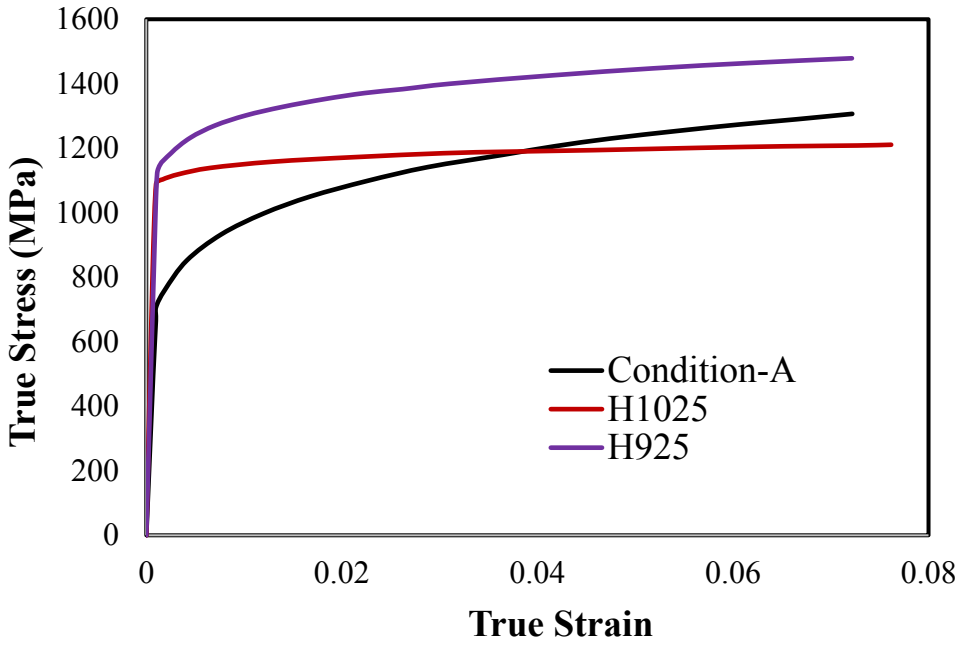

Figure 5-11 Ideal true stress versus true strain curves of the 17-4 PH stainless steel in each condition.

True stress-strain curves are plotted for the three conditions of 17-4 PH using the Hollomon's equation and shown in Figure 5-11. These curves will be used to interpret the results of the erosion performance. Relevant to analyzing erosion results, is the fracture strength of the materials (last point in each curve). It can be observed from Figure 5-11 that the fracture strength of Condition-A is higher than that of H1025, even though Condition-A has lower yield strength value. This is due the high strain hardening exponent value of Condition-A. Condition H925 has the highest fracture strength.

5.2.3 Erosion Test Results

For comparing the erosion performance of the three condition, Condition-A is used as a reference in the erosion tests. The erosion curves of H925 versus Condition-A and H1025 versus Condition-A at impact speed of 250 m/s are shown in Figure 5-12 and Figure 5-13. Condition-A has an incubation period of only about 50 min, whereas H925 and H1025 resulted in an incubation time of 160 and 75 min. A significant difference in the incubation times of H925 and Condition-A (3.2 times) is clearly visible, while the incubation period of H1025 condition is only 1.5 times that of Condition-A. The macrographs in Figure 5-14 show the test surface of each sample, which appear to be consistent with the observations from the erosion curves.

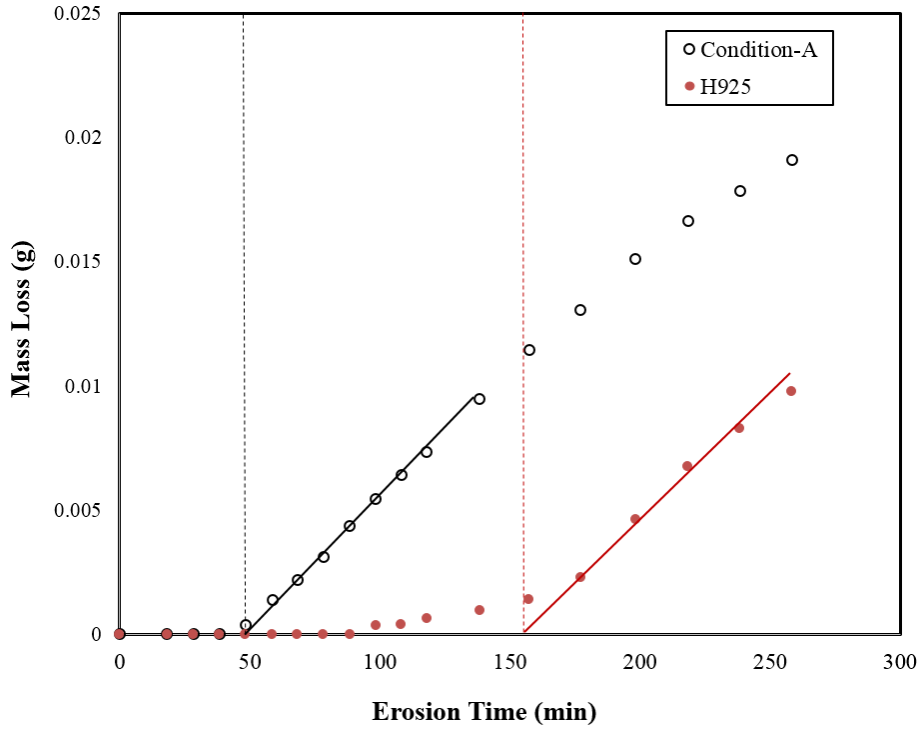

Figure 5-12 Erosion curves of Condition-A versus H925 at impact speed of 250 m/s.

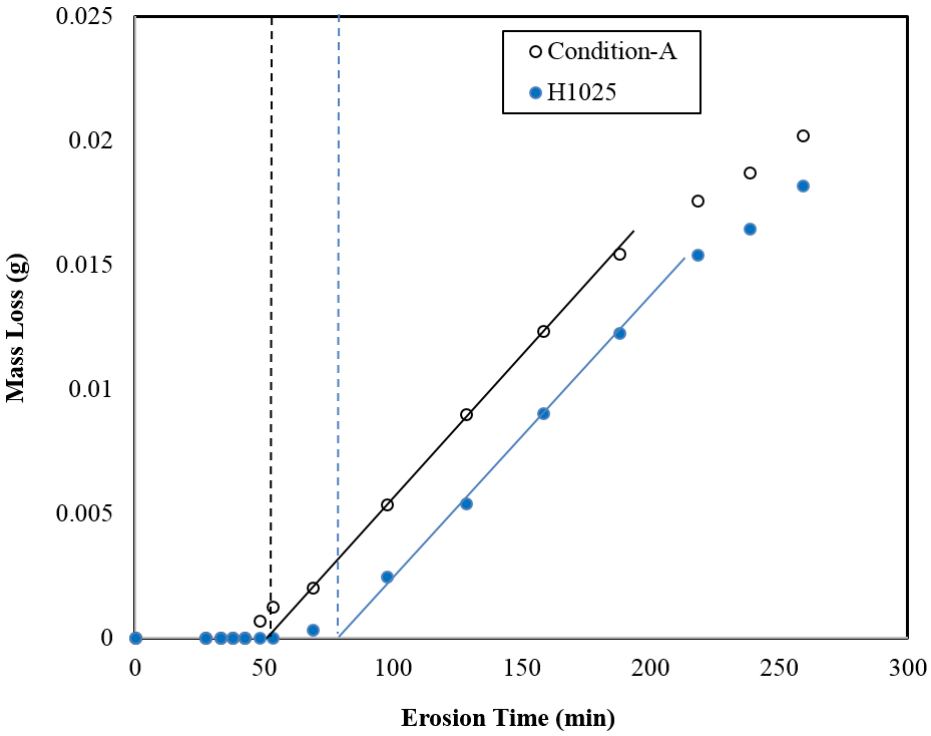

Figure 5-13 Erosion curves of Condition-A versus H1025 at impact speed of 250 m/s.

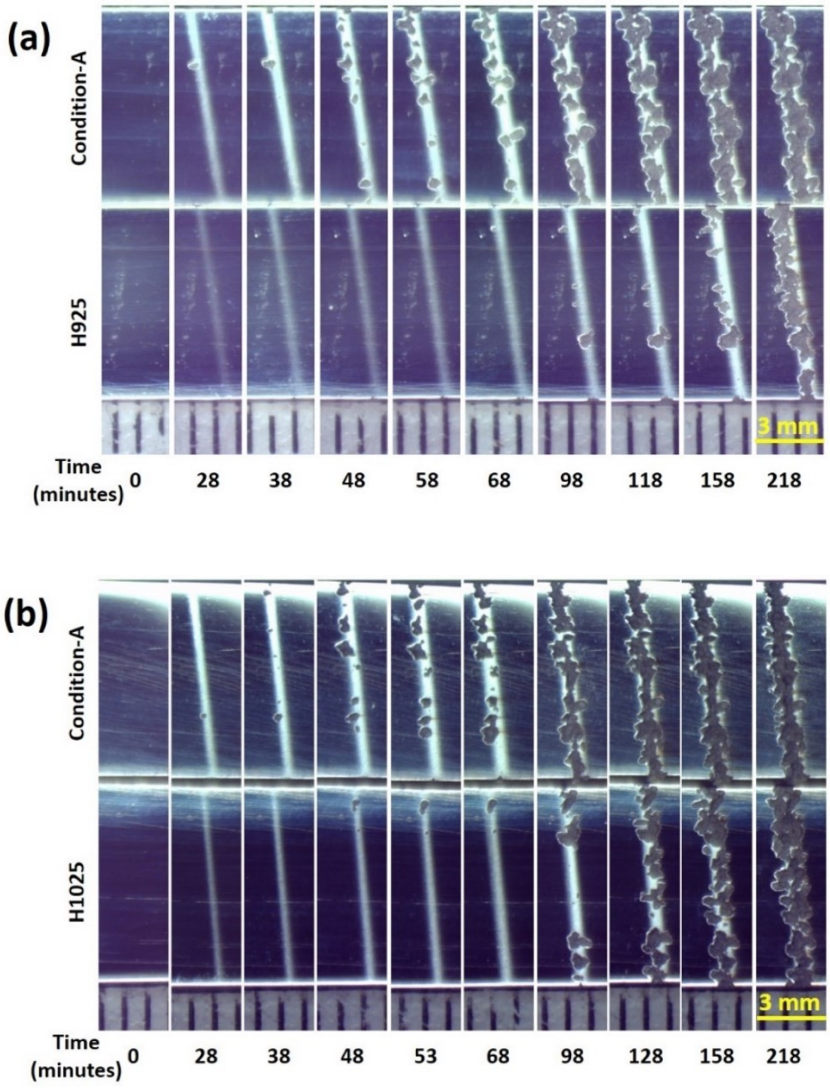

Figure 5-14 Macrographs of erosion samples in (a) Condition-A vs H925 and (b) Condition-A vs H1025 tested at impact speed of 250 m/s [118].

The erosion curves of Condition-A versus H925 and H1025 at impact speed of 300 m/s are shown in Figure 5-15 and Figure 5-16. At 300 m/s, the incubation time is almost the same for Condition-A and H1025 at about 15 min, whereas H925 has a greater incubation time of about 21 min. The observed results are in accordance with the appearance and evolution of craters seen in the macrographs of Condition-A versus H925 (Figure 5-17 (a)) and Condition-A versus H1025 (Figure 5-17 (b)).

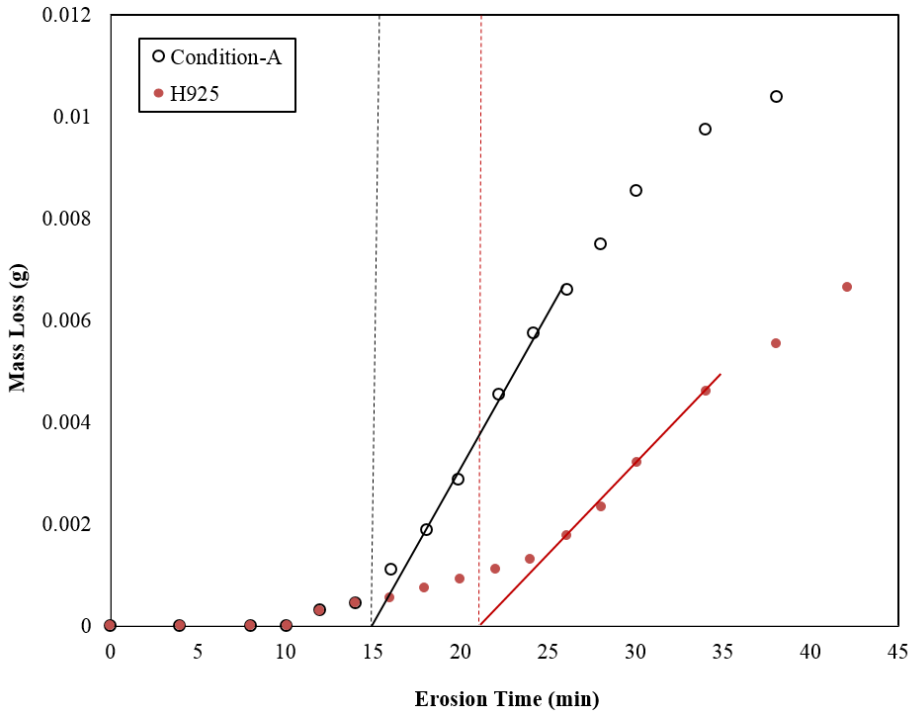

Figure 5-15 Erosion curves of Condition-A versus H925 at impact speed of 300 m/s.

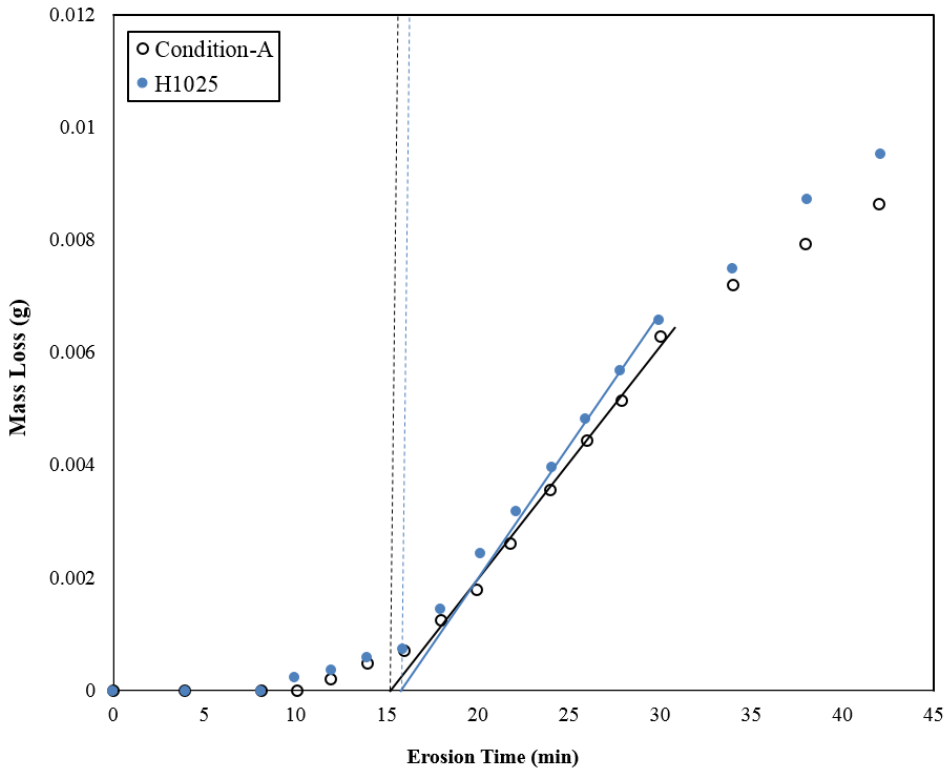

Figure 5-16 Erosion curves of Condition-A versus H1025 at impact speed of 300 m/s.

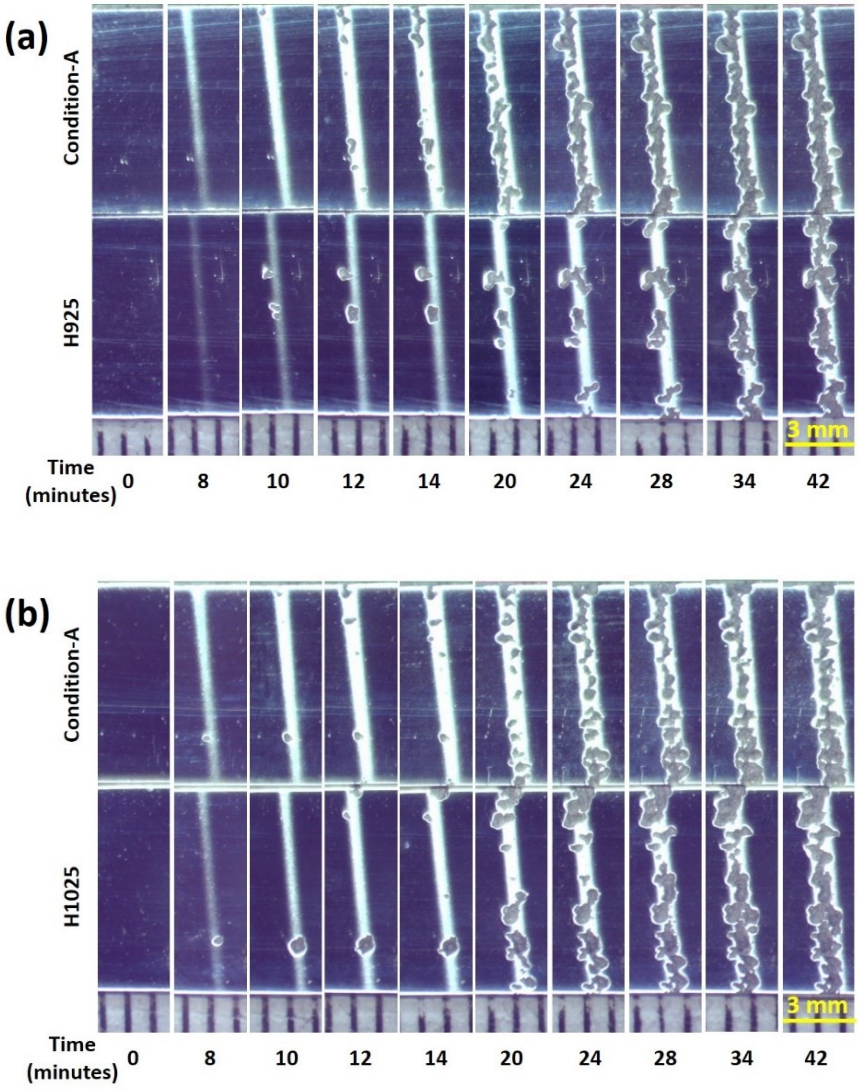

Figure 5-17 Macrographs of erosion samples in (a) Condition-A vs H925 and (b) Condition-A vs H1025 tested at impact speed of 300 m/s [118].

The incubation time and the maximum erosion rate for each condition are summarized in Table 5-3. The influence of impact speed on the incubation period can be observed clearly from this table. The acceleration of erosion with increase in impact speed is due to increase in the number of impacts, impact pressures, lateral jetting speeds and the kinetic energy, which are all proportional to impact speed [48,54].

Table 5-3 Summary of incubation time and maximum erosion rate at 250 and 300 m/s.

Test speed	Condition	Incubation time (minutes)
250m/s	Condition-A	50
	H925	160
	H1025	75
300m/s	Condition-A	15
	H925	21
	H1025	15.5

5.2.4 Discussion

The effect of strain hardening exponent (n) on the erosion behavior of the three 17-4 PH conditions are discussed in this section. Prior to that, mechanics of damage accumulation during the incubation period is explained in terms of the true stress-strain curves.

5.2.4.1 Hypothesis of Damage Accumulation

Figure 5-18 shows the true stress-strain curves of the three tested conditions of the 17-4 PH, where the yield and fracture points are highlighted. Points A_1, B_1 and C_1 are the initial yield points, whereas F, O, and V are the fracture points of Condition-A, H1025 and H925 respectively. Two important assumptions are made in the present work regarding the impact strain and the accumulation of damage during the incubation period. The first assumption is that, for plastic strain to buildup in the material (and eventually causes fracture), the portion of droplet impact energy transferred to the material must exceed the elastic resilience of the material at every impact cycle. In other words, if the transferred impact energy is less than the elastic resilience, erosion is avoided and the threshold condition (discussed in chapter 4) prevails. The second assumption is that when the accumulated plastic strain due to cyclic impact exceeds the fracture

strain of the material, surface fragments begin to fracture. This can be considered as the end of the incubation period. Underlining this assumption is the idea that the yield point continuously shifts towards the fracture point by certain magnitude at every impact due to work hardening. As such, the cyclic time (i.e., cumulative impact energy) needed to reach the fracture point is equivalent to the incubation time. The two assumptions (and hence the current damage hypothesis) are limited to the end of the incubation period. This is because, as the erosion starts, other factors come into play such as erosion pit and crater shape and dimensions [38].

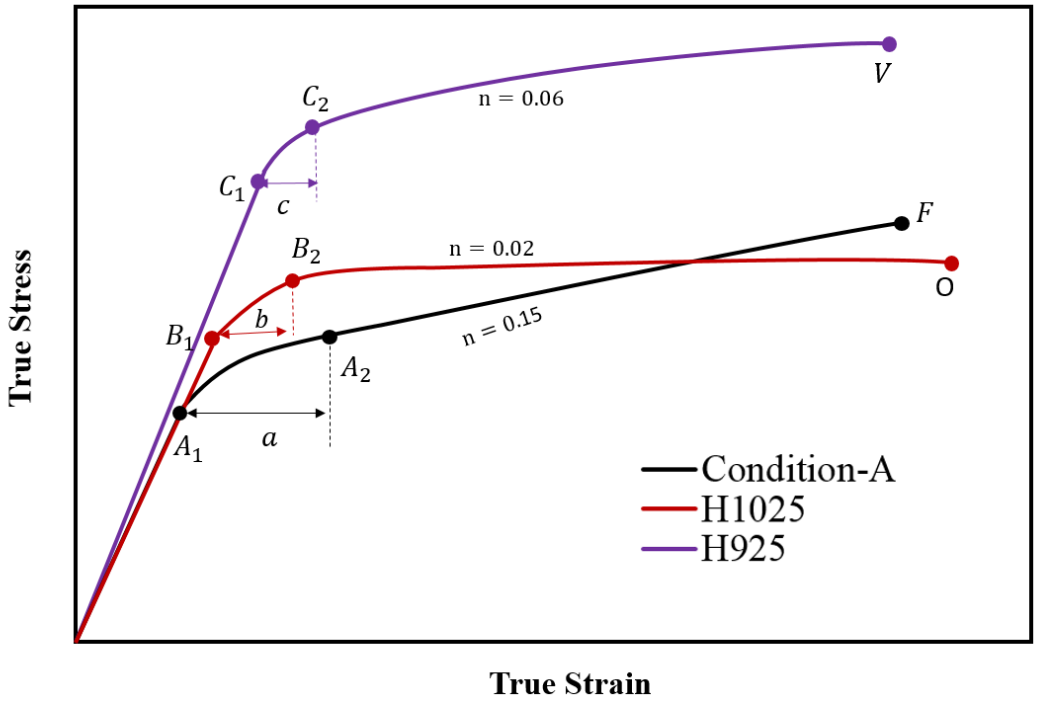

Figure 5-18 Schematic explaining the progression of yield point due to strain hardening in each condition of the 17-4 PH stainless steel.

Admittedly, the proposed hypothesis for the incubation period does not take into consideration other phenomena such as crack initiation and propagation and how they lead to material's removal. It also relies on bulk-static properties rather than localized-dynamic properties, whereas dynamic properties are more representative to the mechanics of water droplet

impact. However, in the absence of a comprehensive theory of damage accumulation, this idealization is reasonable in so far as the role of the mechanical properties are to be discussed. In the light of this hypothesis, the role of strain hardening exponent (n) on the erosion process during the incubation period are explored in the ensuing discussion.

5.2.4.2 The Role of Strain Hardening

Based on the preceding discussion, the strain hardening exponent (n) can influence the incubation period in two ways. Firstly, reaching the fracture point in the true stress-strain curve (which is idealized to represent the end of the incubation period) depends on the initial yield point and strain hardening exponent (n) of the material. That is, having high strain hardening exponent results in high fracture strength and hence, longer incubation period. This is evidenced by the observed similarities between the incubation periods of Condition-A and H1025. Although the H1025 condition has significantly larger yield strength compared to Condition-A, they both have very similar fracture strength due to the high strain hardening exponent of Condition-A. This has resulted in close incubation times between the two conditions when both are tested at 250 m/s and almost identical incubation times when both are tested 300m/s. Therefore, higher strain hardening exponent results in longer incubation period due to the fact that higher impact stresses are needed to bring the material to the fracture point.

Secondly, strain hardening exponent influences the length of the incubation period by controlling the cyclic increase in the hardness and yield strength (and the associated elastic resilience) and hence, the rate of damage accumulation. This is because it has been shown, in the literature (e.g., ref [64]) as well as in the first part of this chapter, that hardness and yield strength of metals increase with exposure to droplet impacts. In other words, every droplet impingement on the surface induces plastic strain in the material, and therefore causes the yield point (i.e. yield

strength and strain) to shift towards the fracture point by certain magnitude. For instance, the yield points in Figure 5-18 could progressively shift respectively from point A_1 to point A_2, from B_1 to B_2, and from C_1 to C_2 in Condition-A, H1025 and H925 after N cycles (which corresponds to a shift in the true strain having the values of a, b, and c for Condition-A, H1025 and H925, respectively). Also, as the yield point moves, the elastic resilience at points A_2, B_2 and C_2 is greater than that at points A_1, B_1 and C_1 respectively in Figure 5-18. As such, the erosion resistance to each N cycle of droplet impacts is greater than that during the preceding cycle by the virtue of increased yield strength and elastic resilience. The strain developed is progressively reduced until failure at a rate governed by the n-value of the condition. In other words, it is the strain hardening exponent that governs the continuous progression of yield point, and therefore, controls the rate of erosion resistance to damage accumulation.

It is to be mentioned that at higher impact velocities (e.g. greater than 300 m/s for the 17-4 PH), it is likely that the peak impact stress is greater than the dynamic tensile strength of the material. This may result in uncontrollable and nonuniform deformation or even cracking of the impacted material, which may obscure the strain hardening effects and makes it irrelevant.

Based on the above analysis, it can be concluded that having greater strain hardening exponent is beneficial to erosion resistance of metals. The greater strain hardening exponent not only results in high fracture strength, but also in higher cyclic yield and elastic resilience, which is conducive to slower rates of impact damage accumulation. This analysis may however not be valid for the conditions where the impact stresses are greater than the dynamic tensile strength of the material. It may also cease to apply for cases of already strained materials (e.g. mechanically treated surfaces). This is because, as proposed in [61,120], this kind of surface treatments introduce a certain amount of cold working in the material that later results in a faster

embrittlement and erosion failure. It is expected in such cases that lower strain hardening exponent is conducive to slower rate of damage accumulation and hence longer incubation period. Investigating of the role strain hardening in erosion performance of pre-strained materials is a subject of an ongoing investigation.

5.2.5 Summary

In this part of the chapter, the role of materials' strain hardening (n) on the initial incubation period of metals is investigated by studying the erosion performance of the 17-4 PH stainless steel in annealed, H925 and H1025 conditions. The samples were tested at impact speeds of 250 and 300 m/s with an average droplet size of 460 μm. It has been found that:

1. At an impact speed of 250 m/s, H1025 has a small difference in incubation time with respect to Condition-A, whereas H925 had a significantly longer incubation time. However, at an impact speed of 300 m/s, Condition-A and H1025 have a similar erosion incubation period while H925 has a slightly improved erosion performance.
2. The different erosion performance of the 17-4 PH steel in the three studied conditions is due mainly to the variation in their mechanical properties as the microstructure is similar for these conditions.
3. The strain hardening exponent (n) dictates the rate at which the fracture point is reached as well as it controls the cyclic increase in hardness and yield strength. Hence, strain hardening exponent (n) plays an important role in the length of the incubation period of the 17-4 PH stainless steel.
4. Erosion resistance of metallic materials is likely to be a synergy of several mechanical properties. Strain hardening exponent (n) is a significant factor in this synergy.

6 CONCLUSIONS AND FUTURE WORK

The present work addressed the topic of predicting the threshold condition and the incubation period in water droplet erosion. For the threshold condition, the objectives were to develop a mathematical model that can predict the threshold velocity from the properties of the solid surface as well as to establish a practical experimental procedure for evaluating it. As for the incubation period, the aim was to investigate the role of surface roughening and strain hardening exponent (n) on the damage accumulation process such that an incubation prediction model consisting of these parameters can be developed in the future. Analysis of the impact mechanics, experimental erosion tests on various metallic alloys, and analysis of erosion data were utilized to achieve these objectives.

The theory of threshold condition for crack propagation was combined with resistance of metallic materials to dynamic wear and fracture to arrive at a mathematical model that predicts the threshold velocity from the properties of the target material. To establish an experimental methodology for the evaluation of the threshold velocity, service lifetime of wind turbine blades when subjected to heavy rain condition was carefully analyzed and utilized.

Five different metallic alloys were carefully selected for the experimental campaign of this work. These are Ti-6Al-4V, 17-4 PH stainless steel, 410 stainless steel, and 7075-T6 and 2024-T4 aluminum alloy. Moreover, 17-4 PH stainless steel was heat treated at two different conditions each resulted in a material having a new set of mechanical properties. These materials – together – they offer a wide range of mechanical properties, which enables the investigation of the role of properties on the damage accumulation process. Erosion tests were then carried out at various impact velocities with two different droplet sizes using erosion testing rig at Concordia

University, with a focus on the incubation period. The change in hardness (i.e. impact hardening) and surface roughness (i.e. impact roughening) were evaluated during the incubation period using Vickers microhardness and Confocal Laser Scanning Microscope (CLSM) tests. Scanning Electron Microscopy (SEM) were performed on the impact area at selected intervals to reveal damage features. A finite element analysis (FEA) was employed to evaluate the value of the impact stress on the flat and rough surfaces, and to examine the influence of the surface irregularities on the impact stresses during the course of the incubation period. The findings, contributions and publications, and suggestions for the future work are summarized in the following sections.

6.1 Conclusions

The main conclusions of this thesis are summarized as follows:

For the Threshold Condition:

1. Modeling erosion endurance by using the theory of dynamic threshold for crack propagation results in an accurate threshold velocity prediction model, compared to other approaches such as energy balance and balance of impact stresses.
2. Using service lifetime of turbine blades as a criterion governing the experimental evaluation of the threshold velocity resultes in a practical threshold testing practices.
3. The threshold velocity is an effective tool to material design and selection.

For the incubation period of Ti-6Al-4V and 17-4 PH stainless steel:

4. Initial droplet impingements on metallic surfaces have a peening effect evidenced by an increase in hardness, and hence, erosion resistance. The initial impingements also result in

an increase in surface roughness and lead to eventual formation and continuous deeping of surface depressions.

5. Impact stresses on surfaces containing depressions are considerably higher than on flat surfaces due to stress concentration. As such, any improvement in erosion resistance of the surface due to droplet peening is negated by the concentration of impact stresses due to presence of surface depression and their deepening.
6. Periodic polishing of metallic surfaces subjected to droplet impingement is an effective method of elongating the incubation period, because eliminates the stress concentration and minimizes lateral jetting effects.
7. The strain hardening exponent (n) dictates the rate at which the fracture point is reached as well as it controls the cyclic increase in hardness and yield strength. Hence, strain hardening exponent (n) plays an important role in the length of the incubation period of the 17-4 PH stainless steel.
8. The erosion resistance of metallic materials is a synergy between several mechanical properties. Strain hardening exponent (n) is a significant factor in this synergy.

6.2 Contribution and Significance of the Thesis

In the context of the water droplet erosion problem and the current status of its literature, the contributions and significance of the present work can be summarized as follows:

- The present work introduced a new material design and selection tool for water droplet erosion (WDE) applications, which is the threshold velocity. That is, the work developed a mathematical model as well as a practical experimental procedure to evaluate the threshold velocity. The threshold velocity - simply calculated from the developed model -

can directly evaluate the risk of developing erosion damage for a specific metal directly from its mechanical properties. This has been achieved through this work for the first time.

- The present work introduced periodic polishing of surfaces as a maintenance practice to extend the service life of blades, especially for their leading edges. The removal of the roughening factor through periodic polishing has been shown in this work to result in delayed incubation period due to elimination of stress concentration.
- For the first time, the present thesis highlighted the importance of the rate of change of initial target properties on the incubation period. Previous accounts considered only the initial (fixed) values of mechanical and surface properties as parameters affecting the length of the incubation period. The present work proved that different rates of change of the initial hardness value (i.e., due to strain hardening) and of roughness (i.e., roughening) leads to different incubation periods even when the initial values are similar. Hence, the work introduces the rates of change of properties as essential parameters in the prediction of the incubation period.

Journal Publication

The following journal papers were published from the present work:

1. **Ibrahim, M.E.**; Medraj, M. "Water Droplet Erosion of Wind Turbine Blades: Mechanics, Testing, Modeling and Future Perspectives" *Materials* **2020**, *13*, 157.
2. **Ibrahim, M.E.**; Medraj, M. "Prediction and Experimental Evaluation of the Threshold Velocity in Water Droplet Erosion" *Materials & Design* **2022**, *213*, 110312.
3. **Ibrahim, M.E.**; Marzbali, M.; Gujba, A.K.; Medraj, M. "The Role of Hardening and Roughening during the Incubation Period in Water Droplet Erosion" (Submitted)
4. **Ibrahim, M.E.**; Gujba, A.K.; Medraj, M. "Experimental Investigation of the Water Droplet Erosion Behavior of Aluminum Alloys" (Submitted).

5. Rizwan, S.K.**; Ibrahim, M.E.**; Gujba, A.K.; Pugh, M.D.; Medraj, M. "On The Role of Strain Hardening and Mechanical Properties in Water Droplet Erosion" *Tribology International* **2022**, 173, 107649.

6.3 Suggestions for Future Work

Investigation of water droplet erosion (WDE) phenomenon encompasses several aspects. The present work aimed to tackle the prediction of the threshold velocity and the incubation period. As far as predicting water droplet erosion is concerned, the present work suggests the following topics to be addressed by future researcher:

- The developed threshold prediction model are limited to metals. Further efforts are needed to extend the present work to include other classes of materials. In particular, the threshold velocity and incubation period of elastomers and polymer composites are needed as the leading edge erosion of wind turbine blades is increasingly becoming a concern.
- In this study, it was shown that roughness changes during the incubation period, and that different roughening profiles result in different incubation periods. Yet, there is no parameter that can be standardized as an "index" to quantify the change in roughness. Therefore, further research is needed to develop an index or a parameter that indicates the way in which roughness changes with exposure duration.
- Research is needed to understand the role of lateral jetting in erosion damage and how that changes with changing the impact velocity.
- The present work demonstrated qualitatively how strain hardening exponent influences the damage accumulation process during the incubation period. Quantitative evaluation of the effect of the strain hardening is needed.

- The present work showed that the hardening and roughening are both important parameters that need to be considered in the prediction of the incubation period. As such, a new incubation prediction model incorporating these two parameters is needed.

REFERENCES

1. Heymann, F.J. Liquid Impingement Erosion. In *ASM Handbook Volume-18. Friction, lubrication and wear technology*; ASM International, 1992; pp. 408–429 ISBN 0871700077.
2. Honegger, E. Corrosion and Erosion of Steam Turbine Blading. *Brown Boveri Rev.* **1924**, 263–278.
3. Ahmad, M.; Casey, M.; Sürken, N. Experimental Assessment of Droplet Impact Erosion Resistance of Steam Turbine Blade Materials. *Wear* **2009**, *267*, 1605–1618, doi:10.1016/j.wear.2009.06.012.
4. Ahmad, M.; Schatz, M.; Casey, M.V. An Empirical Approach to Predict Droplet Impact Erosion in Low-Pressure Stages of Steam Turbines. *Wear* **2018**, *402–403*, 57–63, doi:10.1016/j.wear.2018.02.004.
5. Kirols, H.S.; Kevorkov, D.; Uihlein, A.; Medraj, M. Water Droplet Erosion of Stainless Steel Steam Turbine Blades. *Mater. Res. Express* **2017**, *4*, 086510, doi:10.1088/2053-1591/aa7c70.
6. Khan, J. Fog Cooling, Wet Compression and Droplet Dynamics In Gas Turbine Compressors. *Univ. New Orleans Theses Diss.* **2009**.
7. Ameri, M.; Nabati, H.; Keshtgar, A. Gas Turbine Power Augmentation Using Fog Inlet Air-Cooling System.; January 1 2004.
8. Mishnaevsky, L.; Hasager, C.B.; Bak, C.; Tilg, A.-M.; Bech, J.I.; Doagou Rad, S.; Fæster, S. Leading Edge Erosion of Wind Turbine Blades: Understanding, Prevention and Protection. *Renew. Energy* **2021**, *169*, 953–969, doi:10.1016/j.renene.2021.01.044.
9. Ibrahim, M.; Medraj, M. Water Droplet Erosion of Wind Turbine Blades: Mechanics, Testing, Modeling and Future Perspectives. *Materials* **2020**, *13*, 157, doi:https://doi.org/10.3390/ma13010157.
10. Gohardani, O. Impact of Erosion Testing Aspects on Current and Future Flight Conditions. *Prog. Aerosp. Sci.* **2011**, *47*, 280–303, doi:10.1016/j.paerosci.2011.04.001.
11. Burson-Thomas, C.B.; Wellman, R.; Harvey, T.J.; Wood, R.J.K. Water Droplet Erosion of Aeroengine Fan Blades: The Importance of Form. *Wear* **2019**, *426–427*, 507–517, doi:10.1016/j.wear.2018.12.030.
12. Karstadt, S.; Werner, J.; Münz, S.; Aymanns, R. Effect of Water Droplets Caused by Low Pressure EGR on Spinning Compressor Wheels. In Proceedings of the 19th Supercharging Conference Dresden; 2014.
13. Fyall, A.A. Practical Aspects of Rain Erosion of Aircraft and Missiles. *Philos. Trans. R. Soc. Lond. Ser. Math. Phys. Sci.* **1966**, *260*, 161–167.
14. Van Der Zwaag, S.; Field, J.E. Rain Erosion Damage in Brittle Materials. *Eng. Fract. Mech.* **1983**, *17*, 367–379, doi:10.1016/0013-7944(83)90087-5.

15. Fujisawa, N.; Yamagata, T.; Wada, K. Attenuation of Wall-Thinning Rate in Deep Erosion by Liquid Droplet Impingement. *Ann. Nucl. Energy* **2016**, *88*, 151–157, doi:10.1016/j.anucene.2015.10.024.

16. Yasugahira, N.; Namura, K.; Kaneko, R.; Satoh, T. Erosion Resistance of Titanium Alloys for Steam Turbine Blades as Measured by Water Droplet Impingement. In *Titanium Steam Turbine Blading*; Jaffee, R.I., Ed.; Pergamon: Oxford, 1990; pp. 383–402 ISBN 978-0-08-037301-0.

17. Ryzhenkov, V.A.; Lebedeva, A.I.; Mednikov, A.F. Erosion Wear of the Blades of Wet-Steam Turbine Stages: Present State of the Problem and Methods for Solving It. *Therm. Eng.* **2011**, *58*, 713, doi:10.1134/S0040601511090138.

18. Gujba, A.K.; Ren, Z.; Dong, Y.; Ye, C.; Medraj, M. Effect of Ultrasonic Nanocrystalline Surface Modification on the Water Droplet Erosion Performance of Ti6Al4V. *Surf. Coat. Technol.* **2016**, *307*, 157–170, doi:10.1016/j.surfcoat.2016.08.054.

19. Keegan, M.H.; Nash, D.H.; Stack, M.M. On Erosion Issues Associated with the Leading Edge of Wind Turbine Blades. *J. Phys. D: Appl. Phys.* **2013**, *46*, 383001, doi:10.1088/0022-3727/46/38/383001.

20. Bartolomé, L.; Teuwen, J. Prospective Challenges in the Experimentation of the Rain Erosion on the Leading Edge of Wind Turbine Blades. *Wind Energy* **2019**, *22*, 140–151, doi:10.1002/we.2272.

21. Fujisawa, N.; Yamagata, T.; Hayashi, K.; Takano, T. Experiments on Liquid Droplet Impingement Erosion by High-Speed Spray. *Nucl. Eng. Des.* **2012**, *250*, 101–107, doi:10.1016/j.nucengdes.2012.06.022.

22. Burson-Thomas, C.B.; Wellman, R.; Harvey, T.J.; Wood, R.J.K. Importance of Surface Curvature in Modeling Droplet Impingement on Fan Blades. *J. Eng. Gas Turbines Power* **2019**, *141*, 031005, doi:10.1115/1.4041149.

23. Chapman, B. History of Jet Fighters. In *Global Defense Procurement and the F-35 Joint Strike Fighter*; Chapman, B., Ed.; Springer International Publishing: Cham, 2019; pp. 11–44 ISBN 978-3-030-01367-7.

24. Field, J.E. Invited Lecture: Liquid Impact: Theory, Experiment, Applications. *Wear* **1999**, *233–235*, 1–12, doi:10.1016/S0043-1648(99)00189-1.

25. Cook, S.S.; Parsons, C.A. Erosion by Water-Hammer. *Proc. R. Soc. Lond. Ser. Contain. Pap. Math. Phys. Character* **1928**, *119*, 481–488, doi:10.1098/rspa.1928.0107.

26. Heymann, F.J. On the Shock Wave Velocity and Impact Pressure in High-Speed Liquid-Solid Impact. *J. Basic Eng.* **1968**, *90*, 400–402, doi:10.1115/1.3605114.

27. Dear, J.P.; Field, J.E. High-speed Photography of Surface Geometry Effects in Liquid/Solid Impact. *J. Appl. Phys.* **1988**, *63*, 1015–1021, doi:10.1063/1.340000.

28. Tatekura, Y.; Watanabe, M.; Kobayashi, K.; Sanada, T. Pressure Generated at the Instant of Impact between a Liquid Droplet and Solid Surface. *R. Soc. Open Sci. 5*, 181101, doi:10.1098/rsos.181101.

29. Heymann, F.J. High-Speed Impact between a Liquid Drop and a Solid Surface. *J. Appl. Phys.* **1969**, *40*, 5113–5122, doi:10.1063/1.1657361.

30. Blowers, R.M. On the Response of an Elastic Solid to Droplet Impact. *IMA J. Appl. Math.* **1969**, *5*, 167–193.

31. Marzbali, M.; Dolatabadi, A. High-Speed Droplet Impingement on Dry and Wetted Substrates. *Phys. Fluids* **2020**, *32*, 112101, doi:10.1063/5.0020977.

32. Haller, K.K.; Ventikos, Y.; Poulikakos, D.; Monkewitz, P. Computational Study of High-Speed Liquid Droplet Impact. *J. Appl. Phys.* **2002**, *92*, 2821–2828, doi:10.1063/1.1495533.

33. Sanada, T.; Ando, K.; Colonius, T. A Computational Study of High-Speed Droplet Impact. *Fluid Dyn. Mater. Process.* **2009**, *7*, doi:10.3970/fdmp.2011.007.329.

34. Li, R.; Ninokata, H.; Mori, M. A Numerical Study of Impact Force Caused by Liquid Droplet Impingement onto a Rigid Wall. *Prog. Nucl. Energy* **2011**, *53*, 881–885, doi:10.1016/j.pnucene.2011.03.002.

35. Field, J.E.; Lesser, M.B.; Dear, J.P.; Tabor, D. Studies of Two-Dimensional Liquid-Wedge Impact and Their Relevance to Liquid-Drop Impact Problems. *Proc. R. Soc. Lond. Math. Phys. Sci.* **1985**, *401*, 225–249, doi:10.1098/rspa.1985.0096.

36. Brunton, J.H.; Bowden, F.P. A Discussion on Deformation of Solids by the Impact of Liquids, and Its Relation to Rain Damage in Aircraft and Missiles, to Blade Erosion in Steam Turbines, and to Cavitation Erosion - High Speed Liquid Impact. *Philos. Trans. R. Soc. Lond. Ser. Math. Phys. Sci.* **1966**, *260*, 79–85, doi:10.1098/rsta.1966.0031.

37. Jenkins, D.C.; Booker, J.D. The Impingement of Water Drops on a Surface Moving at High Speed. In Proceedings of the Aerodynamic Capture of Particles; 1960; pp. 97–103.

38. Adler, W.F. The Mechanics of Liquid Impact. In *Treatise on Materials Science and Technology*; Academic Press, 1979; Vol. 16, pp. 127–183.

39. Heymann, F. On the Time Dependence of the Rate of Erosion Due to Impingement or Cavitation. *Eros. Cavitation Impingement* **1967**, doi:10.1520/STP46046S.

40. Kennedy, C.F.; Field, J.E. Damage Threshold Velocities for Liquid Impact. *J. Mater. Sci.* **2000**, *35*, 5331–5339, doi:10.1023/A:1004842828161.

41. Thiruvengadam, A.; Rudy, S.; Gunasekaran, M. Experimental and Analytical Investigations on Liquid Impact Erosion. In *Characterization and Determination of Erosion Resistance*; ASTM Special Technical Publication; ASTM International, 1970.

42. Field, J.E.; Seward, C.R.; Pickles, C.S.; Coad, E.J.; Watt, M. *Studies of Rain Erosion Mechanisms in a Range of IR Transmitting Ceramics-Including Coated Samples.*; Cambridge University, Cavendish Lab, 1994;

43. Evans, A.G.; Gulden, M.E.; Rosenblatt, M.; Tabor, D. Impact Damage in Brittle Materials in the Elastic-Plastic Response Régime. *Proc. R. Soc. Lond. Math. Phys. Sci.* **1978**, *361*, 343–365, doi:10.1098/rspa.1978.0106.

44. Heymann, F.J. Toward Quantitative Prediction of Liquid Impact Erosion. In *Characterization and Determination of Erosion Resistance*; ASTM Special Technical Publication; ASTM International, 1970.

45. Springer, G.S. *Erosion by Liquid Impact*; Scripta Publishing Co.: Washington, DC, USA, 1976;

46. Ruml, Z.; Straka, F. A New Model for Steam Turbine Blade Materials Erosion. *Wear* **1995**, *186*, 421–424.

47. Adler, W.F. Waterdrop Impact Modeling. *Wear* **1995**, *186–187*, 341–351, doi:10.1016/0043-1648(95)07176-8.

48. Heymann, F.J. Survey of Clues to the Relationship between Erosion Rate and Impact Conditions. In Proceedings of the Second Meersburg Conference on Rrain Erosion and Allied Phenomena; Fyall, A.A., King, R.B., Eds.; Meersburg, Federal German Republic, 1967; pp. 683–760.

49. Engel, O.G. Impact of Liquid Drops. In *Erosion and Cavitation*; ASTM Special Technical Publication; ASTM International, 1961.

50. Fujisawa, K. Effect of Impact Velocity on Time-Dependent Force and Droplet Pressure in High-Speed Liquid Droplet Impingement. *Ann. Nucl. Energy* **2022**, *166*, 108814, doi:10.1016/j.anucene.2021.108814.

51. Honegger, E. Tests on Erosion Caused by Jets. *Brown Boveri Rev* **1927**, *14*, 95–104.

52. de Haller, P. Untersuchungen Ber Die Durch Kavitation Hervorgerufenen Korrosionen. *Schweiz. Bauztg.* **1933**, *101*, 243.

53. Thiruvengadam, A. The Concept of Erosion Strength. In *Erosion by Cavitation or Impingement*; ASTM International: West Conshohocken, PA, USA, 1967.

54. Mahdipoor, M.S.; Kirols, H.S.; Kevorkov, D.; Jedrzejowski, P.; Medraj, M. Influence of Impact Speed on Water Droplet Erosion of TiAl Compared with Ti6Al4V. *Sci. Rep.* **2015**, *5*, 14182, doi:10.1038/srep14182.

55. Slot, H.; Matthews, D.; Schipper, D.; van der Heide, E. Fatigue-Based Model for the Droplet Impingement Erosion Incubation Period of Metallic Surfaces. *Fatigue Fract. Eng. Mater. Struct.* **2021**, *44*, 199–211, doi:10.1111/ffe.13352.

56. Borello, D.; Venturini, P.; Gabriele, S.; Andreoli, M. New Model to Predict Water Droplets Erosion Based on Erosion Test Curves: Application to On-Line Water Washing of a Compressor.; American Society of Mechanical Engineers Digital Collection, November 5 2019.

57. Zhang, Z.; Liu, T.; Zhang, D.; Xie, Y. Water Droplet Erosion Life Prediction Method for Steam Turbine Blade Materials Based on Image Recognition and Machine Learning. *J. Eng. Gas Turbines Power* **2021**, *143*, doi:10.1115/1.4049768.

58. Tobin, E.F.; Young, T.M. Analysis of Incubation Period Versus Surface Topographical Parameters in Liquid Droplet Erosion Tests. *Mater. Perform. Charact.* **2017**, *6*, 144–164, doi:10.1520/MPC20160085.

59. Heymann, F.J. Erosion by Liquids. *Mach. Des.* **1970**, *10*, 118–124.

60. Ibrahim, M.E.; Medraj, M. Prediction and Experimental Evaluation of the Threshold Velocity in Water Droplet Erosion. *Mater. Des.* **2022**, *213*, 110312, doi:10.1016/j.matdes.2021.110312.

61. Gujba, A.K.; Hackel, L.; Medraj, M. Water Droplet Erosion Performance of Laser Shock Peened Ti-6Al-4V. *Metals* **2016**, *6*, 262, doi:10.3390/met6110262.

62. Ma, D.; Mostafa, A.; Kevorkov, D.; Jedrzejowski, P.; Pugh, M.; Medraj, M. Water Impingement Erosion of Deep-Rolled Ti64. *Metals* **2015**, *5*, 1462–1486, doi:10.3390/met5031462.

63. Rieger, H. The Damage to Metals on High Speed Impact with Water Droplets. In Proceedings of the First International Conference on Rain Erosion and Associated Phenomena; Royal Aircraft Establishment: Meersburg, Germany, 1965.

64. Hoff, G.; Langbein, G.; Rieger, H. Material Destruction Due to Liquid Impact. In *Erosion by cavitation and impingement. ASTM STP-408*; ASTM: Atlantic City, NJ, USA, 1967; pp. 42–69 ISBN 978-0-8031-6756-8.

65. Foldyna, J.; Klich, J.; Hlaváček, P.; Zeleňák, M.; Scucka, J. Erosion of Metals by Pulsating Water Jet. *Teh. Vjesn.* **2012**, *19*, 381–386.

66. Morris, J.W.; Wahl, N.E. Rain Erosion Damage of Ductile Metals. In Proceedings of the Fourth International Conference on Rain Erosion and Associated Phenomena; Royal Aircraft Establishment: Meersburg, Germany, 1974.

67. Fujisawa, N.; Yamagata, T.; Takano, S.; Saito, K.; Morita, R.; Fujiwara, K.; Inada, F. The Influence of Material Hardness on Liquid Droplet Impingement Erosion. *Nucl. Eng. Des.* **2015**, *288*, 27–34, doi:10.1016/j.nucengdes.2015.03.016.

68. O'Carroll, A.; Hardiman, M.; Tobin, E.F.; Young, T.M. Correlation of the Rain Erosion Performance of Polymers to Mechanical and Surface Properties Measured Using Nanoindentation. *Wear* **2018**, *412–413*, 38–48, doi:10.1016/j.wear.2018.07.008.

69. Moore, M.A. The Relationship between the Abrasive Wear Resistance, Hardness and Microstructure of Ferritic Materials. *Wear* **1974**, *28*, 59–68, doi:10.1016/0043-1648(74)90101-X.

70. Oka, Y.I.; Matsumura, M.; Kawabata, T. Relationship between Surface Hardness and Erosion Damage Caused by Solid Particle Impact. *Wear* **1993**, *162–164*, 688–695, doi:10.1016/0043-1648(93)90067-V.

71. Richman, R.H.; McNaughton, W.P. Correlation of Cavitation Erosion Behavior with Mechanical Properties of Metals. *Wear* **1990**, *140*, 63–82, doi:10.1016/0043-1648(90)90122-Q.

72. Hammitt, F.G.; Heymann, F.J. Liquid-Erosion Failures. In *ASM Handbook*; 1986; Vol. 11, pp. 163–171.

73. Hattori, S.; Itoh, T. Cavitation Erosion Resistance of Plastics. *Wear* **2011**, *271*, 1103–1108, doi:10.1016/j.wear.2011.05.012.

74. Będkowski, W.; Gasiak, G.; Lachowicz, C.; Lichtarowicz, A.; Łagoda, T.; Macha, E. Relations between Cavitation Erosion Resistance of Materials and Their Fatigue Strength under Random Loading. *Wear* **1999**, *230*, 201–209, doi:10.1016/S0043-1648(99)00105-2.

75. R. Seward, C.; S. Pickles, C.; R. Marrah; E. Field, J. Rain Erosion Data on Window and Dome Materials. In Proceedings of the SPIE; SPIE: San Diego, CA, United States, 1992; Vol. 1760.

76. Hobbs, J.M. Experience With a 20-Kc Cavitation Erosion Test. In *Erosion by Cavitation or Impingement*; ASTM International: West Conshohocken , PA, USA; pp. 159–185.

77. Hancox, N.L.; Brunton, J.H. The Erosion of Solids by the Repeated Impact of Liquid Drops. *Philos. Trans. R. Soc. Lond. Ser. A* **1966**, *260*, 121–139, doi:10.1098/rsta.1966.0036.

78. Kirols, H.S.; Kevorkov, D.; Uihlein, A.; Medraj, M. The Effect of Initial Surface Roughness on Water Droplet Erosion Behaviour. *Wear* **2015**, *342–343*, 198–209, doi:10.1016/j.wear.2015.08.019.

79. Fujisawa, K.; Ohki, M.; Fujisawa, N. Influence of Surface Roughness on Liquid Droplet Impingement Erosion. *Wear* **2019**, *432–433*, 202955, doi:10.1016/j.wear.2019.202955.

80. Di, J.; Wang, S.; Yan, X.; Cai, L.; Xie, Y. Experimental Investigation on Effect of Surface Strengthening Process and Roughness on Water Droplet Erosion Behavior in Turbomachinery. *Tribol. Int.* **2021**, *153*, 106647, doi:10.1016/j.triboint.2020.106647.

81. Zhang, Z.; Yang, B.; Zhang, D.; Xie, Y. Experimental Investigation on the Water Droplet Erosion Characteristics of Blade Materials for Steam Turbine. *Proc. Inst. Mech. Eng. Part C J. Mech. Eng. Sci.* **2020**, 0954406220979730, doi:10.1177/0954406220979730.

82. Gujba, A.K.; Hackel, L.; Kevorkov, D.; Medraj, M. Water Droplet Erosion Behaviour of Ti–6Al–4V and Mechanisms of Material Damage at the Early and Advanced Stages. *Wear* **2016**, *358–359*, 109–122, doi:10.1016/j.wear.2016.04.008.

83. Zhou, B.; Liu, B.; Zhang, S. The Advancement of 7XXX Series Aluminum Alloys for Aircraft Structures: A Review. *Metals* **2021**, *11*, 718, doi:10.3390/met11050718.

84. Viswanathan, U.K.; Banerjee, S.; Krishnan, R. Effects of Aging on the Microstructure of 17-4 PH Stainless Steel. *Mater. Sci. Eng.* **1988**, *104*, 181–189, doi:10.1016/0025-5416(88)90420-X.

85. Hsiao, C.N.; Chiou, C.S.; Yang, J.R. Aging Reactions in a 17-4 PH Stainless Steel. *Mater. Chem. Phys.* **2002**, *74*, 134–142, doi:10.1016/S0254-0584(01)00460-6.

86. Yeli, G.; Auger, M.A.; Wilford, K.; Smith, G.D.W.; Bagot, P.A.J.; Moody, M.P. Sequential Nucleation of Phases in a 17-4PH Steel : Microstructural Characterisation and Mechanical Properties. *Acta Mater.* **2017**, *125*, 38–49, doi:10.1016/j.actamat.2016.11.052.

87. *ASTM A693-06: Standard Specification for Precipitation-Hardening Stainless and Heat-Resisting Steel Plate, Sheet, and Strip*; 2006th ed.; ASTM International: West Conshohocken, PA, USA, 2006;

88. ASM Material Data Sheet Available online: http://asm.matweb.com/search/SpecificMaterial.asp?bassnum=MA2024T4 (accessed on 14 September 2021).

89. Anderson, D.; Rosakis, A. Dynamic Fracture Properties of Titanium Alloys. *Exp. Mech.* **2006**, *46*, 399–406, doi:10.1007/s11340-006-6421-9.

90. Rack, H.J. *Physical and Mechanical Properties of Cast 17-4 PH Stainless Steel*; Sandia National Labs: Albuquerque, NM, USA, 1981;

91. Shaik, R.A. Influence of Strain Hardening on the Water Droplet Erosion Performance of 17-4 PH Stainless Steel. MS Thesis, Concordia University, 2021.

92. Brnic, J.; Turkalj, G.; Canadija, M.; Lanc, D.; Krscanski, S. Martensitic Stainless Steel AISI 420—Mechanical Properties, Creep and Fracture Toughness. *Mech. Time-Depend. Mater.* **2011**, *15*, 341–352, doi:10.1007/s11043-011-9137-x.

93. Stainless Steel - Grade 420 (UNS S42000) Available online: https://www.azom.com/article.aspx?ArticleID=972 (accessed on 30 July 2021).

94. Alexopoulos, N.D.; Stylianos, A.; Campbell, J. Dynamic Fracture Toughness of Al–7Si–Mg (A357) Aluminum Alloy. *Mech. Mater.* **2013**, *58*, 55–68, doi:10.1016/j.mechmat.2012.11.005.

95. ASM Material Data Sheet Available online: http://asm.matweb.com/search/SpecificMaterial.asp?bassnum=MA7075T6 (accessed on 19 September 2021).

96. Safarbali, B.; Shamanian, M.; Eslami, A. Effect of Post-Weld Heat Treatment on Joint Properties of Dissimilar Friction Stir Welded 2024-T4 and 7075-T6 Aluminum Alloys. *Trans. Nonferrous Met. Soc. China* **2018**, *28*, 1287–1297, doi:10.1016/S1003-6326(18)64766-1.

97. *ASTM G73-04: Standard Practice for Liquid Impingement Erosion Testing*; ASTM International: West Conshohocken, PA, USA, 2004;

98. Mahdipoor, M.S. Water Droplet Erosion Resistant Materials and Surface Treatments. PhD Dissertation, Concordia University, 2016.

99. Mahdipoor, M.S.; Kevorkov, D.; Jedrzejowski, P.; Medraj, M. Water Droplet Erosion Mechanism of Nearly Fully-Lamellar Gamma TiAl Alloy. *Mater. Des.* **2016**, *89*, 1095–1106, doi:10.1016/j.matdes.2015.10.077.

100. Steverding, E.; Lehnigk, S.H. Dynamic Threshold Conditions for Crack Propagation. *Int. J. Fract. Mech.* **1969**, *5*, 369–370, doi:10.1007/BF00190970.

101. Freund, L.B. *Dynamic Fracture Mechanics*; Cambridge University Press, 1990; ISBN 978-0-511-54676-1.

102. Hornbogen, E. The Role of Fracture Toughness in the Wear of Metals. *Wear* **1975**, *33*, 251–259, doi:10.1016/0043-1648(75)90280-X.

103. Tiryakioğlu, M. On the Relationship between Vickers Hardness and Yield Stress in Al–Zn–Mg–Cu Alloys. *Mater. Sci. Eng. A* **2015**, *633*, 17–19, doi:10.1016/j.msea.2015.02.073.

104. Tabor, D. *The Hardness of Metals*; Oxford University Press, 2000; ISBN 978-0-19-850776-5.

105. Fu, J.; Zhu, K.; Nie, X.; Tang, Y.; Yang, Z.; Qi, L. Inertia-Based Identification of Elastic Anisotropic Properties for Materials Undergoing Dynamic Loadings Using the Virtual Fields Method and Heterogeneous Impact Tests. *Mater. Des.* **2021**, *203*, 109594, doi:10.1016/j.matdes.2021.109594.

106. Chen, F.; Gu, Y.; Xu, G.; Cui, Y.; Chang, H.; Zhou, L. Improved Fracture Toughness by Microalloying of Fe in Ti-6Al-4V. *Mater. Des.* **2020**, *185*, 108251, doi:10.1016/j.matdes.2019.108251.

107. Bragov, A.; Konstantinov, A.; Kuznetsov, A.; Lomunov, A.; Savenkov, G. Relationship Between the Crack Velocity, Fractal Dimension, and Dynamic Fracture Toughness of a Material. *J. Appl. Mech. Tech. Phys.* **2018**, *59*, 132–137, doi:10.1134/S0021894418010169.

108. Wu, J.-H.; Lin, C.-K. Tensile and Fatigue Properties of 17-4 PH Stainless Steel at High Temperatures. *Metall. Mater. Trans. A* **2002**, *33*, 1715–1724, doi:10.1007/s11661-002-0180-8.

109. Janeček, M.; Nový, F.; Stráský, J.; Harcuba, P.; Wagner, L. Fatigue Endurance of Ti-6Al-4V Alloy with Electro-Eroded Surface for Improved Bone in-Growth. *J. Mech. Behav. Biomed. Mater.* **2011**, *4*, 417–422, doi:10.1016/j.jmbbm.2010.12.001.

110. Behrendt, A. Investigation of Parameters of Aircraft Materials at Speeds up to 1000 Meters per Second. In Proceedings of the Fourth International Conference on Rain Erosion and Associated Phenomena; Royal Aircraft Establishment: Meersburg, Germany, 1974.

111. King, R.B. *Multiple Impact Rain Erosion Studies at Velocities up to 450 m/s (M1.3)*; Royal Aircraft Establishment, 1967;

112. Ripken, J. A Test Rig for Studying Impingement and Cavitation Damage. In *Erosion by Cavitation or Impingement*; ASTM International: West Conshohocken, PA, USA, 1967.

113. Kamkar, N.; Bridier, F.; Jedrzejowski, P.; Bocher, P. Water Droplet Impact Erosion Damage Initiation in Forged Ti–6Al–4V. *Wear* **2015**, *322–323*, 192–202, doi:10.1016/j.wear.2014.10.020.

114. Gerdes, C.; Karimi, A.; Bieler, H.W. Water Droplet Erosion and Microstructure of Laser-Nitrided Ti-6Al-4V. *Wear* **1995**, *186–187*, 368–374, doi:10.1016/0043-1648(95)07153-9.

115. Huang, L.; Folkes, J.; Kinnell, P.; Shipway, P.H. Mechanisms of Damage Initiation in a Titanium Alloy Subjected to Water Droplet Impact during Ultra-High Pressure Plain Waterjet Erosion. *J. Mater. Process. Technol.* **2012**, *212*, 1906–1915, doi:10.1016/j.jmatprotec.2012.04.013.

116. Pilkey, W.D.; Pilkey, D.F.; Bi, Z. *Peterson's Stress Concentration Factors*; John Wiley & Sons, 2020; ISBN 978-1-119-53251-4.

117. Child, D.J.; West, G.D.; Thomson, R.C. Assessment of Surface Hardening Effects from Shot Peening on a Ni-Based Alloy Using Electron Backscatter Diffraction Techniques. *Acta Mater.* **2011**, *59*, 4825–4834, doi:10.1016/j.actamat.2011.04.025.

118. Shaik, R.A.; Ibrahim, M.E.; Gujba, A.K.; Pugh, M.D.; Medraj, M. On the Role of Strain Hardening and Mechanical Properties in Water Droplet Erosion of Metals. *Tribol. Int.* **2022**, *173*, 107649, doi:10.1016/j.triboint.2022.107649.

119. Rack, H.J.; Kalish, D. Strength, Fracture Toughness, and Low Cycle Fatigue Behavior of 17-4 Ph Stainless Steel. *Metall. Trans.* **1974**, *5*, 1595–1605, doi:10.1007/BF02646331.

120. Thomas, G.P.; Brunton, J.H. Drop Impingement Erosion of Metals. *Proc. R. Soc. Lond. Ser. Math. Phys. Sci.* **1970**, *314*, 549–565.

121. Amirzadeh, B.; Louhghalam, A.; Raessi, M.; Tootkaboni, M. A Computational Framework for the Analysis of Rain-Induced Erosion in Wind Turbine Blades, Part I: Stochastic Rain Texture Model and Drop Impact Simulations. *J. Wind Eng. Ind. Aerodyn.* **2017**, *163*, 33–43, doi:10.1016/j.jweia.2016.12.006.

122. Brown, V.M.; Alan, W. Hourly Rainfall Climatology of Louisiana. *Theoretical and Applied Climatology 52*, 2019.

123. Marzbali, M.; Dolatabadi, A.; Jedrzejowski, P. Fluid-Solid Interaction Modeling of Compressible Droplet Impact onto Elastic Substrates. In *21st AIAA Computational Fluid Dynamics Conference*; American Institute of Aeronautics and Astronautics.

124. Marzbali, M.; Dolatabadi, A. 2D Axisymmetric Modelling of Single Liquid Droplet Impingement at High Speeds on Thin Liquid Films in Compressible Regime.; August 1 2020.

125. Marzbali, M.; Dolatabadi, A. Flow Characterization of a Water Drop Impinged onto a Rigid Surface at a High Speed and Normal Angle in the Presence of Stagnant Air at Ambient Condition. **2020**, *7*, 92–104, doi:10.11159/jffhmt.2020.009.

APPENDICES

Appendix-A:

Experimental criterion for deciding the length of threshold velocity experiments in terms of number of impacts.

In this section, calculation is carried out to showcase a systematic and practical approach to defining a suitable number of impacts (m) for which the threshold velocity can be evaluated from the $V - N$ erosion curve and erosion experiments.

The choice of m in this work is linked to actual in-service lifetime of components facing water droplet erosion (e.g. blades). We assume that, for a certain component operating under hydrometer environment, erosion threshold condition is met if the component completed its service life without experiencing erosion damage. As such, the threshold velocity is considered as the impact velocity at which the total number of impingements during the entire service life of the component is less than the number of impacts needed to end the incubation period. Unfortunately, the nature of erosion environment (and hence total number of impingements) is not known for most of the engineering application facing water droplet erosion issues such as blades of compressor of gas turbines and steam turbines. In these applications, formation, distribution, and behavior of impacting droplets seem to be of a stochastic nature. However, for wind turbine blades, such information can be statistically accessed through metrological data collected at the turbine location. For this reason, the analysis in this work is primarily carried out for wind turbine blades, and generalization is made for other components. This is shown in the ensuing discussion.

Droplet Impacts on a Wind Turbine Blade

The average life time of a wind turbine blade is around 20 years [121]. Wind turbines experience different raining annual hours depending on the geographical location. If the average raining hours per year is considered to be 500h (for example in the US [122]) and this will be considered in our calculation. Hence, during 20 years of service life, a wind turbine is likely to experience a total number of 10,000 hours of rain. The number of rain drops impinging a unit area of a component is given by [45]:

$$m = V \cos\theta \; q \; t \qquad \text{(A-1)}$$

Where V is the impact velocity, θ is the impact angle, t is the total raining time, and q is the number of droplets in m^3 of rain, and is given by:

$$q = 530.5 \; \frac{I}{V_t \, d^3} \qquad \text{(A-2)}$$

Where d is the droplet size, I is the rain intensity, and V_t is the terminal velocity of droplets. For the purpose of developing a conservative criterion for threshold velocity, we shall assume a severe rain and impingement scenario for a wind turbine blade. We consider that all raining hours during the life time of the turbine are characterized with heavy rain with a rain intensity of 25 mm/h, and that all raindrops are uniformly distributed and have similar diameter of 2 mm (2 mm is the predominant droplet diameter corresponding to 25mm/h intensity [45]). The number of droplets per cubic meter of rain can then be calculated using equation A-2 as follows:

$$q = 530.5 \; \frac{25}{7 \times 2^3} \cong 237 \; \frac{droplets}{m^3 \; of \; rain} \qquad \text{(A-3)}$$

We assume that these droplets impacts a wind turbine blade that its tip can attain a tangential velocity of 150 m/s. Also, we assume that all droplets impinge the surface of the blade at normal angle ($\theta = 0°$), which is known to result in the most severe impact condition. The total number of droplets impinging on a unit area of the turbine blade during its entire life time can then be calculated using equation A-2 as follows:

$$m = V\cos\theta\, q\, t = 150\left(\frac{m}{s}\right) \times 237\left(\frac{droplets}{m^3}\right) \times 10000\, h\,(60\, minutes \times 60 sec)$$

$$\cong 1.28 \times 10^{12}\left(\frac{droplets}{m^2}\right)$$

$$m = V\cos\theta\, q\, t = \cong 1.28 \times 10^{12}\left(\frac{droplets}{m^2}\right) \qquad \text{(A-4)}$$

If we consider a spot in the turbine blade tip of a square mm size, the number of the droplets impacting that spot during the life time of the turbine is then:

$$m = 1.28 \times 10^{12}\,\frac{m^2}{10^6\, mm^2} = 1.28 \times 10^6\left(\frac{droplets}{mm^2}\right)$$

This number of impacts can be used for the threshold criterion. That is, for threshold conditions to prevail during 20 years life time of a wind turbine blade, a mm^2 spot on the turbine blade should endure 1.28 million droplet impingement without showing signs of erosion damages. Hence, for experimental evaluation, we shall consider the threshold velocity to be the impact velocity that results in no erosion damage after 1 million impacts per mm^2.

Although the previous calculation to justify the choice of 1 million impact as a criterion for experimental evaluation of the threshold velocity was carried for wind turbine blades and rain data, there are good reasons to extend it to blades of gas and steam turbines. Firstly, the design life time of blades in the compressor of gas turbines and in low pressure stage of steam turbines

are shorter than wind turbine blades (around 5 years). Hence, it is unlikely that a 1 million droplets would impinge a mm^2 during their life time. Secondly, the size of droplets encountered in these application are much smaller compared to raindrops. It is generally known that smaller droplets results in lower impact stresses and therefore delayed erosion. Thirdly, blades of steam and gas turbines are usually made of metallic alloys compared to polymeric materials of wind turbine blades, which are known to have lower erosion resistance than metals. For these reasons, experimental threshold velocities are considered to be the impact velocities that after 1 million impacts per mm^2 result in no erosion damages for metallic materials.

Appendix-B:

Numerical Analysis in Collaboration with Dr. Mason Marzbali (American University in Dubai)

The numerical analysis of water droplet erosion in this work was done in two parts. The first part represents a fluid-solid interaction (FSI) framework that enables the evaluation of the spatial and temporal distribution of the impact pressure. In the second part of the analysis, Finite Element Method (FEM) is utilized to obtain the stress-strain field in the solid target that results from the impact pressure. These are detailed in the ensuing discussion.

B.1. Spatiotemporal Evolution of Impact Pressure

A Fluid-Solid Interaction (FSI) framework (developed earlier in references [123]) has been utilized in this work to obtain the spatiotemporal evolution of impact pressure. The framework consists of compressible Volume of Fluid (VOF) model with a two-dimensional

axisymmetric geometry for spherical droplets. It utilizes the ideal gas model for the air and Tait's Equation of State (EOS) for water. Full description of the model can be found in [31,123–125].

In the present work, the FSI model was employed to simulate the compressible impact of a 600 µm spherical water droplet impinging a flat rigid surface at a velocity of 250 m/s. The simulation was performed in OpenFoam® software. The obtained spatiotemporal evolution of the impact pressure corresponding to the simulated impact condition is illustrated in Figure B-1.

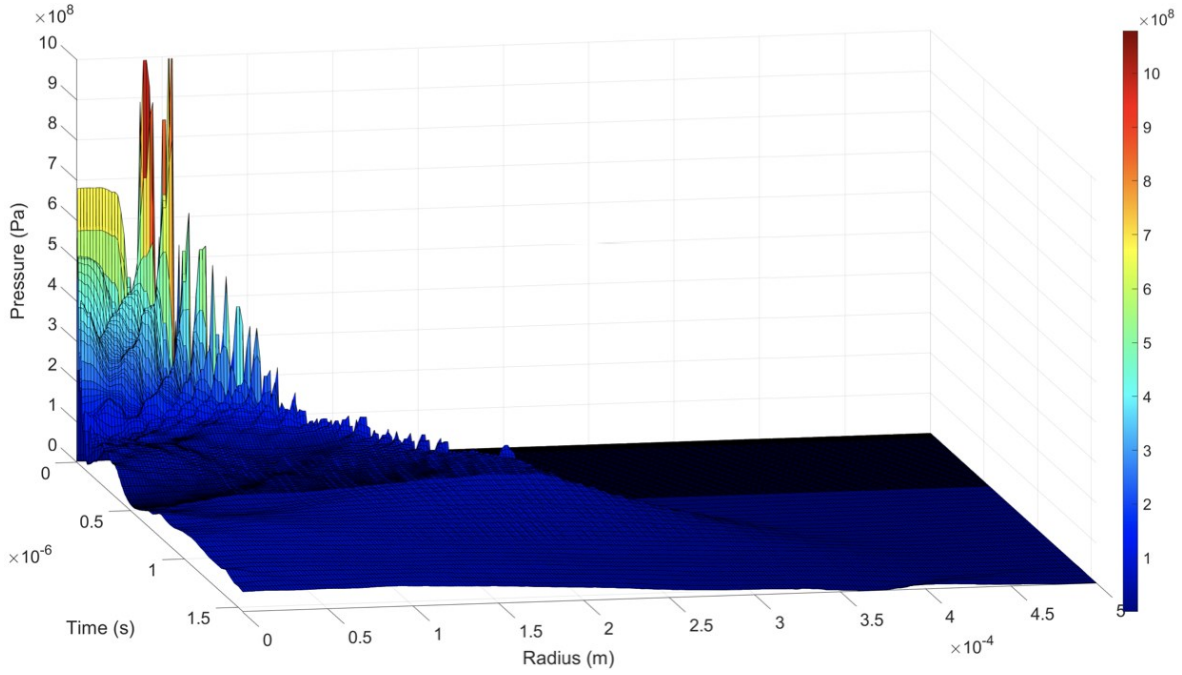

Figure B-1 Spatiotemporal evolution of pressure for a compressible impact of a 600 µm spherical droplet impinging on a flat rigid surface at a velocity of 250 m/s.

B.2. Finite Element Analysis (FEA)

The impact pressure obtained from the fluid simulation was imported to the finite elements analysis software (ANSYS®) and used as time-step loading boundary condition on the surface of the Ti-6Al-4V sample. The sample was modeled using the 2D cross section of the coupon (i.e., 8 mm × 3 mm) as illustrated in Figure B-2. Isotropic material properties of Ti-6Al-

4V were applied to the 2D model. Then, two-dimensional quadrilateral mesh with a width of 20 µm (30 cells per diameter of the water droplet) was generated in ANSYS® Mechanical for transient structural modelling in cartesian coordinate system, as shown in Figure B-3. The top 500-µm layer was meshed with square 20-µm elements and a growth rate of 1.015 was applied to the mesh along the depth, from the top surface toward the bottom surface, to reduce the number of total elements (=38000). A grid sensitivity analysis was performed to ensure that further grid refinement does not change the overall maximum stress in the plate. It is worth mentioning that the grid size used in the Computational Fluid Dynamics (CFD) simulations for this case was 1 µm, which is considered very fine. This was done to capture the compressible region in the fluid and the high-pressure emergence due to the ejection of the lateral jets. This requires the imported pressure distribution to be mapped (20 CFD nodes on to 1 FEM node). As such, a mapping with profile preserving and triangulation weighting was applied while importing the pressure load.

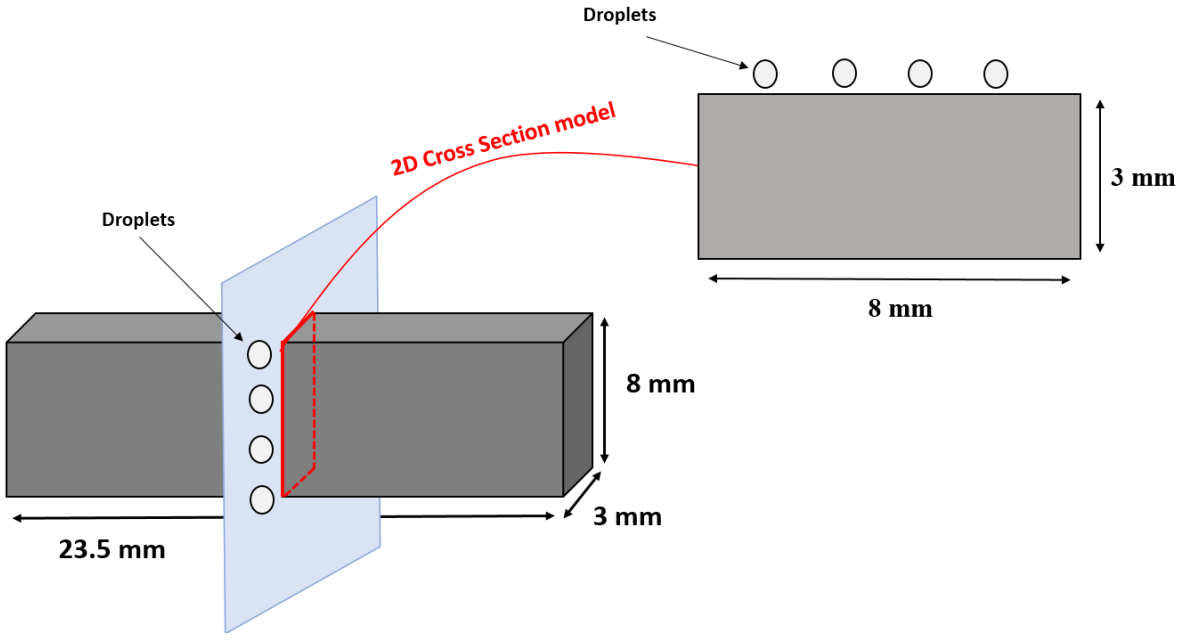

Figure B-2 2D model for finite element analysis.

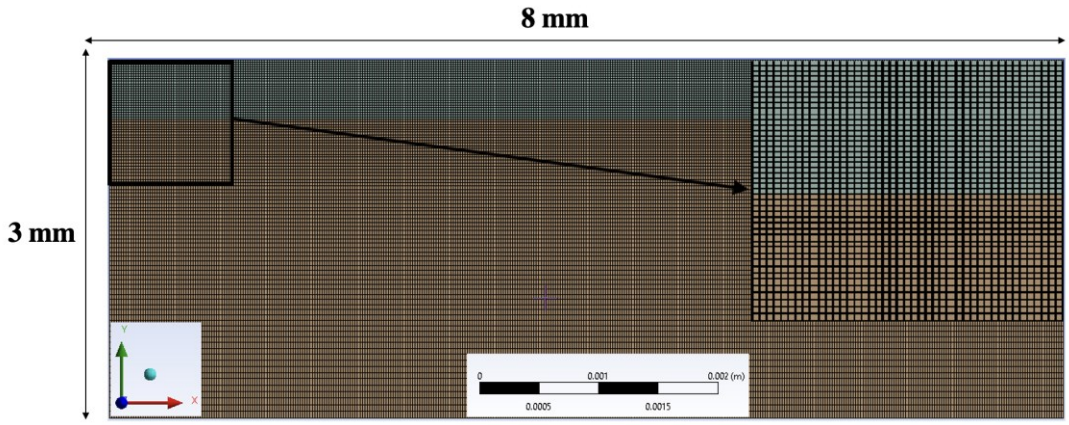

Figure B-3 Two-dimensional quadrilateral mesh used in FEM modelling.

Since the length of the coupon (23.5 mm) is much larger than its thickness (3 mm), plane strain condition was applied to the *z* direction (assuming infinitely long solid bar). Deformation of the solid was set to the elastic mode that follows the Hooke's law. The coupons are assumed to be at room temperature and the heat generated due to the impact is ignored. As such, all thermal stresses are neglected. The imported transient pressure distribution was applied on the top edge. The same impact pressure was applied at four equally-spaced locations on the model to represent the impact conditions of the erosion experiments (as illustrated in Figure B-2). The bottom edge was set to zero displacement (since it is fixed to the coupon holder in the erosion rig). The left and right edges are not constrained and therefore free to deform. The Mechanical APDL solver was used, where Newton-Raphson method was employed for solving the nonlinear equations. Moderate speed dynamics with large deflection was enabled in the solver and an energy dissipation ratio of 10^{-3} was selected. The stiffness coefficient was defined by direct input and both the stiffness and mass coefficients are set to 0. The convergence for force, moment and displacement are all controlled by the program automatically for better stabilization. The simulations were performed on a single processor of a local machine equipped with Intel®

Core™ i7-6700 CPU @ 3.40GHz with 16 GB installed RAM. The average computational time for each case was under one hour.